Directed growth of organic nanofibers

Ph.D. Thesis
Mads Clausen Institute
University of Southern Denmark

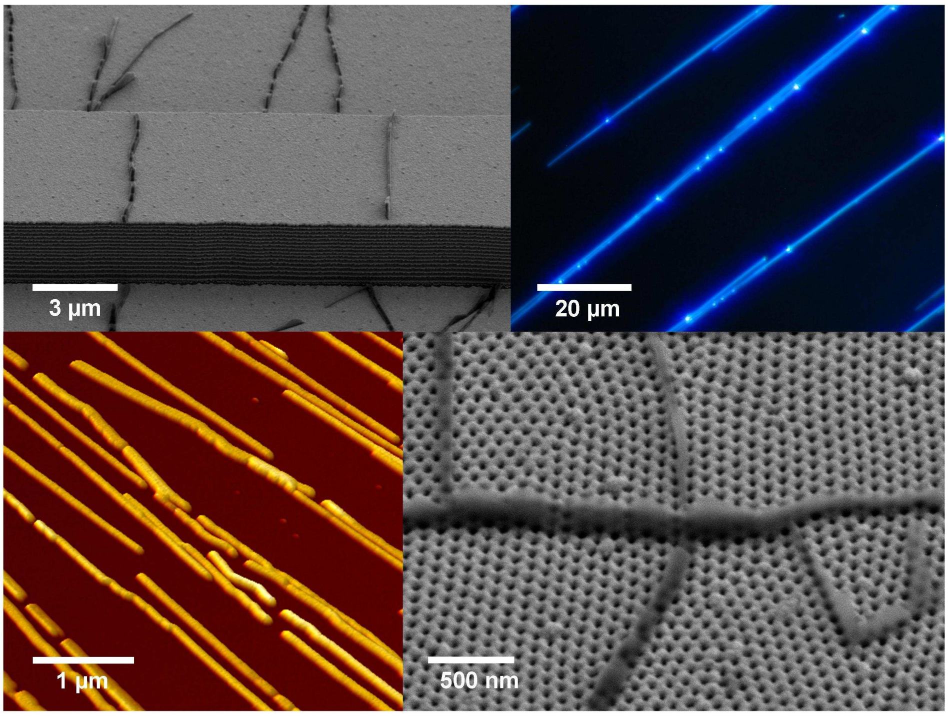

Morten Madsen

July 15, 2009

Preface

This thesis is part of the requirements for achieving the Ph.D. degree at the University of Southern Denmark (SDU). The main part of this work has been carried out at the Mads Clausen Institute at SDU in Sønderborg and a minor part has been performed at SDU in Odense. At the Mads Clausen institute (MCI) I have been working at the NanoSYD group. The project has been supervised by Professor Horst-Günter Rubahn as main supervisor and Professor Morten Willatzen as project supervisor. Apart from this thesis, a number of other publications has also been made during this project, these are listed in appendix B.

I would like to acknowledge several people for their support during this project. This is in particular Horst-Günter Rubahn for his help, support and assistance on several aspects. I would also like to thank my colleagues at NanoSYD for their help and kindness along the way. Ideas and creative solutions to scientific problems often come along more informal discussions within a group, this I have experienced personally during this project. A special thanks to Jakob Kjelstrup-Hansen for help on different aspects. Furthermore, I would like to thank Niels Lervad Andersen for support and discussions.

I have been working together with some collaborative groups, to whom I owe thanks. This is the S. Tamulevicius group from the Institute of Physical Electronics, Kaunas University of Technology, Lithuania and the M. Es-Souni group from the Institute for Materials and Surface Technology, University of Applied Sciences, Kiel, Germany.

July, 2009

Morten Madsen
Mads Clausen Institute
University of Southern Denmark
Alsion 2
6400 Sønderborg
Denmark

Abstract

This thesis is focused on directed growth of organic nanofibers on structured gold surfaces. In the past years, growth of phenylene-based organic nanofibers has been investigated thoroughly. One interesting model system is growth of *para*-hexaphenylene (p6P) nanofibers on muscovite mica, where the molecules self-assemble into mutually parallel nanofibers, when deposited on the heated mica surface in a high vacuum environment [1, 2]. These nanofibers emit intense blue, polarized, anisotropic light under UV excitation [1] and show both waveguiding [3] and lasing [4] properties, which make them interesting candidates as components in new types of optoelectronic devices. However, the lack of ability to pre- or post-process muscovite mica puts severe restraints in its use as a device substrate. Although several transfer techniques have been employed in order to transfer the nanofibers to more device applicable substrates [5], controlled transfer onto specific micrometer-sized regions defined by the substrate, while retaining the parallelism of the nanofibers, is not yet possible. Growth of p6P nanofibers on various other substrates such as Au(111) [6, 7], TiO_2 [8] and alkali halides [3, 9] has also been demonstrated, although without growth of long, mutually parallel nanofibers as in the case of muscovite mica.

In this work, growth of p6P nanofibers on structured gold surfaces is demonstrated as a method for obtaining mutually parallel nanofibers on substrates, which allow for pre- or post-processing. It is shown, that nanofibers can be grown on a non-structured gold film prepared by electron beam deposition unlike other metals such as aluminum, silver[1], titanium and chromium. Furthermore, structures, which guide the subsequent nanofiber growth, can be fabricated in the underlying substrate (silicon) prior to gold deposition. It is shown that both micron-sized ridges and channels guide the subsequent nanofiber growth into preferred directions perpendicular to the structures. Besides the orientation control of the nanofibers, the microstructures are also demonstrated to define the length of the nanofibers. Different parameters, which affect this growth mechanism such as the size of the structures and the substrate temperature during growth, are

---

[1] It should be noted, that short nanofibers can be grown on silver surfaces, if the surface temperature is sufficiently high.

investigated in detail in order to establish conditions for obtaining mutually parallel nanofibers with specific lengths on these substrates.

Nanostructured gold surfaces are also investigated as possible substrates for guided nanofiber growth. In this case, the structured gold surfaces are prepared by gold deposition on porous alumina templates, which lead to periodically nanostructured gold surfaces. Indications of guided nanofiber growth is also seen on these substrates, however, directed growth of nanofibers on a larger scale could not be observed as in the case of microstructured gold surfaces. This work therefore describes a method for achieving directed growth of organic nanofibers on structured gold surfaces and elaborates on several key points in this aspect. The method is believed to be useful for integration of organic nanofibers on device platforms.

Dansk resumé

Dette projekt er fokuseret imod retningsbestemt vækst af organiske nanofibre på strukturerede guld overflader. I de forgangne år er phenylene-baseret organiske nanofibre blevet grundigt undersøgt. Et interessant model system er vækst af *para*-hexaphenylene (p6P) nanofibre på muscovite mica, hvor selv-samlende molekyler danner indbyrdes parallelle nanofibre når de deponeres på den opvarmede mica overflade i et højt vakuum miljø [1, 2]. Disse nanofibre udsender intenst blåt, polariseret, anisotropisk lys under UV excitation [1] og viser både lysledende [3] og laser [4] egenskaber, hvilket gør dem til interessante kandidater som komponenter i nye typer af optoelektroniske devices. Den manglende formåen til at pre- eller post-processere muscovite mica har dog lagt begrænsninger på dets brug som device substrat. Selvom adskillige overførsels-teknikker har været brugt til at overføre nanofibrene til mere applikations-anvendelige substrater [5], har kontrolleret overførsel til specifikke mikrometer store områder defineret af substratet, imens paralleliteten af nanofibrene bevares, endnu ikke været muligt. Vækst af p6P nanofibre på forskellige substrater, såsom Au (1 1 1) [6, 7], TiO_2 [8] og alkalihalogen forbindelser [3, 9] er også blevet demonstreret, dog uden vækst af lange, indbyrdes parallelle nanofibre, som det er tilfældet med muscovite mica.

I dette arbejde demonstreres vækst af p6P nanofibre på strukturerede guld overflader, som en metode til at opnå indbyrdes parallelle nanofibre på substrater, som tillader pre- og post-processering. Det vises, at nanofibre kan gros på ustrukturerede guld overflader, forberedt ved elektron stråle deponering, i modsætning til metaller som aluminium, sølv[2], titanium og krom. Ydermere kan strukturer, som dirigerer den efterfølgende nanofiber vækst, fabrikeres i det underliggende substrat (silicium) før guld deponering. Det vises, at både mikrometer store højderygge og kanaler dirigerer den efterfølgende nanofiber vækst i foretrukne retninger vinkelret på strukturerne. Ud over kontrol af nanofibrenes retning, demonstreres det også, at mikrostrukturene definerer nanofibrenes længde. Forskellige parametre som påvirker denne vækst-mekanisme, såsom størrelsen af strukturerne

---

[2] Det skal nævnes, at korte nanofibre kan gros på sølv overflader, hvis overfladetemperaturen er tilstrækkelig høj.

og substrat temperaturen ved væksten, er undersøgt i detaljer, således at betingelser for at opnå indbyrdes parallelle nanofibre med specifikke længder på disse substrater kan etableres.

Nanostrukturerede guld overflader er ligeledes undersøgt som mulige substrater til at dirigere nanofiber vækst. I dette tilfælde er de strukturerede guld overflader forberedt ved guld deponering på porøse aluminiumoxid skabeloner, som fører til periodisk nanostrukturerede guld overflader. Indikationer på dirigeret nanofiber vækst ses også på disse substrater, men retningsbestemt vækst af nanofibre over større områder kunne ikke observeres, som det er tilfældet med mikrostrukturerede guld overflader. Dette arbejde beskriver derfor en metode til at opnå retningsbestemt vækst af organiske nanofibre på strukturerede guld overflader, og uddyber nogle vigtige punkter af dette aspekt. Metoden menes at være brugbar til integration af organiske nanofibre på device platforme.

Contents

Chapter 1

Introduction

1.1 Microtechnology and nanotechnology

From the middle of the last century, microtechnology, and especially microelectronics, found its break-through and revolutionized the existing technologies [10]. Top-down fabrication of micrometer-sized components, defined by optical lithography, became the standard for fabrication of integrated circuits and had a huge impact on the computer industry. During the years, a continuous effort was put in to further downscale the size of the components, in order to continuously increase the computation capacity of computers, which had grown exponentially as predicted by Gordon E. Moore, called Moore's law [11].

The downscale in size has today pushed the top-down fabrication close to its limits, with characteristic structure sizes well within the nano-regime, i.e. well below 100 nm [12]. In this strive towards miniaturization, a conceptually different method compared to top-down technology is being explored, namely bottom-up technology. Here, instead of decreasing the size of a larger object, the structures are built by assembly of individual building blocks such as atoms or molecules. The size of these structures are therefore not limited by the precision with which one can structure an object. Instead, it is essentially limited by the size of the individual building blocks themselves. Examples of structures fabricated by each method are given in figure 1.1.

This significant downscaling opens up for new physical considerations, which are inherently different from those related to bulk or micron-sized materials. First of all, the impact from forces, which are important in a macroscopic context, may become irrelevant in a nanoscopic context and vice versa. Gravity for example has an insignificant effect on nano-objects, whereas surface forces such as Van der Waals forces become dominant. The impact on a object by photons is also very different in the nano-regime, since it is easily possible, due to their small sizes, to manipulate and move nano-

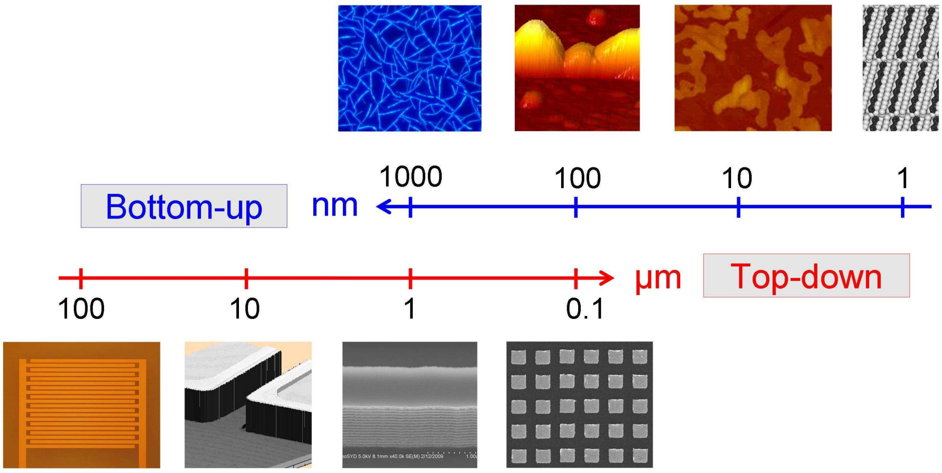

Figure 1.1: Schematic of top-down fabricated micro- and nano-structures and bottom-up assembled organic nanostructures with characteristic sizes.

objects with light [13]. Furthermore, the ability to synthesize molecules and nanostructures with a high precision of size, shape and composition, in principle at an atomic level, has opened for novel classes of materials with unique properties. Examples are 1-D nanostructures, such as nanotubes and nanowires [14, 15], and 0-D nanostructures, such as quantum dots [16], with striking electrical and optical properties. At sizes well below 100 nm, quantum mechanical effects may arise, which give rise to fundamentally new properties of materials, such as for example tuning of the energy bandgap in semiconductors by size reduction. Several remarkable examples such as single-electron transistors based on carbon nanotubes [17] and quantum dots [18] have been demonstrated as a result of quantum confinement.

Therefore, although nanotechnology has not yet had the commercial break-through in all the areas in which it was predicted to have big impact, it is foreseen a future as bright as for microtechnology many years ago. Back in 1959, Richard Feynman gave his famous speech at Caltech, in which he stated: "*There's plenty room at the bottom*" [19], meaning that by working with atoms, one could build up a huge number of different systems, which could potentially revolutionize existing technologies. In the decades to come, he was indeed proven right.

1.2 One-dimensional nanostructures

One dimensional (1-D) nanostructures are objects with a height and width below 100 nm, whereas the length of the objects is large. There exist many different kinds of 1-D nanostructures in the form of nanotubes, nanoribbons, nanowires, nanofibers and more. It should be noted however, that the distinction between a nanowire and nanofiber is often unclear, and both terms have been used in the literature for the same type of structure. In this work, the term nanofiber is used only for the special type of phenylene-based nanofibers, which are studied in this work, otherwise the term nanowire is used.

In the recent years, such 1-D nanostructures have obtained a huge interest within the scientific community, due to their large application potential within for example sensing [20, 21, 22, 23], electronics [24, 25], photovoltaics [26, 27] and opto-electronics and photonics [28, 29]. This potential arises from the fundamental properties of these structures, which are closely related to the downscaling of their dimensions. Their surface to volume ratio is increased, and electrons and photons are much better confined as compared to micron-sized components. 1-D nanostructures are the objects with the smallest dimensionality that can transport electrons and optical excitations. This makes them very interesting as nanoscaled components in devices. Especially carbon nanotubes [14, 30] have been demonstrated to function as novel components in electrical devices, but also inorganic semiconducting nanowires [15] have had a major break-through within numerous devices. This is for example silicon nanowires, which have effectively been employed as new field-effect transistors [31]. Furthermore, III-V inorganic semiconducting nanowires have been widely used within light-emitting diodes [32] and lasers [33], areas where a special type of organic nanofibers [1] also have found interest.

When fabricating a device based on 1-D nanostructures, there are in general three critical aspects to consider, in order to make the device work. First of all, the desired device functionality is essential for the choice of nanostructure fabrication and integration. Secondly, the 1-D nanostructures need to be fabricated in a controlled way, so that they meet the demands for their use, i.e. their size, crystallinity, purity etc. need to be controlled. Thirdly, the 1-D nanostructures need to be integrated into a device platform. Typically this means, that they should be placed in a specific way on the device platform, for example on specific micrometer-sized regions defined on the platform. This could also include additional fabrication steps, for example in order to establish electrical contact to the nanostructures. Examples within each area are shown in figure 1.2 and explained in the following.

It should be noted, that the different aspects depend critically on each other. When fabricating a specific type of device, one has to consider which type of nanostructure to use, in order to meet the demands for the function of the device. The integration is then performed by using a method, which is suitable for the specific type of nanostructure. This can either be by transferring the nanostructures onto the device platform or by *in-situ* growth (sec. 1.2.2). In the latter case, the nanostructure fabrication and integration is performed simultaneously. Afterwards, the steps which make

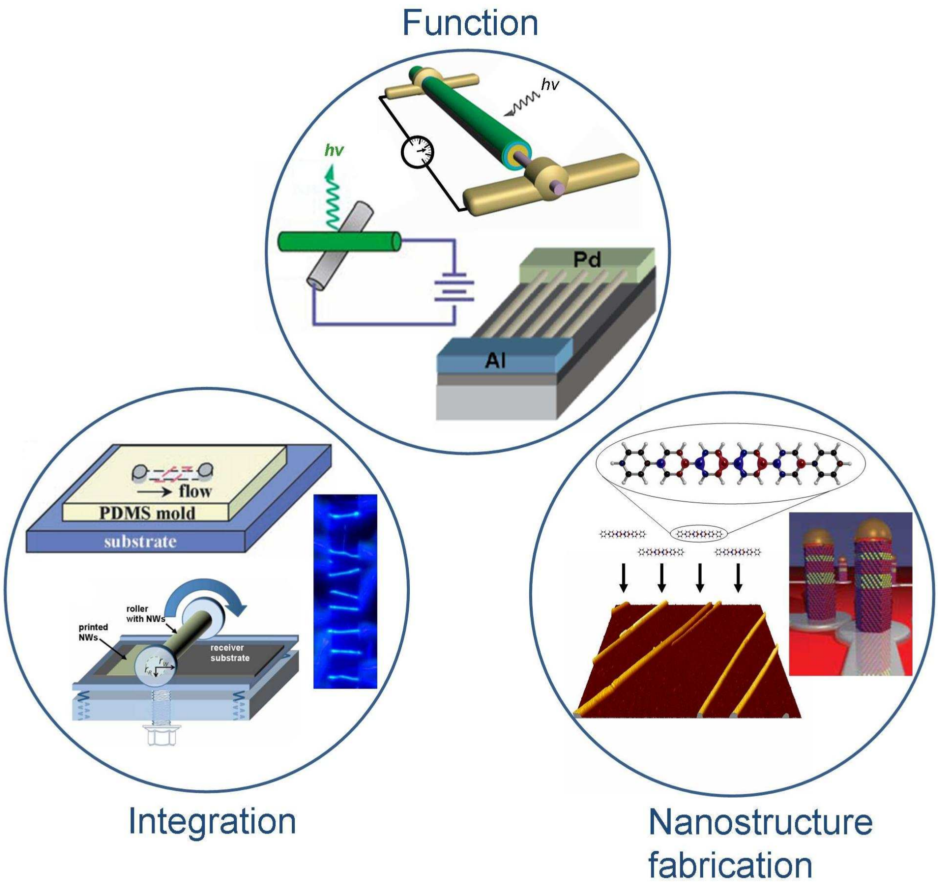

Figure 1.2: Examples from each of the three different areas needed for fabrication of devices based on 1-D nanostructures: Nanostructure fabrication: Organic nanofibers and seeded bottom-up nanostructure fabrication [34]. Integration: Roll printing [35], fluidic alignment [36] and *in-situ* growth. Function: Solar cells [37], diodes on flexible substrates [38] and light emitting-diodes [28].

the device function are employed in a way, which is compatible with both the type of nanostructure and integration method. Therefore, one needs to consider solutions within each step carefully, before the desired device can be fabricated. In this work, the focus is on growth and integration of organic nanofibers. Therefore, the function of these devices is only considered briefly throughout this work.

1.2.1 Fabrication of one-dimensional nanostructures

Many different top-down or bottom-up methods have been used in order to fabricate 1-D nanostructures. As for top-down fabrication, conventional methods such as lithography [39] is often employed. However, the small scales of the structures and the request for using other than conventional microfabrication compatible materials, have increased the use of bottom-up methods and materials. However, different combinations of top-down and bottom-up methods, such as placement of catalyst particles by laser ablation [40] or electron beam lithography [41] for subsequent bottom-up growth of nanowires, have been proven successful.

In the case of bottom-up processes, synthesis from the vapor phase of the materials are typically employed. This can be done either by direct vapor phase methods [42], i.e. without relying on any catalytic particles, or from the more well known vapor-solid-solid (VSS) [43] or vapor-liquid-solid (VLS) [44, 45] methods. Especially the latter is probably the most successful for fabricating single-crystalline nanowires today. Examples of template assisted synthesis have also been widely demonstrated [46, 47], which can be performed either from the vapor or liquid phase of different materials. In general, nanowires can be grown either epitaxial or non-epitaxial depending on the material and substrate used. Many examples of epitaxially grown nanowires have been demonstrated, such as vapor phase epitaxial (VPE) growth of inorganic semiconducting nanowires [48] or molecular beam epitaxial (MBE) growth of semiconducting organic nanofibers [49]. Today, such techniques are standard in the fabrication of various kinds of crystalline nanowires with tailored dimensions of both organic and inorganic materials [21]. In this work, organic nanofibers are grown from vapor deposition of the organic material on different substrates. Examples of both epitaxial and non-epitaxial growth of these nanofibers will be demonstrated.

1.2.2 Integration of one-dimensional nanostructures

Integration of nanowires is a key aspect in the fabrication of nanowire based devices. Often, highly controlled integration on well defined regions is needed, which sometimes is a bottle-neck in exploration of the unique properties of nanowires. Different methods can be applied depending on the specific type of nanowires, which need to be integrated. In general, integration can be done either by transferring the nanowires from the growth substrate to the desired device platform or, by *in-situ* growth, i.e. growth of nanowires directly where they are needed.

In the case of transferring, many examples within inorganic nanowires have been employed for transferring an ensemble of wires. These rely on for example contact printing [38, 50], roll printing [35] (fig. 1.2) or fluidic integration [36] (fig. 1.2). Methods for transferring organic nanostructures have also been demonstrated [5], although not on such a large scale as for the inorganic nanowires. Nanofibers can also be transferred by simple drop-casting of a nanofiber suspension on a substrate, and then afterwards manipulate the nanofibers mechanically [17, 51, 52] in order to achieve the desired configuration. Several considerations besides position and orientation need to be considered during these transfer processes. This is for example how to avoid contamination of the wires during the transfer process and also how to avoid damaging of the individual wires, which for example is a problem in the case of organic nanofibers due to their mechanically fragile nature (van der Waals bound molecules) [51, 52].

During the years, many different methods for *in-situ* growth of nanowires have been employed. Typically, these rely on carefully placement of a catalyst particle, from where the nanowire growth starts. As mentioned earlier, conventional top-down fabrication methods are normally used for defining the placement of the catalyst particles, such as optical [53] or electron beam [41] lithography, followed by bottom-up growth of the nanowires. The orientation of the grown nanowires can be controlled in different ways, typically they are epitaxially defined [41], but for example electric-field alignment has also been demonstrated [53].

Both for transferring and *in-situ* growth, the different techniques employed depends critically on the system, i.e. on the type of nanowires and the device substrate, and therefore it is difficult to make any general statement regarding advantages and disadvantages for the two integration methods. However, for 3-D integration of nanowires where transferring is difficult, *in-situ* growth has a clear advantage. One example is placement of carbon nanotubes at silicon cantilever tips for scanning probe microscopy. Here, transferring is only realistic in small numbers, due to the time consumption of the method [54], instead, *in-situ* growth has allowed for wafer scale integration of carbon nanotubes at such tips [55]. However, nowadays, transferring at a wafer scale is possible in other configurations [38], and therefore the type of method which is beneficial depends on the individual system investigated.

In this work, a new method for achieving *in-situ* growth of organic nanofibers on microstructured gold surfaces will be demonstrated.

1.3 Organic nanofibers

As already mentioned, this project is focused on growth and integration of a special kind of organic semiconducting nanofibers. Organic semiconductors have in general many advantages, such as large-scale synthesis, solution-processability, optical and electrical tunability by molecular design and easy and low cost fabrication and mechanical flexibility [56, 57]. Among organic molecules, oligomers built up of π-conjugated systems have received a lot of attention due to their interesting optical, electrical and optoelectronic properties. Especially rod-like molecules such as pentacene [58], oligo-thiophenes [59] and oligo-phenylenes [60, 1] are among those studied the most. Among devices built from these systems are for example organic transistors [61], organic light emitting diodes [62, 63] and photovoltaic cells [64, 65, 66]. In general, the performance of such devices is critically determined by how the molecules assemble in the solid state [67]. Today, it is possible to fabricate one-dimensional, crystalline organic nanofibers with very few defects, which make them important model systems for both fundamental studies and device applications.

Examples of the type of nanofibers investigated in this project are shown in figure 1.3. The nanofibers are grown from physical vapor deposition of the organic molecules on different substrates at elevated temperatures; the main substrate explored in this project is gold. Typical dimensions of the nanofibers are shown in the figure, however, all three dimensions of the nanofibers can be varied by changing the growth conditions [1].

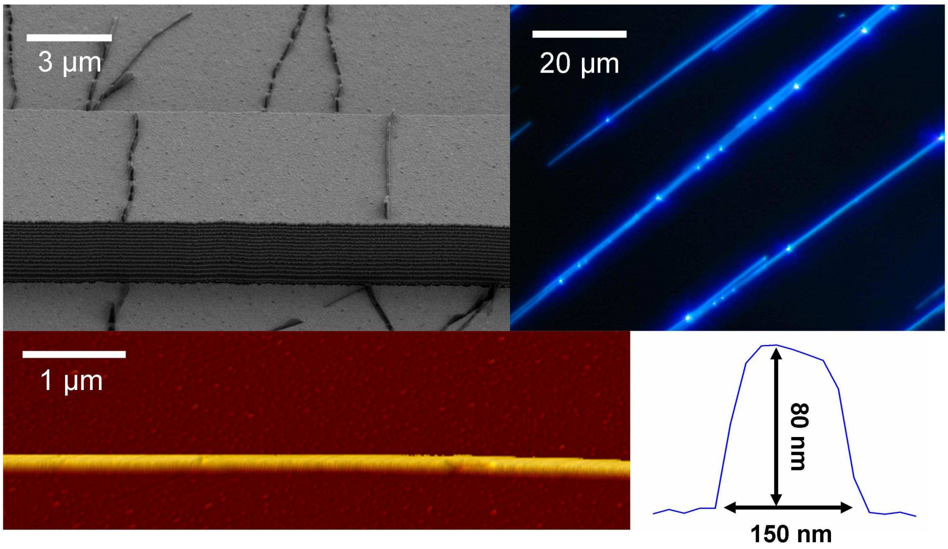

Figure 1.3: fluorescence microscopy (top right) and AFM (lower) image of nanofibers grown on mica along with measured dimensions. SEM image (top left) of nanofibers grown on a gold coated silicon microstructure.

These nanofibers emit intense, polarized, anisotropic, blue light under UV excitation [1] and show both waveguiding [3] and lasing properties [4], which makes them interesting for optical and opto-electronic applications. However, the lack of ability to integrate these nanofibers in a controlled way usually hinders their implementation in devices. Although several transfer techniques from the growth template (usually muscovite mica) to a device substrate have been demonstrated, transferring of mutually parallel nanofibers at specific micron-sized regions defined by the device substrate is so far not accomplished. A different approach, which relies on *in-situ* growth of the nanofibers directly at nano- and micro-structured substrates, are investigated as the key topic in this work.

Chapter 2

Experimental

2.1 The organic molecular beam epitaxy system

The organic molecular beam epitaxy (OMBE) system used for growth of *para*-hexaphenylene nanofibers is described in the following. The system is a two chamber system, which consists of a transfer chamber and a main chamber[1] (fig. 2.1).

The first step in a growth process is to introduce a growth substrate into the transfer chamber, which is sealed off from the main chamber by a pneumatic valve (1). This is done by fixing the substrate mechanically on a sample plate and then connect it to a magnetically driven transfer rod (2) in the transfer chamber. After pump down of the transfer chamber, the sample plate can be introduced into the main chamber by opening the pneumatic valve and transfer it with the magnetically driven transfer rod. The sample plate is placed in a sample holder in the main chamber, figure 2.2a. The sample holder can be heated to the desired temperature by the use of two thermo coax cables, which are integrated in the sample holder. The temperature is measured with a type K thermocouple[2]. The sample holder is connected to a manipulator (3), which makes it possible to rotate the holder and to move it in a vertical direction. Below the sample holder, a water-cooled quartz microbalance is placed in order to measure the deposition rate and nominal thickness of the deposited film. Once the substrate temperature is reached, the oven (4) can be heated. The oven consists of a home built

---

[1] This system was developed and built by: Henrik H. Henrichsen, Morten Madsen, Ralf Frese and Kasper Thilsing-Hansen.

[2] $http://srdata.nist.gov/its90/main/its90_main_page.html$. It should be noted that although the thermocouple has not been calibrated, measurements of the temperature dependence on p6P nanofiber dimensions on muscovite mica have shown quantitatively same results as reported by others (sec. 3.4.2) and the measured temperatures are therefore assumed to be correct. Furthermore, since small variations in the temperature occur across the sample plate when heated, special care has been taking in mounting the substrates in the same way for each deposition, in order to allow for direct comparison between the samples.

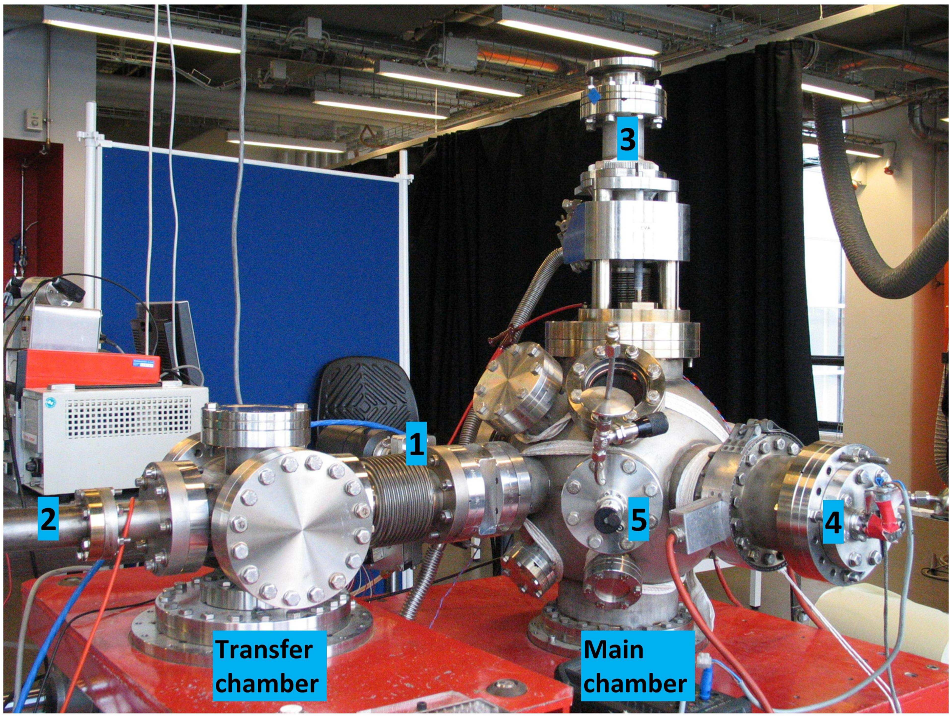

Figure 2.1: The organic molecular beam epitaxy system used for growth of p6P nanofibers.

Knudsen cell wrapped in a thermo coax cable, which is connected to a type K thermocouple, figure 2.2b. The oven is furthermore wrapped in a heat shield.

The typical temperature for the sublimation process to take place is around 670 K. A shutter (5) is placed in front of the Knudsen cell, which is opened once the desired rate (typically 0.1 Å/s) is reached. After deposition, the sample plate is cooled in the sample holder for approximately 30 minutes, simply by turning off the heating of the holder, before it is transferred back to the transfer chamber, which is then sealed and vented.

2.2 Characterization equipment

In this section, the characterization equipment used in this project is briefly described along with some considerations regarding the influence of the equipment on the measurements. The following characterization equipment is used in this project:

- **Fluorescence microscope** from Nikon, model: Eclipse ME600D. Hg lamp, peak wavelength of ≈ 365 nm. Used for investigating morphol-

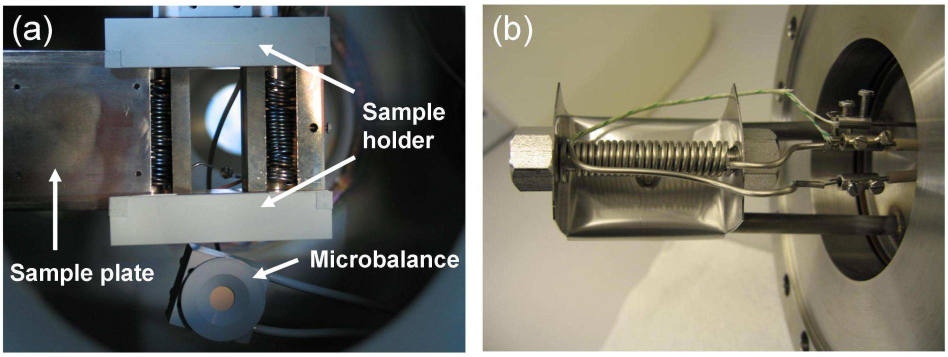

Figure 2.2: (a) Image of the sample holder and the sample plate which is introduced into the holder. A microbalance is placed below the sample holder. (b) Image of the Knudsen cell wrapped in thermo coax cables and with a connected thermocouple (design and image by Henrik H. Henrichsen).

ogy, fluorescence spectra and polarization properties of the organic nanoaggregates.

- **Interference microscope** from Fogale nanotech, model: Microsurf 3D. Lateral resolution is diffraction limited to ≈ 0.6 μm, vertical resolution can reach 0.1 nm. Can scan profiles with heights up to 400 μm. Used for measuring 3-D profiles of the fabricated microstructures in silicon.

- **Atomic Force Microscope (AFM)** from JPK, type: Nanowizard. Used for investigating the morphology of nanoaggregates and thin films.

- **Scanning Electron Microscope (SEM)** from Hitachi, model: S-4800 Field Emission Scanning Electron Microscope. Resolution of 2.0 nm at an accelerating voltage of 1 kV and a magnification up to 800.000 times. Used for investigating the morphology of organic nanoaggregates and fabricated nano- and micro-structured templates.

The organic nanofibers, which are investigated in this project, are mechanically fragile (van der Waals bound molecules), and special care must be taken in order not to damage the nanofibers during characterization. Bleaching of the nanofibers may occur during fluorescence microscopy measurements [68], however, this can be avoided by using relatively low intensities and short integration times. AFM measurements may also damage the nanofibers [52], however, by scanning in intermittent contact mode with an appropriate set-point value, non-destructive AFM measurements of the nanofibers can be made.

In terms of damaging the nanofibers during characterization, SEM measurements are the most critical characterization tool. Several measurements was made in order to investigate possible effects from electron beam irradiation on the organic nanofibers, the results are described in the following.

2.2.1 P6P nanofiber characterization with SEM

The ability of the SEM to operate at low voltage (down to 100 V), makes it possible to examine poor conductive material, such as the organic nanofibers, without detecting any noticeable charge build-up during the scans. However, when high voltages are employed, or when the exposure time is too long (i.e. when the electron dose is large), effects such as charging and radiation-induced modifications of the nanofibers can be seen. Figure 2.3 shows SEM images of the same area of nanofibers taken at different voltages[3], starting from 100 V (fig. 2.3a) to 300 V (fig. 2.3b) and finally 600 V (fig. 2.3c). It is seen, that the different image conditions modifies the measured nanofibers. Clearly a different image contrast is observed at 600 V compared to 100 V, which is due to the higher electron energy. It should be noted that the nanofibers, that are examined in these experiments, are transferred from their growth substrate (muscovite mica) to silicon(100), in order to avoid charging effects from the substrate.

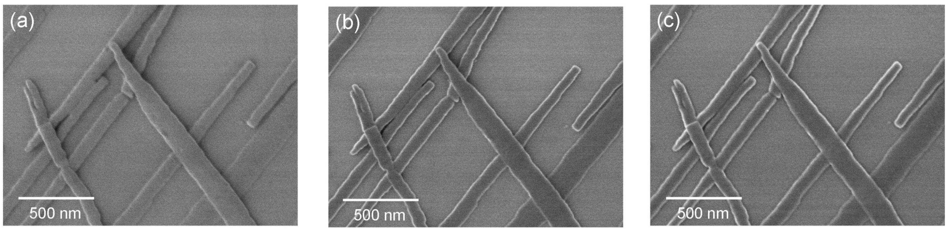

Figure 2.3: SEM images of p6P nanofibers on silicon imaged with (a) 100 V, (b) 300 V and (c) 600 V. A magnification of 50.000 was chosen during the SEM measurements.

Also effects from increasing the electron beam exposure time have been investigated. This is demonstrated in figure 2.4 which shows SEM images of nanofibers from the same area after exposing it for 0 minutes (fig. 2.4a), 10 minutes (fig. 2.4b) and 20 minutes (fig. 2.4c), respectively. It is seen that the nanofibers appear bigger, when the exposure time is increased. This increase of the nanofiber dimensions have been verified by AFM measurements [69].

---

[3] A de-acceleration voltage of 1.500 V was used in all experiments. The voltage here refers to the effective voltage, i.e. the accelerating voltage minus the de-accelerating voltage. A beam current of 10 μA was used in all experiments in this section.

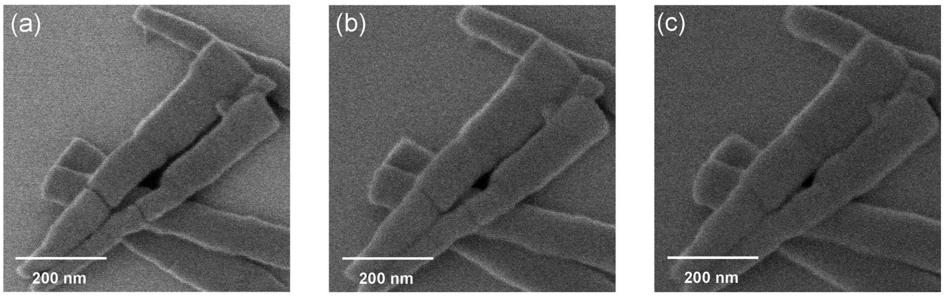

Figure 2.4: SEM images of p6P nanofibers on silicon. The area has been scanned for (a) below a minute, (b) 10 min and (c) 20 min. The voltage was 200 V. A magnification of 50.000 was chosen during the SEM measurements.

Additional information on the modification of the nanofibers during electron beam irradiation can be obtained by fluorescence microscopy investigations. Figure 2.5 shows fluorescence microscopy images of p6p nanofibers grown on a Au surface, after they have been exposed to electron beam irradiation (acceleration voltage was 1.000 V). Only the center part of the images have been exposed to the electron beam. It is seen, that the nanofibers change their fluorescence properties after they have been exposed to the beam. After 20 s of exposure (fig. 2.5a), the exposed nanofibers start to become dim, whereas after 180 s of electron beam exposure (fig. 2.5b) the nanofiber fluorescence seem to exhibit a redshift.

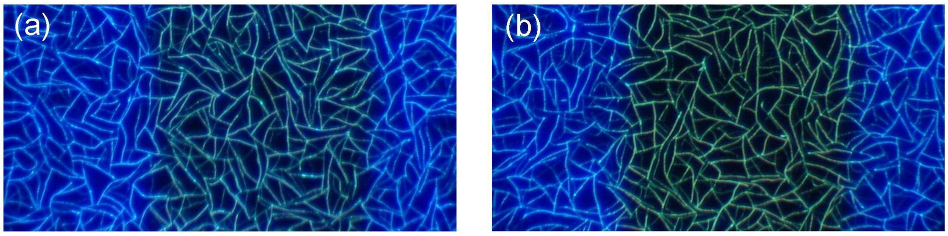

Figure 2.5: Fluorescence microscopy images of p6P nanofibers exposed to electron beam irradiation for (a) 20 s and (b) 180 s. The electron beam voltage was set to 1.000 V. The nanofibers are grown on a gold surface.

Detailed analysis of the changing fluorescence properties are obtained from fluorescence spectra from the exposed areas of the nanofibers (fig. 2.6). Nanofibers exposed to 1.000 V (left) and 30.000 V (right) for 0 s, 20 s and 180 s are examined. The reference spectrum (0 seconds of e-beam illumination) shows the known relation between the (0-1), (0-2) and (0-3) optical transition peaks for p6P nanofibers (see fig. 3.2). It should be noted that the (0-0) transition is not present in these spectra, due to the presence of a UV filter in the microscope (cut-off wavelength at 420 nm). The spectra are normalized, so that the intensity of the (0-1) peak is 1, i.e. the total intensity can not be deduced from the spectra.

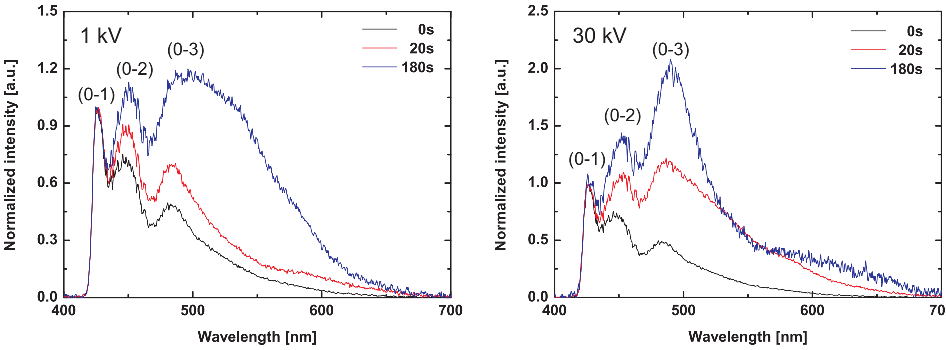

Figure 2.6: Fluorescence spectra from p6P nanofibers exposed to electron beam irradiation with a voltage of 1.000 V (left) and 30.000 V (right). The nanofibers have been exposed for 0 s, 20 s and 180 s, respectively. The nanofibers are grown on a gold surface.

It is seen, that the amplitude of the (0-1), (0-2) and (0-3) transitions change relative to each other. This is the case both for the 1 kV and 30 kV measurements, where the intensity of the (0-2) and (0-3) transition increase relative to the (0-1) transition. In the 30 kV measurements, the increase is more pronounced than in the 1 kV measurements, due to the higher electron energy. This change could be due to damage or defects in the nanofibers, which appear as a consequence of the electron irradiation. Furthermore, besides the change in intensity ratio between the peaks, a new, broad emission peak appears above 500 nm, and a small peak at around 600 nm. This indicates a change in the molecular structure of the nanofibers for example due to electron-induced polymerization of the nanofibers. Indications on electron-induced polymerization have also been observed for p4P nanofibers [70].

In summary it can be concluded, that fast scans and low voltages (maximum around 1 kV) should be used in order to make non-destructive characterization of the nanofibers by SEM. If too high voltages or too long scan times are chosen, damage and modifications of the nanofibers take place, which clearly change the optical properties and morphologies of the fibers.

2.3 Optical lithography - process recipe

The recipe used for the optical lithography is described in the following. The aim of the lithography and subsequent etching is to fabricate microstructured ridges in silicon, which afterwards can be used as templates for nanofiber growth (see section 4.1). An optical microscopy image of the lithography mask is shown in figure 2.7.

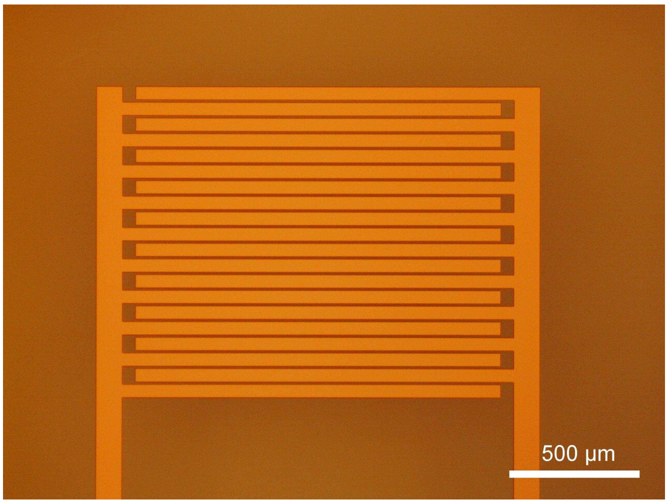

Figure 2.7: Optical microscopy image of the mask employed for the optical lithography.

The mask consists of parallel arrays of metal lines with gaps of a few micrometer in between. In order to produce micrometer sized ridges, negative lithography was chosen. The steps are as follows:

1. **Wafer:** The start wafer is a 4 inch silicon(100) wafer.
2. **HMDS treatment:** A monolayer of adhesion promoter Hexamethyldisilane (HMDS) is deposited on the clean wafer at 130° C, in order to enhance resist adhesion.
3. **Resist spincoat:** Photoresist (type: AZ5214E) is spin-coated on the wafer, first at 500 rpm for 5 sec. then at 4000 rpm for 30 sec. The resulting resist layer is approx. 1.5 μm thick.
4. **Prebake:** The resist coated wafer is prebaked at 90° C for 1 min.
5. **UV exposure:** UV exposure is performed in a MA150 mask aligner from Karl Süss (soft contact mode, approx. 1.5 sec.).
6. **Inversion bake:** Inversion bake is done at 120° C for 100 sec.

7. **Flood exposure:** UV flood exposure without mask is done for 25 sec.

8. **Develop:** The resist is developed for 1 min (in a AZ351B developer) with subsequent water rinse for 2 min.

After the optical lithography steps, silicon is selectively etched by reactive ion etching, which will be described in the next section.

2.4 ICP-RIE etching

The etching is performed in an inductively coupled plasma reactive ion etching (ICP-RIE) system from Alcatel (type: AMS 110). The BOSCH process, which uses a mixture of SF_6 and C_4F_8, is used for etching of the silicon wafers. In the BOSCH process, SF_6 is used as the active etch gas and C_4F_8 is introduced in order to passivate the sidewalls in between the etch cycles. The passivating layer is preferentially removed from the bottom of the trenches by ion bombardment during the etch cycles, whereas etching of the sidewalls is hindered by the passivating layer. This results in a highly anisotropic etch. After etching, the resist is removed in acetone (5 min.) and subsequently cleaned in an oxygen plasma.

Several parameters influence the final etch result in the BOSCH process. A list of these is given in table 2.1.

Etch cycle time	Passivation cycle time
SF_6 flow rate	C_4F_8 flow rate
Etch cycle coil power	Passivation cycle coil power
Etch cycle chuck power	Passivation cycle chuck power
Etch cycle pressure	Passivation cycle pressure
Wafer temperature	Wafer distance from source plasma

Table 2.1: List of parameters which influence the silicon etching in a BOSCH process [71].

The listed parameters and the balance between the etch and passivation determine the etch process. This includes parameters such as the silicon etch rate, the photoresist etch rate, the profile angle and the sidewall roughness or the size of the scallops, which originate from the alternating etching (SF_6) and passivating (C_4F_8) cycles. Several studies describe the influence of the different parameters in details [71, 72, 73, 74].

In this work, deep etching profiles are not needed, and the silicon etch rate is considered to be less important. Instead, the focus has been on fabricating microstructures with a low line edge roughness, since this potentially has an effect on the subsequent nanofiber formation on the structures (section 4.1). Experimental investigations demonstrated, that a low line edge roughness was obtained by reducing the sidewall roughness. In general, several parameters affect the sidewall roughness such as the coil power [73] and the passivation cycle times [71]. However, a rather simple method for reducing the sidewall roughness is to reduce the overall cycle times, while maintaining the etch and passivation cycle ratio [74]. It should be noted that this also results in a lower etch rate. A standard recipe supplied by Alcatel and experimental investigations of some of the process parameters resulted in a process recipe, which has a silicon etch rate of 3 μm/min. The parameters are listed in table 2.2.

Process parameter	Gas independent	SF_6	C_4F_8	O_2
Gas flow - etch [sccm]	-	300	60	0
Gas flow - passivation [sccm]	-	0	200	25
Etch duration [s]	2.8	-	-	-
Passivation duration [s]	0.8	-	-	-
Chuck temperature [°C]	0	-	-	-
Chuck distance to source [mm]	120	-	-	-
Coil power [W]	1200	-	-	-
chuck high power (10 ms) [W]	90	-	-	-
chuck low power (90 ms) [W]	0	-	-	-

Table 2.2: List of parameters used for achieving an etch with reduced line edge and sidewall roughness. The silicon etch rate is 3 μm/min.

In this recipe, O_2 is applied in order to effectively remove the passivating layer at the bottom of the trenches [75], which thereby further increases the etch rate at the bottom of the trenches compared to the sidewalls [76].

A 10 μm wide microridge fabricated in silicon by the described recipe is shown in figure 2.8. The total process time for the etching step was 60 s. As it can be seen from the profile cross-section (measured by interference microscopy), the resulting depth is approx. 3 μm. The line edge roughness of the etched ridges was investigated by SEM, and showed a roughness below 50 nm. No further attempts to reduce the line edge roughness were made.

As a final test of the optimized process parameters for both the optical lithography and the subsequent reactive ion etching, a grating structure with a period of 2 μm was fabricated. The resulting structures are shown in figure 2.9. Although small variations appear across the wafer and on some of the structures, the final etch result, in terms of structure dimensions and periodicity, is believed to be sufficiently good for the work in this project, and no further optimization has been performed.

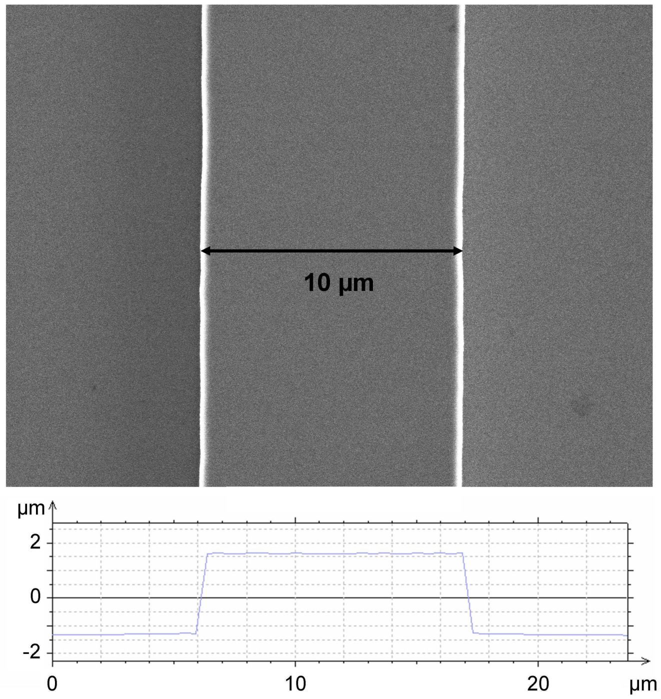

Figure 2.8: SEM image of a 10 micrometer wide ridge fabricated in silicon. The cross-section profile, measured by interference microscopy, reveal an etch depth of approx. 3 μm.

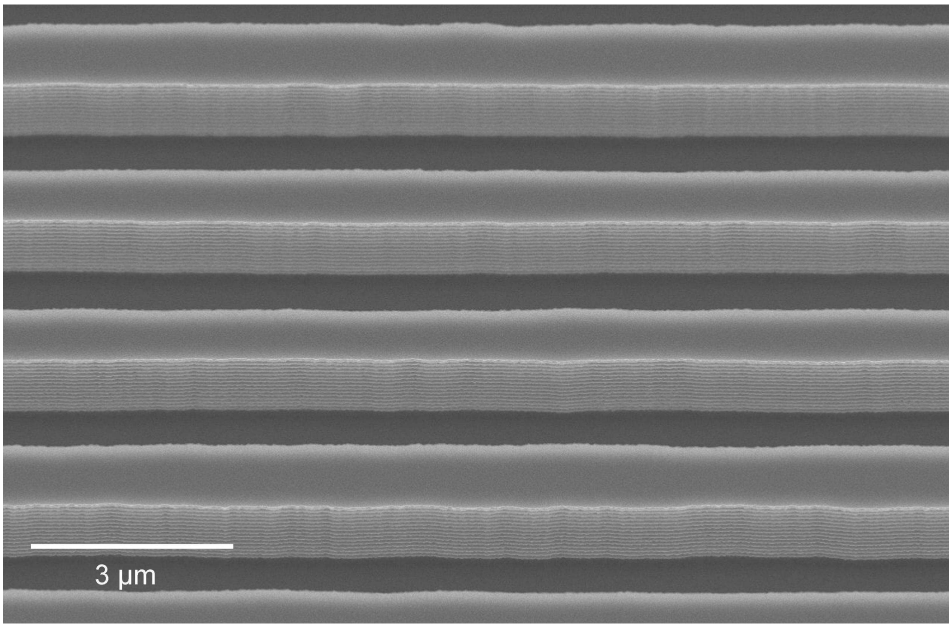

Figure 2.9: Tilted SEM image of a grating structure fabricated in silicon by optical lithography and subsequent reactive ion etching. The grating period is 2 μm.

Chapter 3

Nanofibers from *para*-hexaphenylene molecules

3.1 Introduction

This project is focused on nanofibers made from the rod-like molecule *para*-hexaphenylene (p6P). In a series of experiments in the past years it has been shown that nanofibers can be grown from this molecule on various substrates such as muscovite mica [49, 2], Alkali Halides [3, 9], TiO_2 [8] and Au [7, 6].

Especially the optical properties of p6P nanofibers have increased the interest for them in the past years. This is for example their ability to emit polarized, blue light after UV excitation [1] and their waveguiding [3, 9] and lasing [4] properties. One of the promising features of the nanofibers is the ability to tune their properties by chemical synthesis of the individual molecules prior to growth, which for example has led to second-harmonic generation in such nanofibers [57, 77]. So, although this work is based on p6P nanofibers alone, the growth and handling techniques of the nanofibers extend to other types of fibers as well. In this chapter, nanofibers made from p6P are described. This includes a general introduction to the p6P molecule along with the formation of crystal structures in thin films as well as in nanofibers, which mainly govern p6P nanofiber growth on muscovite mica and Au coated silicon.

It should be noted that growth of nanofibers on Au coated silicon is of special interest in this work. As it will be demonstrated in chapter 4, it is possible to structure silicon prior to nanofiber growth, and thereby modify or direct the nanofiber growth. However, in the present chapter only growth on planar Au coated silicon will be covered.

3.2 Molecular structure of *para*-hexaphenylene

Para-hexaphenylene ($C_{36}H_{26}$) is an oligomer of the conjugated polymer, poly-paraphenylene. It is a an aromatic molecule, which consist of six phenylene rings (Fig. 3.1). This type of molecule is especially interesting due to its promising application potential within electronic and opto-electronic devices, such as light emitting devices [78, 79, 80, 81] and thin film transistors [82].

The optical and electrical properties are mainly governed by the delocalized π electron system. In p6P, the carbon atoms hybridize to form three sp^2 orbitals and one 2p orbital. The sp^2 electrons form strong σ bonds while the remaining 2p electrons form π bonds, which are delocalized over the entire molecule. It is the π orbitals, that constitute the highest occupied molecular orbital (HOMO) and the lowest unoccupied molecular orbital (LUMO), which again, to a large extend, govern the optical and electrical properties in p6P.

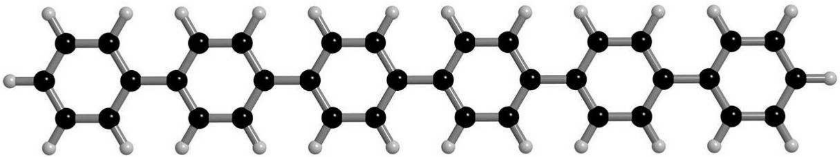

Figure 3.1: The p-6P molecule ($C_{36}H_{26}$) which consist of six phenylene rings.

In such organic molecules, which posses conjugated π electron systems, the π electrons are easily excited from the HOMO to the LUMO level. In the case of p6P, the energy bandgap is around 3.1 eV [83], which gives rise to blue fluorescence. When an electron is excited from the HOMO level to the LUMO level, an electron-hole pair (exciton) is generated, with a corresponding Coulomb force between them. The energy of this electron-hole pair is therefore smaller than the energy gap between the HOMO and LUMO levels, and thus, when the electron and hole recombine, the photo-emission occurs at energies that are lower than the bandgap. In the fluorescence spectrum of p6P, several peaks are visible, which correspond to transitions between the LUMO ground state and different HOMO vibrational states. This is demonstrated in figure 3.2, which shows a fluorescence spectrum from an ensemble of p6P nanofibers. It should be noted, that the fluorescence spectrum from a thin film of p6P shows the same characteristic as for an ensemble of nanofibers, although the ratio between the peaks change, and the peaks appear broader [84]. Both the (0-0), (0-1), (0-2) and (0-3) bands are clearly visible in the spectrum. The reason for the suppressed (0-0) band is re-absorption.

When discussing thin films, either continuous or an ensembles of nanofibers, an important aspect is that the optical and electronic properties of

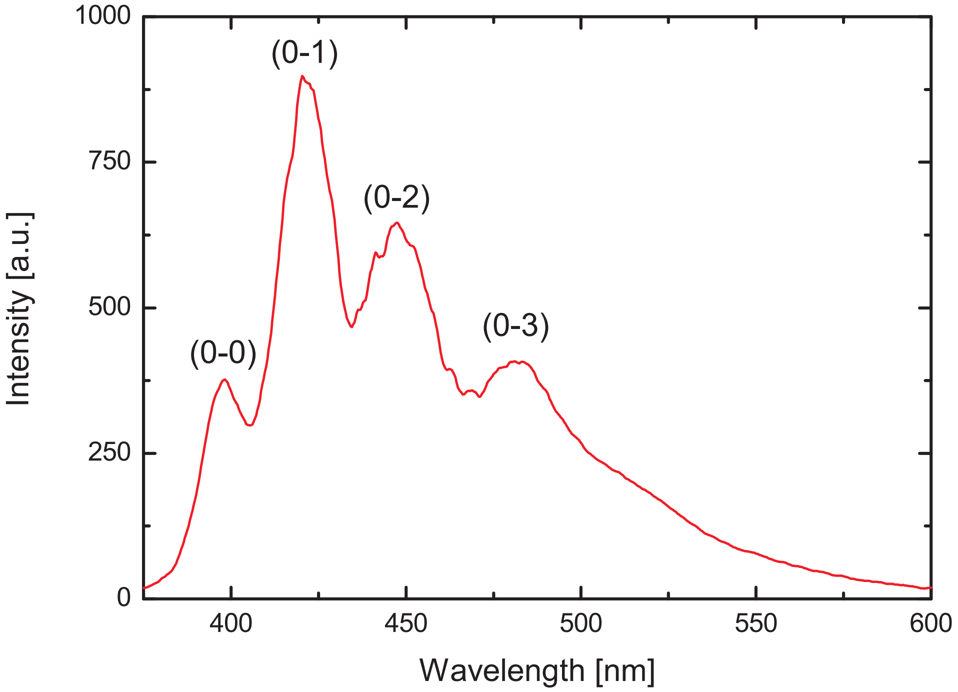

Figure 3.2: Fluorescence spectrum from an ensemble of p6P nanofibers grown on muscovite mica. Excitation wavelength at 325 nm.

these depend strongly on the orientation of the molecules, from which the thin films are assembled. For example does the optical absorption of p6P depend strongly on the orientation of the individual molecules relative to the surface of the substrate [85]. Furthermore it has be demonstrated that the internal alignment of the molecules in p6P based light emitting devices has a strong effect on the efficiency of the device [78]. Therefore, an understanding of the p6P crystal structure and the formation of p6P thin films on substrates is of crucial importance for the understanding of the properties of these devices. This will be described in the following sections.

3.3 Crystal structure of *para*-hexaphenylene

In the gaseous phase, p6P molecules are nonplanar with alternating torsion angles between adjacent phenyl rings of around 30° - 40° [86, 87]. This torsion is due to two competing forces between, on one hand, repulsion of positively charged orthohydrogens on neighboring rings, which forces the molecules into nonplanar configuration, and on the other hand, the delocalized π electron system, which tends to planarize the molecule. However, in a crystalline environment, the molecules are expected to be planar [86, 60].

Para-hexaphenylene crystallizes in a monoclinic lattice with $P2_1$ symmetry and lattice constants of $a = 8.09$ Å, $b = 5.57$ Å, $c = 26.24$ Å, and $\beta = 98.2°$ [86]. The molecules are packed in a herringbone structure, with the molecular axes parallel to each other (fig. 3.3a) and the molecular planes are tilted with 66° with respect to each other [60] as shown in figure 3.3b. This crystal structure is known as the β-phase of p6P.

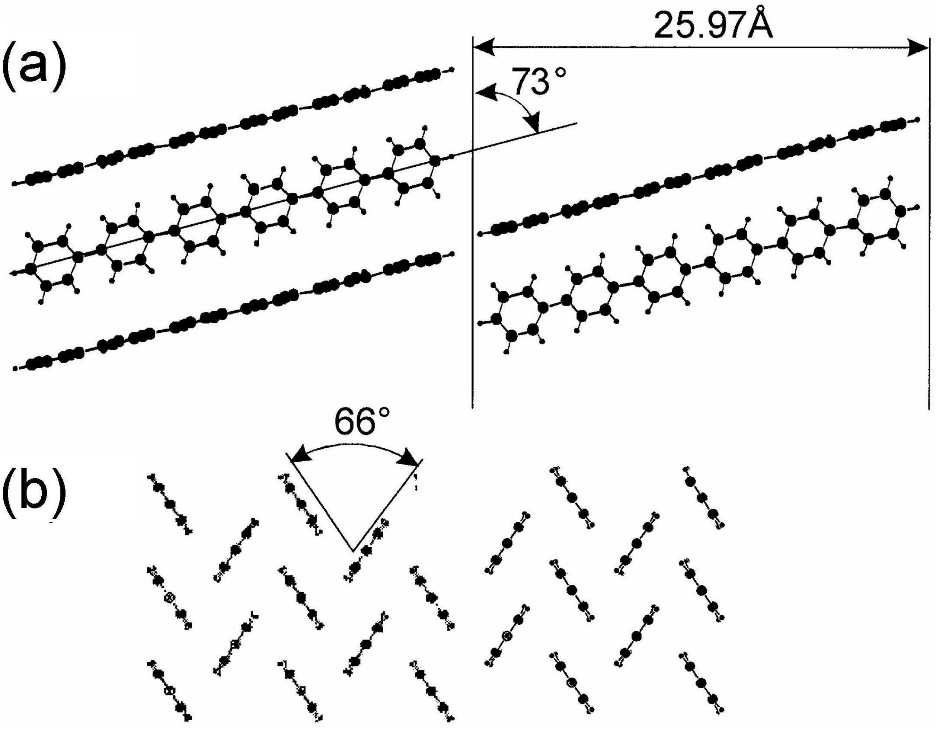

Figure 3.3: Arrangement of hexaphenylene molecules in the β-phase. (a) The hexaphenylene molecule form layers with a thickness of 25.97 Å. (b) The molecular planes of neighboring molecules are tilted by 66° relative to each other. Reproduced from [60]

The reason for this herringbone packing of the molecules is atomic charges on the hydrogen atoms [88]. This results in Coulomb forces which act between the molecules. The fact that the Coulomb forces are stronger than the van der Walls interactions [60] leads to a parallel alignment of the long molecular axes. While the Coulomb forces thus lead to layer formation, the much weaker van der Walls interactions seem to act between the layers [60]. The thickness of a layer is 25.97 Å (figure 3.3a).

In figure 3.4, a space-fill model of the room temperature bulk p6P crystal structure is depicted along with the (100) and (1-1-1) planes, which resemble two close-packed faces of the bulk crystal. Depending on the interaction between the molecules and the surface, the molecules can be either upright standing or lying on the substrate surface. When the interaction between the molecules and the surface is small, the molecules tend to stand upright on the surface, with their close-packed (100) face parallel to the surface [60]. This is for example observed for p6P deposited on alkali halides [89]. The resulting films therefore exhibit step heights of around 2.6 nm, corresponding to the length of the p6P molecule. When the interaction is large, for example due to electrostatic interactions [60], lying molecules with e.g. their (1-1-1) or (20-3) faces parallel to the substrate are observed. This is for example the case for p6P deposited on mica [49] and TiO_2 [8].

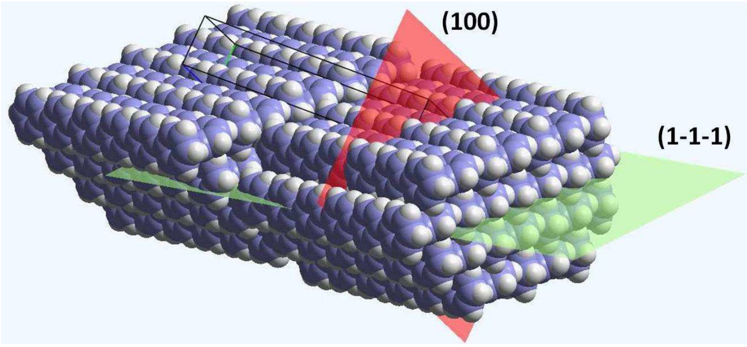

Figure 3.4: The room temperature bulk structure of p6P. Part of the bulk unit cell together with the (100) and (1-1-1) planes are shown. Reproduced from [90].

It should be noted, that for some substrates, both lying and upright standing molecules can be observed, depending on the growth conditions. This is the case for growth on alkali halides, where both substrate temperature [91] and deposition rate [89] influence, whether lying or standing molecules are formed. Therefore, strict control of the parameters during thin film growth is an obvious demand.

A rather simple method for determining, whether lying or upright standing molecules are formed on the surface, is by fluorescence microscopy under normal incidence excitation. The reason is, that the transition dipole moment between the HOMO and the LUMO level in p6P is aligned along the long molecular axes [92] and as a consequence, only molecules lying on the substrate surface can be excited under normal incidence radiation, whereas upright standing molecules do not couple to the normal incidence excitation light [85]. Furthermore, information of the molecules orientation to each other can be found by investigating the polarization properties of the film. A film, which consist of mutually parallel molecules emits polarized fluorescence, since the transition dipoles are all aligned.

3.4 *Para*-hexaphenylene thin film growth

Due to the insolubility of p6P in common solvents, deposition of p6P molecules on substrates is done by vacuum sublimation. Sublimation processes are in general advantageous compared to films prepared from a solution, due to the fact that the molecules are deposited from the gas phase in a high vacuum environment (typically around 10^{-8} mbar), which results in thin films of high purity. Mainly two techniques have been employed for growth of p6P thin films, either organic molecular beam epitaxy (OMBE) [49] or hot wall epitaxy [2]. In this work, p6P nanofibers are grown on different surfaces under various conditions in an OMBE system. The system is described in more details in section 2.1. In short, p6P is deposited via sublimation at around 670 K at a pressure of around 10^{-8} mbar. The nominal thickness of the deposited material and the deposition rate (typically around 0.1 Å/s) are monitored by a water-cooled quartz microbalance. The substrate temperatures range from around 350 K to 450 K.

In this section, growth of different thin films from p6P molecules will be described. This include first some general aspects of the growth process followed by specific examples of thin film growth on muscovite mica, metal-oxide and metal surfaces. The focus in these examples is on the formation of p6P nanofibers on different surfaces.

3.4.1 Thermodynamic aspects of thin film growth

Growth modes

When p6P is deposited on a surface, one of the three following growth modes are generally accepted to take place: Volmer-Weber growth, Frank-Van der Merwe growth or Stranski-Krastanof growth [93]. The three growth modes are illustrated in figure 3.5.

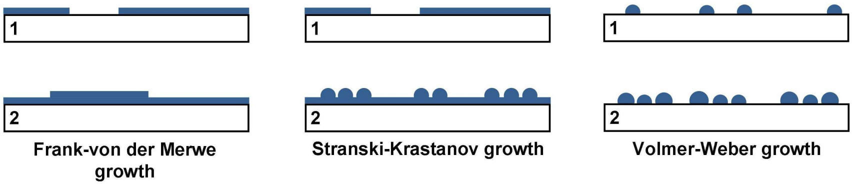

Figure 3.5: Illustration of the three typical thin film growth modes: Frank-Van der Merwe growth, Stranski-Krastanof growth and Volmer-Weber growth.

In Frank-Van der Merwe growth, layers are formed on the substrate, the mode is also denoted as layer-by-layer growth. In Stranski-Krastanof growth, a wetting layer is formed on the surface followed by island growth.

The Volmer-Weber growth is pure island growth. The mode, which is active during thin film growth, depends on the strength of the molecule-molecule interaction compared with the molecule-surface interaction as well as strain in the formed films. In Frank-Van der Merwe growth, the molecule-surface interaction is stronger than the molecule-molecule interaction, and this therefore results in layer-by-layer growth. When the molecule-molecule interaction is stronger, pure island growth is present (Volmer-Weber), whereas Stranski-Krastanof is a mixture between the two. This especially occur when the interface energy is high, thus allowing for initial layer-by-layer growth, and when the strain energy in the film is also high, making subsequent island growth energetically favorable [94].

Nucleation and kinetics

Considering the case where atoms or molecules impinge on a substrate surface, the deposited molecules follow one of the three growth modes depending on the molecule and surface properties. Stable islands or nuclei may form on the substrate surface, which are accompanied by a free-energy change, ΔG, given by [93]:

$$\Delta G = a_3 r^3 \Delta G_V + a_1 r^2 \gamma_{fv} + a_2 r^2 \gamma_{fs} - a_2 r^2 \gamma_{sv} \tag{3.1}$$

Here the interface energies γ are indexed by s (substrate), f (film) and v (vapor), respectively. a is a geometric constant, r is the nucleus radius and ΔG_V is the chemical free-energy change per unit volume. The different parameters are shown in figure 3.6, which is an illustration of the nucleation processes on a surface during vapor deposition.

Thermodynamic equilibrium is achieved when $d\Delta G/dr = 0$, which leads to a critical nucleus size, r^*, and its free energy change, ΔG^*, given by [93]:

$$\frac{r^* = -2(a_1\gamma_{fv} + a_2\gamma_{fs} - a_2\gamma_{sv})}{3a_3\Delta G_V} \tag{3.2}$$

$$\Delta G^* = \frac{-4(a_1\gamma_{fv} + a_2\gamma_{fs} - a_2\gamma_{sv})}{27a_3\Delta G_V^2} \tag{3.3}$$

$$= \frac{16\pi(\gamma_{fv})^3}{3(\Delta G_V)^2}\left\{\frac{2 - 3\cos\Theta + \cos^3\Theta}{4}\right\} \tag{3.4}$$

Here, ΔG^* is given by two factors. The first factor describes homogeneous nucleation, and the second factor describes the wetting, which is 0 for $\Theta = 0°$, i.e. complete wetting, and unity for $\Theta = 180°$. Direct differentiation, assuming an inert substrate and inserting typical values yields [93]:

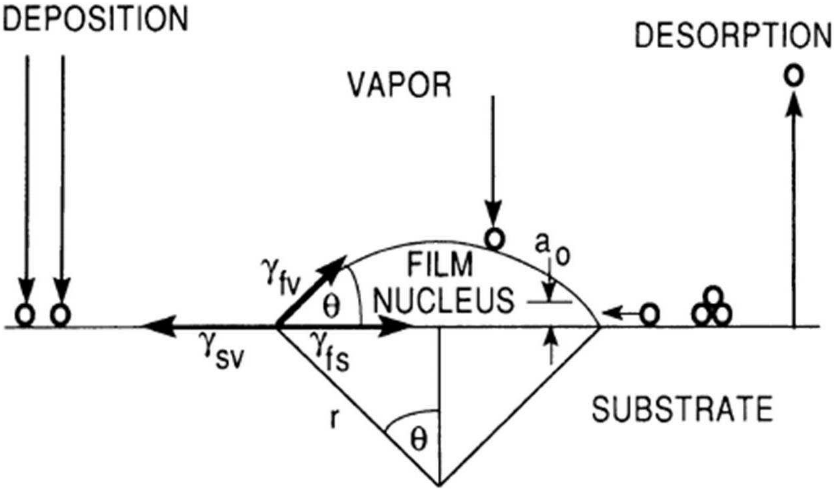

Figure 3.6: Illustration of the nucleation processes on a substrate surface during vapor deposition. Reproduced from [93]

$$\left(\frac{\delta r^*}{\delta T}\right)_R > 0 \quad , \quad \left(\frac{\delta \Delta G^*}{\delta T}\right)_R > 0 \tag{3.5}$$

Hence, an increase in substrate temperature, T, leads to an increase in the critical nucleus size and its free energy change. Furthermore, considering the dependence on the deposition rate, R:

$$\left(\frac{\delta r^*}{\delta R}\right)_T < 0 \quad , \quad \left(\frac{\delta \Delta G^*}{\delta R}\right)_T < 0 \tag{3.6}$$

Hence, the critical nucleus size and its free energy change increase for decreased deposition rates. Therefore, from these basic considerations, the influence of the substrate temperature and deposition rate on the initial nucleation can be deduced. In general, low deposition rates and high substrate temperatures lead to an increase in the nucleus size. This is also seen in the case of p6P deposition on for example muscovite mica (sec. 3.4.2) and Au surfaces (sec. 3.4.4).

Once stable nuclei are formed, they diffuse over the heated substrate surface and may coalesce or agglomerate to form larger aggregates. From thermodynamics, the effective diffusion, D_{eff}, can be described by [95]:

$$D_{eff} = \nu \exp(\frac{-E_{eff}}{K_B T}) \tag{3.7}$$

Where ν is the attempt frequency, E_{eff} is the effective activation energy and T is the substrate temperature [95]. The effective diffusion therefore increases with substrate temperature. This basic expression for the effective diffusion is an important relation for the growth of p6P nanofibers, since the fibers are assembled from diffusing clusters, which therefore, to a large extend, can be controlled by surface temperature. It should be noted, that for real surfaces, parameters like cleavage steps and surface imperfections influence the diffusion of nuclei on the substrate surface. Typically such imperfections hinder diffusion, and thus a significantly higher density of nuclei is usually observed near cleavage steps and other surface imperfections [93].

In this section, some of the basic thermodynamic aspects of thin film growth were discussed, in the following, some specific examples of p6P deposition on different surfaces are demonstrated.

3.4.2 *Para*-hexaphenylene on muscovite mica

Deposition of p6P molecules on muscovite mica leads to formation of mutually parallel nanofibers. The mica is cleaved just before it is introduced to the OMBE system, where p6P is deposited on the heated substrate. As already noted in the previous section, there are several important parameters in such a nanofiber growth process, which influence the end result. Three of the main parameters are the substrate temperature during deposition of the molecules, the deposition rate and the nominal thickness of the p6P layer. These parameters strongly influence both the dimensions and density of the grown nanofibers [1, 96]. One example of this is demonstrated in figure 3.7 which show fluorescence microscopy images of p6P nanofibers grown on muscovite mica at three different substrate temperatures. The nominal thickness of the p6P layer is 5 nm in all cases. It is easily seen that the density of the nanofibers is decreased with an increased substrate temperature.

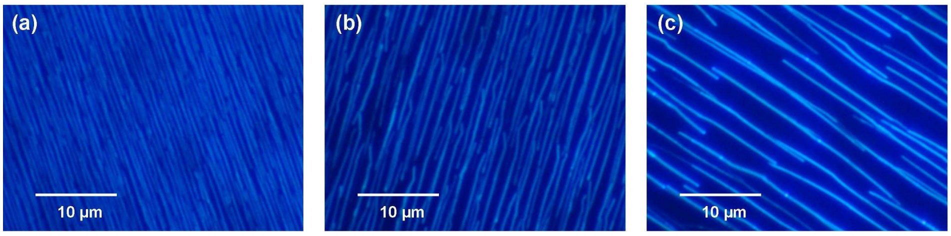

Figure 3.7: Fluorescence microscopy images of blue light emitting p6P nanofibers grown on muscovite mica at a substrate temperature of (a) 390 K, (b) 417 K and (c) 449 K.

In figure 3.8, atomic force microscopy images of the same samples are shown. As seen from images, the nanofiber dimensions increase with an increasing substrate temperature. This is mainly the mean length of the fibers, which increase from around 6 μm at 390 K to around 25 μm 449 K. The width of the nanofibers also increases from around 200 nm at 390 K to around 300 nm at 449 K. These observations are quantitatively the same as those previously observed for p6P nanofibers on muscovite mica [96].

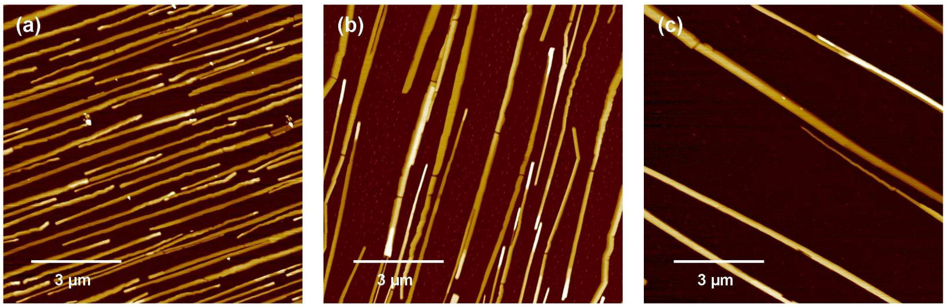

Figure 3.8: AFM images of p6P nanofibers grown on muscovite mica at a substrate temperature of (a) 390 K, (b) 417 K and (c) 449 K. The height range is (a) 100 nm, (b) 70 nm and (c) 116 nm, respectively.

Growth of p6P nanofibers on muscovite mica follows the Stranski-Krastanof growth mode. A detailed illustration of this is demonstrated in figure 3.9. There are different stages present in such a growth process. First a wetting layer is formed on the surface, second clusters are formed until a critical size and number density are reached, and then finally fibers are assembled from these clusters [96, 97], whose diffusion can be described from equation 3.7, i.e. the effective diffusion is increased with temperature. The clusters are crystalline [97] and their size depend on temperature: the cluster size increases for increasing substrate temperatures [96], which is consistent with basic nucleation theory (see eq. 3.5). The large increase in length compared to height and width can be assigned to anisotropic molecular interactions, i.e. the molecules tend to pack with the molecular axes parallel to each other.

Investigations of the microscopic growth process of p6P nanofibers on muscovite mica by LEED measurements have revealed, that the nanofibers grow with either the (1-1-1) or the (2-1-1) face of the bulk crystal (β-structure) parallel to the substrate, i.e. the nanofibers are assembled from molecules lying on the substrate surface [1]. This is also indicated by the fluorescence microscopy images (fig. 3.7), since only lying molecules can be excited under normal incidence irradiation.

The reason for the growth of mutually parallel nanofibers on muscovite mica is a combination of epitaxy and electric-field induced alignment of the molecules. The nanofibers grow along one of the two possible high symmetry directions on mica, i.e. along one of the $\langle 110 \rangle$ directions determined

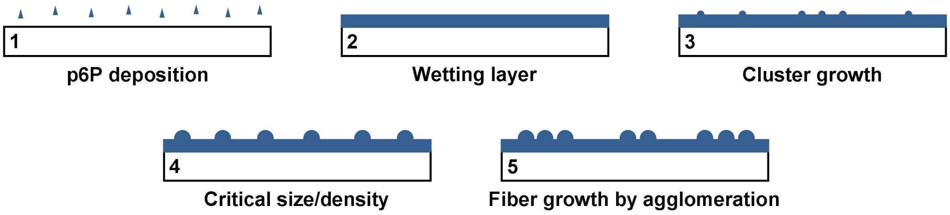

Figure 3.9: Illustration of the Stransky-Krastanov growth mode. Cluster growth is present on top of a wetting layer until a critical cluster size and density is reached from where nanofiber growth starts.

from Schlagfigur investigations [90]. The long molecular axes are almost perpendicular to the long fiber axis and are parallel to electric fields present on the mica surface upon cleavage [98]. The orientation of the molecules to the electric fields is likely due to a dipole-induced dipole interaction, since the average dipole moment of p6P is zero [90]. In figure 3.10, the growth of p6P nanofibers on mica is illustrated. In fig. 3.10a, the (1-1-1) face of the bulk p6P crystal is depicted along with the surface unit cell. The long nanofiber direction is marked by a blue arrow. In fig. 3.10b, the unit cell is reproduced together with the (001) face of mica. The nanofiber growth direction is along the $\langle 110 \rangle$ direction of mica. The electric fields present on the surface are marked with arrows.

3.4.3 *Para*-hexaphenylene on metal-oxide surfaces

In recent studies it has been demonstrated that highly ordered p6P films can be grown on single-crystalline metal-oxide surfaces [8, 99, 100, 101]. The p6P films display single crystallinity and in certain cases also nanofiber growth. In contrast to mica, where oriented growth of nanofibers is due to a combination of epitaxy and electric field induced alignment, pure epitaxial grown, mutually parallel nanofibers are observed on TiO_2(110) [8] and on (2x1) oxygen reconstructed Cu(110) [100].

On TiO_2(110) mutually parallel, segmented nanofibers are observed. The nanofiber growth direction is along the [1-10] direction of the highly anisotropic TiO_2(110) and X-ray diffraction (XRD) data reveals, that the molecules are oriented perpendicular to the long fiber axis, namely along the [001] direction [8]. Therefore it is believed that molecular alignment along the atomic rows on the single-crystalline TiO_2(110) surface is the reason for the oriented growth [8]. The nanofiber growth on TiO_2(110) is different from the fiber growth on muscovite mica, where nanofibers are assembled from crystalline clusters (section 3.4.2). Instead nanofibers on TiO_2(110) are assembled from individual, aligned molecules, which are all mutually parallel over the entire surface and hence display only a single crystalline

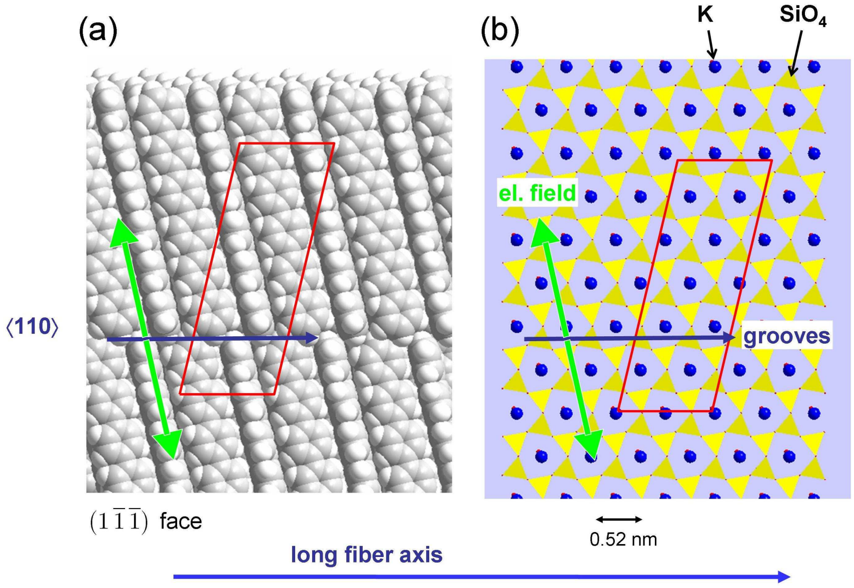

Figure 3.10: (a) The (1-1-1) face of the bulk p6P crystal structure together with the surface unit cell. (b) The (001) face of mica together with the unit cell. The short axis of the unit cell is parallel to mica ⟨110⟩. The direction of the molecules is parallel to the electric fields, which are symbolized by arrows. Reproduced from [90].

orientation. As mentioned before, the nanofibers are segmented, and are therefore limited in length to around 1 μm [8].

Similar growth has been observed on Cu(110)(2x1)O surfaces, where mutually parallel nanofibers are grown from molecules which align parallel to the O rows, i.e. perpendicular to the long fiber axis [100]. Both on Cu(110)(2x1)O and $TiO_2(110)$ surfaces, lying molecules with their close-packed (20-3) face parallel to the substrate are formed [8, 99, 100, 101].

Although a high degree of order is achievable on these surfaces, the difficulty in preparing the clean[1], ordered substrates makes them less interesting from an applied point of view.

3.4.4 *Para*-hexaphenylene on metal surfaces

Due to its large application potential, metal surfaces are of special interest as substrates for nanofiber growth. This is for example the possibility to act as contact electrodes in new types of organic field effect transistors (OFET's) or organic light emitting diodes (OLED's). In the past it has been

---

[1] Typically the cleaning process involves sputtering with Argon ions in vacuum and subsequent annealing in ultra high vacuum.

demonstrated, that nanofibers from p6P molecules can be grown on Au surfaces, for example on Au coated mica [6] and on Au(111) surfaces [7]. In this work, deposition of p6P is investigated on various metals as substrates for nanofiber growth.

In contrast to previous studies, the metal substrates here are prepared by electron beam deposition (10^{-5} mbar, 0.6 Å/s) of around 50 nm metal on either silicon(100) or glass (pyrex) substrates. After metal deposition, the substrates are immediately transferred into the OMBE system (section 2.1) for deposition of the organic molecules.

Deposition of p6P on such simple prepared metal surfaces still leads to nanofiber formation in specific cases. This is demonstrated in figure 3.11, which shows fluorescence microscopy images of p6P deposited on an electron beam evaporated Au surface (fig. 3.11a). For comparison, nanofibers grown on muscovite mica at the same conditions are shown as well (fig. 3.11b).

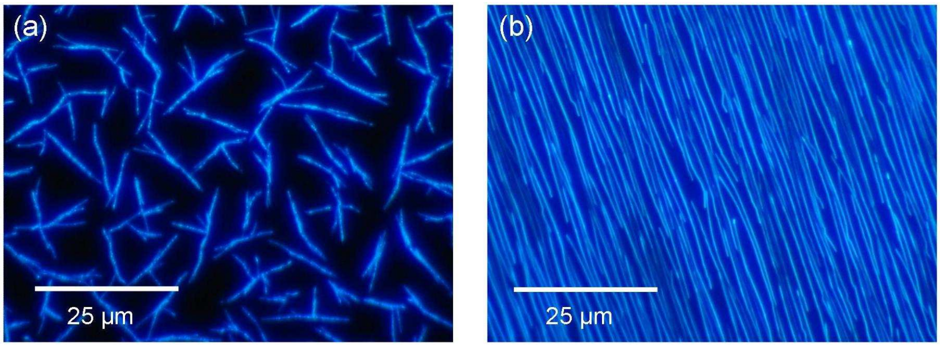

Figure 3.11: p6P nanofibers grown on (a) 55 nm Au, deposited on pyrex glass, and on (b) muscovite mica. The nominal thickness of the p6P layer is 5 nm, the nanofibers are in both cases grown at a substrate temperature of 432 K.

It is clearly possible to grow nanofibers on such Au surfaces, however, in contrast to nanofibers on mica, no preferred orientation of the nanofibers is observed. In the following, deposition of p6P on various metal substrates will be described. P6P deposition on Au surfaces will be described first followed by p6P deposition on various other metal surfaces.

Para-hexaphenylene on Au surfaces

In previous studies, p6P deposition on crystalline Au(111) surfaces has been described [7, 102, 103]. On Au(111) surfaces, p6P deposition leads to one of three different film types depending on the substrate temperature. At low temperatures (93 K), an almost continuous flat film is formed on the surface, whereas a more island-like film is formed at room temperature [7]. In the latter case, a wetting layer is first formed on the surface, and the growth mode can be described by a Stranski-Krastanof mode. At high temperatures (430 K) nanofibers, which consist of lying molecules, are formed along with terraces made of upright standing molecules [7, 103]. The nanofiber growth direction is along three directions separated by an angle of 120°, which is a clear indication of an epitaxial relationship between the nanofiber growth and the Au(111) surface geometry [7]. This has also been observed for p6P deposited on Au coated muscovite mica [6].

As already demonstrated, p6P deposition on electron beam evaporated Au surfaces also leads to nanofiber formation (fig. 3.11a). The nanofiber formation exhibits a clear temperature dependence, as it is shown in figure 3.12. The figure shows fluorescence microscopy images of 5 nm p6P deposited on Au at a substrate temperature of 388 K (fig. 3.12a), 416 K (fig. 3.12b) and 449 K (fig.3.12c). The Au surfaces were prepared by evaporating 55 nm Au onto silicon(100) substrates. The substrates were transferred to the OMBE system immediately after Au evaporation.

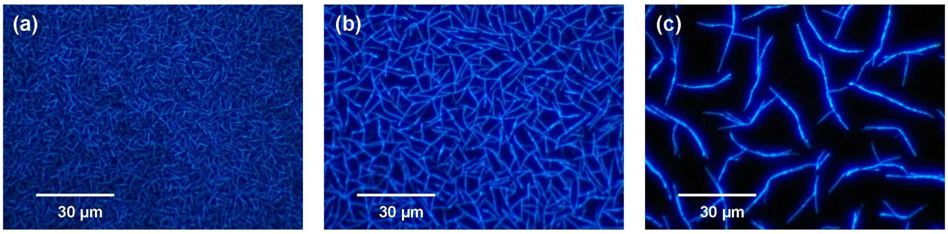

Figure 3.12: Fluorescence microscopy images of p6P nanofibers grown on Au coated Si at a substrate temperature of (a) 388 K, (b) 416 K, (c) 449 K.

It is seen, that the nanofiber density decreases with an increased substrate temperature. Furthermore, the nanofiber length increases with temperature. These observations are similar to those seen for p6P nanofiber growth on muscovite mica (fig. 3.7 and fig. 3.8). No preferred growth orientations of the nanofibers are observed on these substrates, i.e. there seem to be no epitaxial relationship between the organic molecules and the Au surface, indicating that the Au surface is non-crystalline. It should be noted that no cleaning of the substrates was performed after the substrates were introduced to the OMBE system, i.e. the Au surface cannot be expected to be completely clean.

For both p6P and p4P deposition on Au(111) surfaces, the influence from an initial carbon layer on the Au surface has been studied. In the case of p6P [102], the first p6P layer changes from highly regular and well-defined on clean Au (111) to disordered on carbon covered Au(111)

For p4P films, a change of both morphology and orientation of grown nanofibers has been demonstrated as a consequence of carbon coverage on

Au(111) surfaces [104, 105]. On clean Au(111) surfaces, p4P nanofibers with preferred orientations are observed due to an epitaxial relationship between the lying molecules and the surface [104, 105, 106, 107]. Again the growth mode can be described by a Stranski-Krastanof growth mode. When covered with carbon, this epitaxial relationship is weakened, resulting in a less oriented fiber growth. Furthermore, the grown fibers are no longer straight, but start to bend due to the carbon coverage on the Au surface [105]. A further carbon covered Au(111) surface leads to a film of upright standing molecules without any nanofiber growth [104, 105].

Therefore, not only the crystal structure of the surface, but also the surface composition affects the formation of nanofibers on Au surfaces. A clean, crystalline surface is needed for achieving oriented p6P nanofibers on non-structured Au surfaces.

Figure 3.13 show AFM images of p6P nanofibers grown on evaporated Au surfaces at substrate temperatures of 388 K (fig. 3.13a), 416 K (fig. 3.13b) and 449 K (fig. 3.13c), respectively. As fluorescence microscopy revealed (fig. 3.12), the nanofiber density decreases with an increasing substrate temperature. The AFM measurements show, that small clusters are present in between the nanofibers, and that the size of these clusters depends on the substrate temperature during growth. The cluster width increases from around 50 nm at 388 K to 200 nm at 449 K, whereas their height increases from around 20 nm at 388 K to 40 nm at 449 K. This growth behavior is similar to that of p6P nanofibers grown on muscovite mica (section 3.4.2), where the nanofibers are assembled from crystalline, diffusing clusters, whose sizes are also temperature dependent. This is also qualitatively expected from basic nucleation theory (sec. 3.4.1).

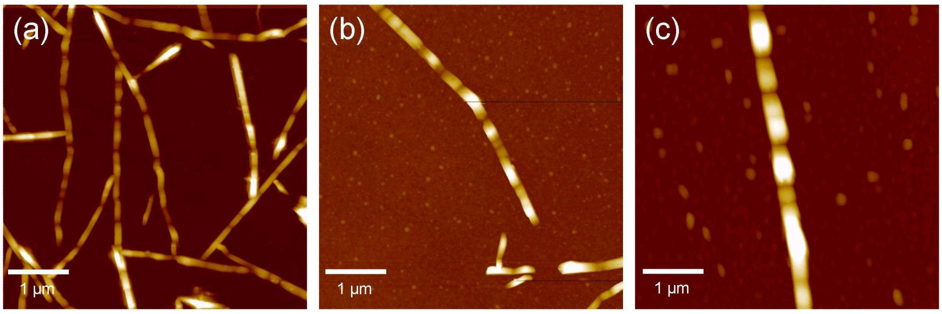

Figure 3.13: AFM images of p6P nanofibers grown on Au coated Si at a substrate temperature of (a) 388 K, (b) 416 K, (c) 449 K. The height range is (a) 299 nm, (b) 230 nm and (c) 206 nm, respectively.

As already seen from fluorescence microscopy measurements, the length of the nanofibers increases with temperature (fig. 3.12). The AFM measurements reveal an increase in nanofiber width with substrate temperature as well. The width increases from around 150 nm at 388 K to around 400 nm at 449 K. Furthermore, the AFM measurements show, that the nanofibers are not flat as in the case of p6P nanofibers grown on mica. Instead, the nanofibers show a faceted structure. This has also been observed for nanofibers grown on Au coated mica [6]. A more detailed image of the nanofiber morphology is shown in figure 3.14, which shows a 3D representation of a single nanofiber grown on Au at a substrate temperature of 449 K. The facets along the nanofiber are easily seen together with the small clusters from which the fibers are assembled.

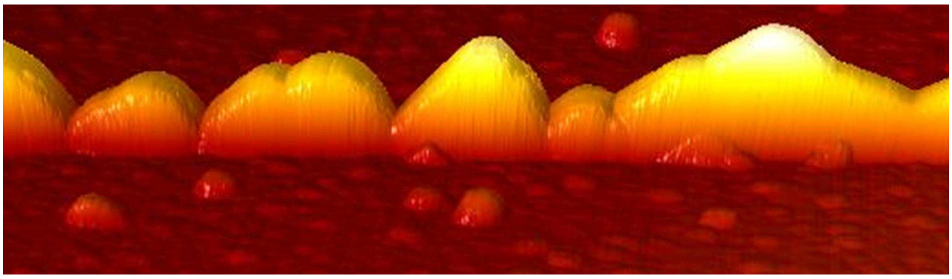

Figure 3.14: 3D AFM image of a p6P nanofiber grown on Au coated Si at a substrate temperature 449 K. The width of the image is 4 μm. The height range is 206 nm.

***Para*-hexaphenylene on Ti, Cr, Al and Ag**

In addition to Au, p6P deposition on Al, Ag, Ti and Cr has been investigated. The metals are deposited onto glass (pyrex) substrates by electron beam deposition, afterwards 5 nm p6P is deposited on the metal surfaces at a substrate temperature of 432 K. Figure 3.15 shows fluorescence microscopy images of the films grown on (a) Al, (b) Ag, (c) Ti and (d) Cr, respectively. As it is seen, the films do not show any nanofiber formation as in the case of p6P deposition on Au, instead only small clusters of different kinds are seen on the surfaces. For Al (fig. 3.15a), elongated p6P clusters are formed on the surface, whereas for both for Ag and Cr, smaller and more circular shaped clusters seem to appear. The fact that the p6P clusters on Ag fluoresce much more than on Cr, indicates, that different molecular orientations are present on the two surfaces, i.e. lying molecules are formed on the Ag surface, whereas upright standing molecules are formed on the Cr surface[2].

A more detailed analysis of the grown films is made by AFM measurements. Figure 3.16 shows AFM images of the same samples, i.e. 5 nm

---

[2] It should be noted, that a difference in sticking coefficients and optical reflectivity, may influence on the comparison of the fluorescence microscopy measurements on the different metals.

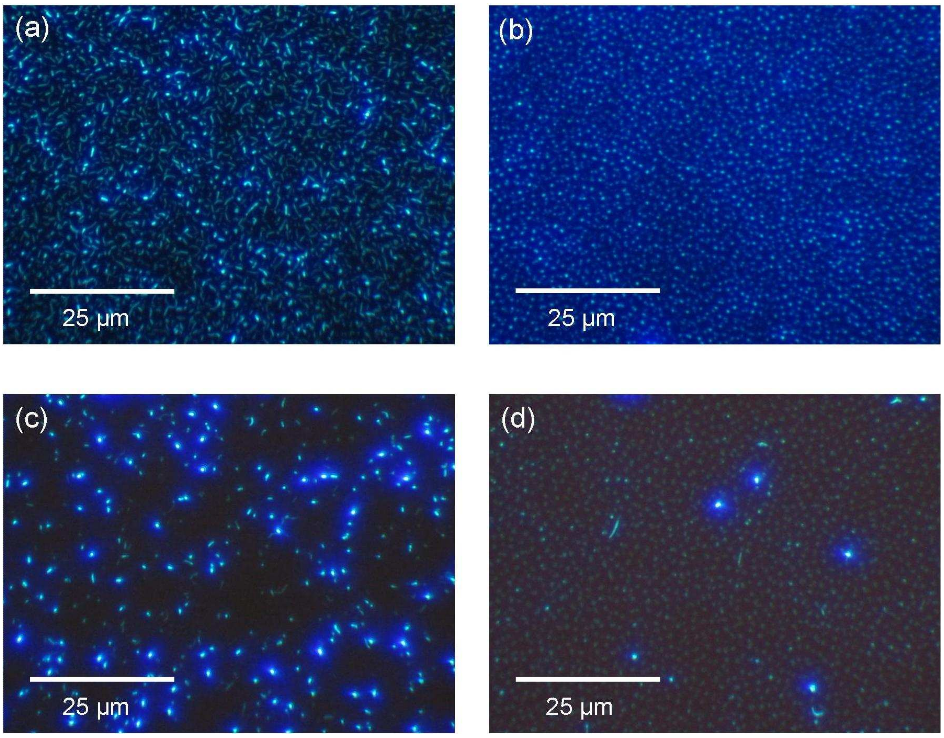

Figure 3.15: Fluorescence microscopy images of p6P nanofibers grown on 55 nm (a) Al, (b) Ag, (c) Ti and (d) Cr, deposited on a pyrex glass. The nanofibers are grown at a substrate temperature of 432 K.

p6P deposited on (a) Al, (b) Ag, (c) Ti and (d) Cr, respectively. For Ag (fig. 3.16b) and Cr (fig. 3.16d), clusters with typical widths around 600 nm and typical heights around 60 nm appear, although with some variations in both dimensions across the sample. For Ti (fig. 3.16c), flat islands of different shapes are formed. The typical height of these islands is around 20 nm. Furthermore, small clusters with typical height around 200 nm are formed as well. From comparing the fluorescence microscopy analysis with the AFM analysis, it is assumed, that the flat islands are assembled from upright standing molecules, whereas the small clusters are assembled from lying molecules, since they fluoresce when excited by normal incidence UV light (fig. 3.15c). On Al, the growth can be characterized as elongated clusters, both seen in fluorescence microscopy and the AFM images. However, high resolution imaging by AFM was not possible when scanning this particular surface. It could not be determined, whether lying or upright standing p6P molecules are formed on the Al surface.

It should be noted, that at higher temperatures, short nanofibers start to form on Ag surfaces. This is not the case for the other metals. Figure 3.17

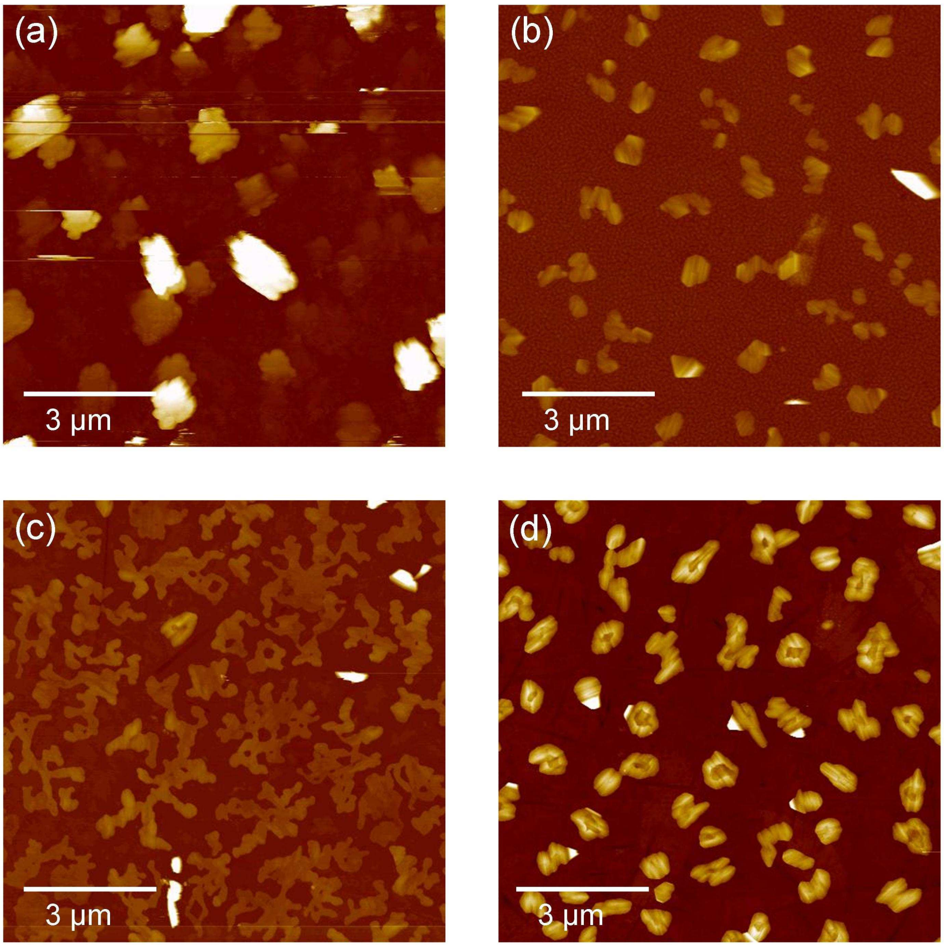

Figure 3.16: AFM images of 5 nm p6P deposited on (a) Al, (b) Ag, (c) Ti and (d) Cr at a substrate temperature of 432 K. The metals were deposited on a pyrex substrate by electron beam evaporation. The height range is (a) 571 nm, (b) 426 nm, (c) 260 nm and (d) 205 nm, respectively.

shows fluorescence microscopy images of 5 nm p6P deposited on silver coated (50 nm) silicon at 439 K. It is seen that small fibers start to form at this temperature, however, these nanofibers are much shorter than nanofibers grown on gold at the same temperature. The nanofibers also grow randomly in all directions, as it the case for nanofiber growth on gold.

The reason why these substrates do not lead to nanofiber formation is not clear, however, the relatively high density of clusters/islands on the surface suggest, that the molecules are less mobile on these surfaces compared to molecules on Au surfaces, where long, separated nanofibers are formed at the same substrate temperature (fig. 3.11a). As demonstrated for p6P on

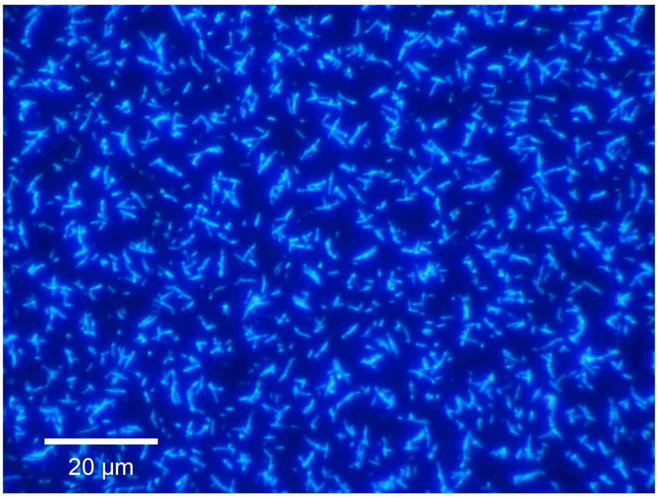

Figure 3.17: Fluorescence microscopy image of 5 nm p6P deposited on Ag coated (50 nm) silicon at 439 K.

muscovite mica, the morphology of the nanostructures depends strongly on the surface energy [90]. On mica, bend fibers and upright standing molecules are observed at a reduced surface energy [90], compared to long, mutually parallel nanofibers on freshly cleaved muscovite mica. The surface energies of the different metals are listed in table 3.1 [108, 109].

Metal	Surface enegergy
Aluminum (Al)	1.143 J/m^2
Silver (Ag)	1.246 J/m^2
Titanium (Ti)	1.989 J/m^2
Chromium (Cr)	2.354 J/m^2
Gold (Au)	1.506 J/m^2

Table 3.1: Surface energy of Al, Ag, Ti, Cr and Au [108, 109].

Both for Titanium and Chromium, the surface energy is higher than for gold. However, Titanium, Chromium and Aluminum are all known to form a thin oxide layer, which reduces the surface energy [93] (the samples are transferred in air after metal deposition). This can be one explanation for the different nanostructure formation on the metals, however, further investigations are needed to verify this assumption. This could for example include growth on metal films which are prepared in the vacuum system.

The fact, that the organic films are formed from molecules or clusters, which diffuse over the heated metal surfaces, makes the quality and roughness of the metal surface important. The surface roughness of the five different metal films evaporated on pyrex glass (including Au, fig. 3.11a) has been measured by AFM, using the sofware: The Scanning Probe Image Processor (SPIP) version 3.3.6.0 from Image Metrology[3]. The measured RMS film roughness of the different metal films are listed in table 3.2. Although some variations of the roughness are seen, they are in all cases within one to a few nanometers, and it is not expected, that smoother films would affect the nanostructure growth on the different metals a lot.

Metal (55 nm on pyrex glass)	RMS roughness
Aluminum (Al)	2.49 nm
Silver (Ag)	3.75 nm
Titanium (Ti)	1.06 nm
Cromium (Cr)	1.23 nm
Gold (Au)	1.31 nm

Table 3.2: RMS roughness of different metal films (55 nm) prepared by electron beam evaporation on pyrex glass. The roughness has been measured at a scan area of 3 μm^2 in all cases.

3.5 Summary

In this chapter, nanofiber growth from *para*-hexaphenylene (p6P) molecules on non-structured surfaces has been described. This includes the molecular and crystal structure of p6P along with some basic properties. The assembly of the molecules into nanostructures on various surfaces has been discussed. In general it can be concluded, that oriented nanofiber growth is possible on muscovite mica, $TiO_2(110)$, Cu(110)(2x1)O and Au(111) surfaces, however, only on muscovite mica, long, mutually parallel nanofibers are formed. Common for these substrates is, that they are crystalline, i.e. the directed growth is epitaxial driven through the interaction between the molecules and the substrate surface. On non-crystalline surfaces, nanofiber growth has been demonstrated on Au surfaces, however, the growth is not directed due to the non-crystallinity of the surface. P6P deposition on other metal surfaces (Al, Ag, Ti, Cr) has been investigated as well, however, no nanofiber growth was possible on these, with exception of Ag surfaces, where short nanofibers were observed at high surface temperatures.

---

[3] www.imagemet.com

Chapter 4

Nanofibers on structured templates

In chapter 3, growth of p6P nanofibers on different planar surfaces was discussed. As it was shown, nanofibers can be grown on different substrates, however, long, mutually parallel nanofibers can solely be grown on a specific crystalline growth template, namely muscovite mica. In many applications, however, parallel nanofibers on specific micrometer sized regions (for example on ridges or in channels) are needed, which requires pre- or post-processing of the substrates [20, 22, 28]. Therefore, for device purposes, mica is unsuitable. One way to overcome this problem, is by transferring the nanofibers from mica to a device substrate, while retaining there parallelism. Previous studies have shown, that p6P nanofibers can be transferred from muscovite mica, as an ensemble or individually, to other substrates [5], which for example has allowed for investigations of the electrical [110] and mechanical [52] properties of the fibers. However, large-scale, controlled transferring of the nanofibers onto specific, micrometer sized device areas is a very difficult task. Furthermore, destruction or contamination of the nanofibers during transferring also restrains the usefulness of this method.

In this chapter, a new approach, which relies on growth on nano- and micro-structured surfaces, is presented. The aim of this method is to achieve *in-situ* growth of mutually parallel p6P nanofibers on prefabricated device platforms, i.e, to grow the nanofibers in a controlled way, where they are needed. An obvious choice of device substrate is silicon, due to its excellent compatibility with micro-processing techniques, which have been exploited for decades in microelectronics. However, as previous studies have shown [111], and as demonstrated in figure 4.1, p6P deposition on silicon does not lead to nanofiber growth. The figure shows SEM images of 2 nm p6P deposited on silicon at a substrate temperature of 435 K. The silicon substrate is partly coated with Au. The Au was deposited through a mask, therefore only the lower (bright) part on figure 4.1a is coated with Au, whereas the upper (dark) part is uncoated, i.e. p6P on bare silicon.

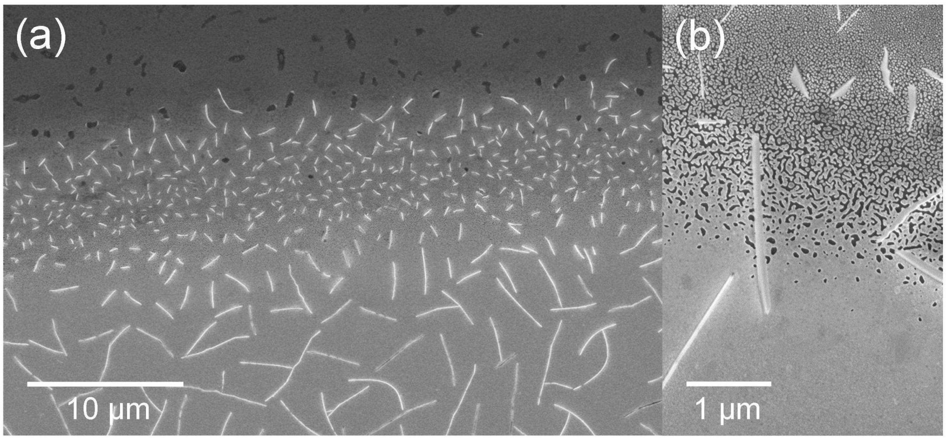

Figure 4.1: SEM images of 2 nm p6P deposited on Au coated silicon(100) at a substrate temperature of 435 K. (a) The Au has been deposited through a mask, so only the lower (bright) part of the substrate is coated with Au, whereas the upper (dark) part is pure Si. On (b) a zoom-in on the boundary region between Au and Si is shown.

As it is seen, the Au coated part shows random nanofiber growth (as it was demonstrated in section 3.4.4), whereas the bare silicon part only shows a few p6P islands. So although silicon itself does not allow for nanofiber growth, a thin Au layer circumvents this problem. Metal deposition is a standard process within micro-fabrication, and therefore this does not preclude its usage from a device oriented point of view.

In figure 4.1b, a zoom-in on the boundary region is shown. The Au film is changed in this region from continuous to cluster-like, which clearly modifies the nanofiber growth from long, separated fibers on the continuous film, to shorter and more closely packed nanofibers in the boundary region. This can be explained by a limited diffusion of p6P molecules or clusters in this region, which increase the nucleation sites. This demonstrates, that it is possible to modify the diffusion and thereby nanofiber growth by structuring the Au surface prior to p6P deposition.

The basic idea demonstrated in this chapter, is growth of p6P nanofibers on periodically structured Au surfaces, as a method for achieving oriented growth of nanofibers on device compatible substrates. Au has the advantage, that it can be deposited on various substrates and still allow for nanofiber growth (sec. 3.4.4). Therefore it is possible to use different types of nano- or micro-structured substrates as the base template, and then deposited Au to achieve the structured Au surface. In this work, two different substrates have been used, namely silicon and alumina templates. Silicon can be structured in a controlled way on a micrometer scale by optical lithography and etching, and is therefore ideal for growth on microstructured templates. Alumina templates with a high pore regularity can rather easily be fabricated [112]. This is therefore a cheap and fast method for fabricating nanostructured templates compared to for example electron beam lithography, although it does not allow for the same design flexibility.

4.1 Au coated microstructured silicon

4.1.1 Au coated micro-ridges

In this section, growth of nanofibers on microstructured Au surfaces is demonstrated. The microstructures are fabricated in silicon(100) by optical lithography and reactive ion etching. An Au layer is deposited on the structured substrate by electron beam deposition to achieve the microstructured Au surface. Experimental details regarding the optical lithography and reactive ion etching are described in section 2.3 and section 2.4, respectively. In short, the optical lithography is performed by using a Karl Süss MA 150 mask aligner, the subsequent reactive ion etching (RIE) is done in a deep plasma etching system type AMS 110 from Alcatel, using the BOSCH process with a mixture of $SF_6/C_4F_8/O_2$. One microstructured configuration, which has been investigated, is periodically ordered micro-ridges fabricated with different dimensions. In figure 4.2 an interference microscopy image of 10 μm wide micro-ridges fabricated in Silicon is shown.

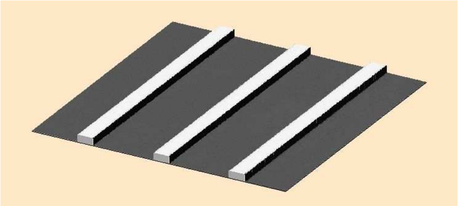

Figure 4.2: 200 μm x 200 μm interference microscopy image of 10 μm wide micro-ridges fabricated in Silicon by optical lithography. The height of the structures is 3 μm.

After etching and resist removal, the wafers are cleaned in an oxygen plasma, before 55 nm Au is deposited on the substrates. The Au deposition is done at a rate of 0.6 $\text{Å}s^{-1}$ in a BOC Edwards 500 system, with a deposition pressure of around 10^{-5} mbar. The Au coated substrates are immediately transferred into the OMBE system (section 2.1), where the p6P deposition is performed.

In figure 4.3, a fluorescence microscopy (fig. 4.3a) and a SEM (fig. 4.3b) image of p6P nanofibers, grown on such a Au coated micro-ridge at a substrate temperature of 388 K, is shown. The width of the ridge is 5 μm and the nominal p6P thickness is 5 nm.

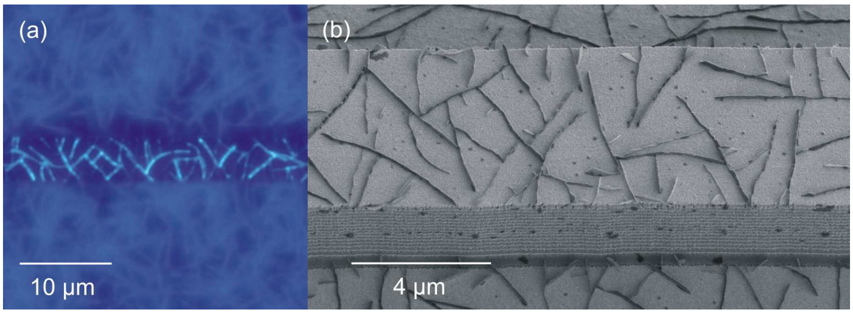

Figure 4.3: (a) Fluorescence microscopy image and (b) tilted scanning electron microscopy image of p6P nanofibers grown on a 5 μm wide Au coated ridge at a substrate temperature of 388 K.

As it is seen from the images, nanofibers grow, as expected, both on top of the ridge and at the bottom of the substrate, since the whole substrate is coated with Au. In the fluorescence microscopy image (fig. 4.3a), the nanofibers, which are grown at the bottom of the substrate, appear blurred, since they are out of focus. The nanofibers grown on top of the ridge (and at the bottom of the substrate) grow in all directions, as it is the case for nanofibers grown on planar Au surfaces (fig. 3.12), i.e. their orientation is not affected by the micron-size ridge. This is not surprising considering the dimensions of the nanofibers and the ridge, since the nanofibers are shorter than the ridge width.

Figure 4.4, shows a fluorescence microscopy (fig. 4.4a) and a SEM (fig. 4.4b) image of p6P nanofibers grown on a 5 μm wide Au coated ridge at a substrate temperature of 435 K. Again the nominal p6P thickness is 5 nm.

At this substrate temperature, the nanofibers are much longer, and the orientation of the nanofibers is clearly affected by the micro-ridge. The nanofibers, which are grown on top of the ridge, grow almost perpendicular to the long ridge axis, whereas those grown at the bottom of the substrate still grow randomly in all directions (fig. 4.4a). This demonstrates, that it is possible to grow mutually parallel p6P nanofibers on microstructured Au surfaces, if the substrate temperature is high enough. This effect has been analyzed in more details by investigating the substrate temperature dependence on the orientational distribution of the nanofibers grown on top of both 2.5 μm (fig. 4.5) , 5 μm (fig. 4.6) and 10 μm (fig. 4.7) wide Au coated ridges.

The orientational distributions show a strong temperature dependence for growth on both 2.5, 5 and 10 μm wide Au coated ridges. The growth is almost random at 388 K, however, at a small ridge width (fig. 4.5 and

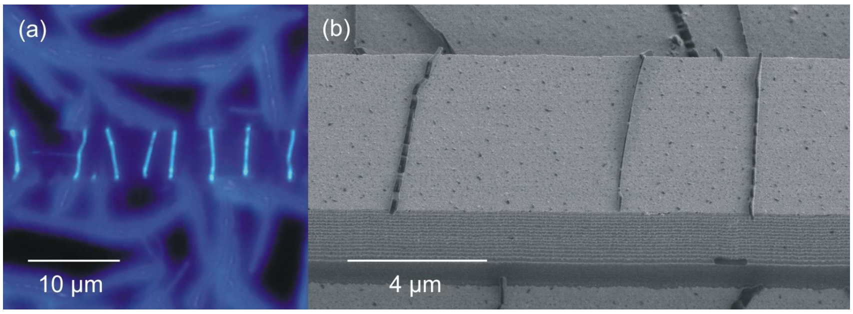

Figure 4.4: (a) Fluorescence microscopy image and (b) scanning electron microscopy image of p6P nanofibers grown on a 5 μm wide Au coated ridge at a substrate temperature of 435 K.

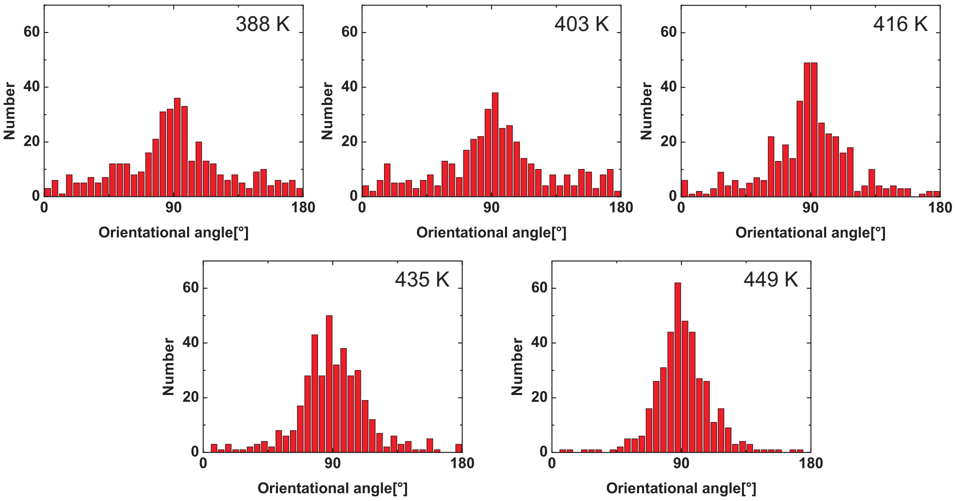

Figure 4.5: Orientational distribution of p6P nanofibers grown on 2.5 μm wide Au coated ridges at a substrate temperature of 388 K, 403 K, 416 K, 435 K and 449 K, respectively. The growth orientation is with respect to the long ridge axis.

fig. 4.6), oriented growth start to occur even at this temperature. At high substrate temperatures, the nanofiber growth is almost perpendicular to the long ridge axis. It should be noted, that the mean value is not the same in all distributions, however, it is always close to 90°. The distributions reveal, that growth orientation is not only temperature dependent, but depend on the ridge width as well. This is demonstrated in figure 4.8, which shows a plot of the standard deviation of the orientational distributions as a function of the ridge width for nanofibers grown at a substrate temperature of 388

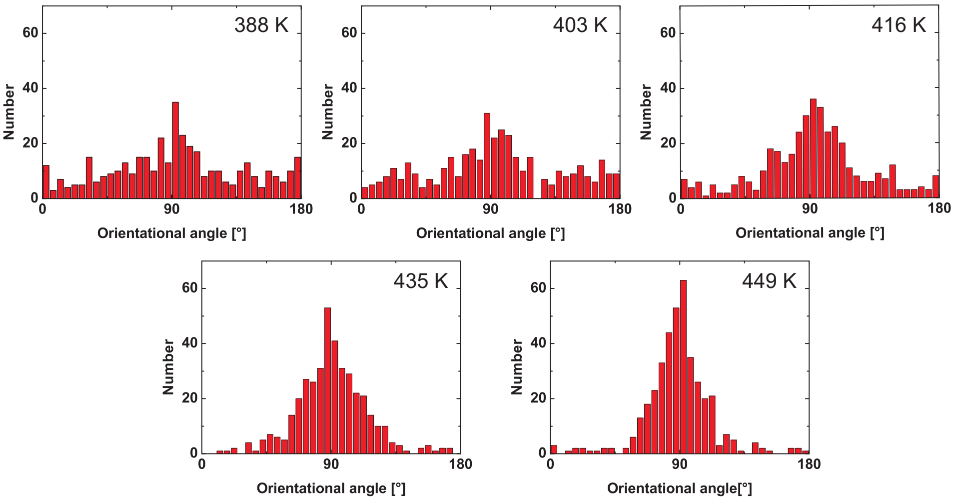

Figure 4.6: Orientational distribution of p6P nanofibers grown on 5 μm wide Au coated ridges at a substrate temperature of 388 K, 403 K, 416 K, 435 K and 449 K, respectively. The growth orientation is with respect to the long ridge axis.

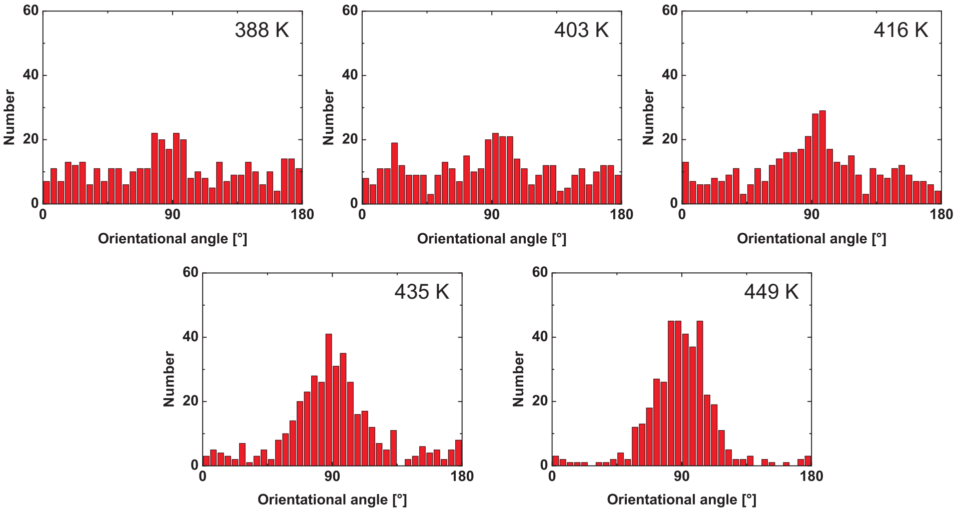

Figure 4.7: Orientational distribution of p6P nanofibers grown on 10 μm wide Au coated ridges at a substrate temperature of 388 K, 403 K, 416 K, 435 K and 449 K, respectively. The growth orientation is with respect to the long ridge axis.

K, 403 K, 416 K, 435 K and 449 K, respectively. Clearly the standard deviation is smaller at higher substrate temperatures, i.e. the nanofibers are better oriented at high temperatures. Furthermore, the standard deviation increases with ridge width, i.e. nanofibers are better oriented at narrow ridges.

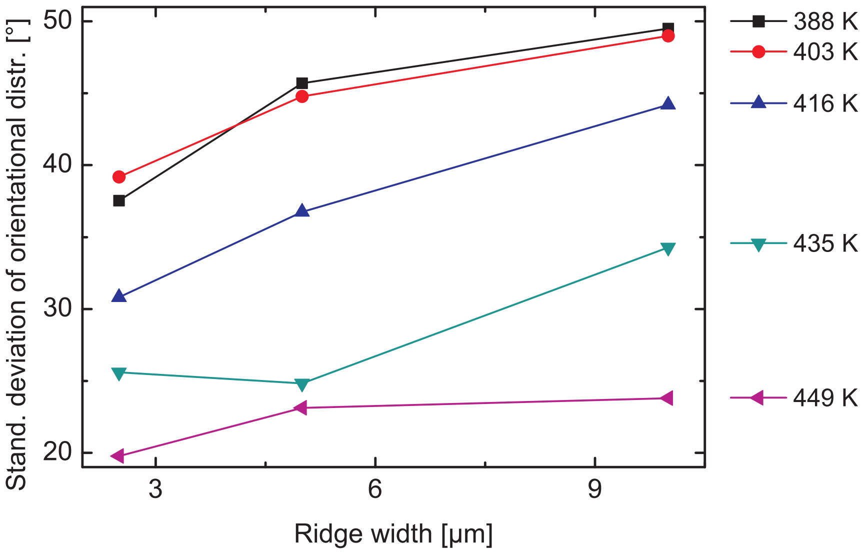

Figure 4.8: Standard deviation of the orientational distributions as a function of the ridge width for nanofibers grown at a substrate temperature of 388 K, 403 K, 416 K, 435 K and 449 K, respectively.

Length distributions of the nanofibers grown on 2.5 μm (fig. 4.9), 5 μm (fig. 4.10) and 10 μm (fig. 4.11) wide Au coated ridges at the different substrate temperatures have also been measured. The distributions show, that the nanofiber length increases with temperature as on planar Au surfaces (sec. 3.4.4). Furthermore it is seen, that on 2.5 μm (fig. 4.9) and 5 μm (fig. 4.10) wide ridges, the nanofiber length is at high substrate temperatures limited to the size of the ridge. This is especially clear when looking at the nanofibers grown at 435 K, which show a peak value in length, that corresponds to the ridge width, i.e. 2.5 μm (fig. 4.9) and 5 μm (fig. 4.10), respectively. This is not seen on 10 μm wide ridges (fig. 4.11), where the nanofiber lengths are shorter than the ridge width. Therefore, the nanofiber length does not only show the expected temperature dependence, but also a ridge width dependence. This is clearly seen in figure 4.12, which shows the mean length of the nanofibers as a function of ridge width for the different temperatures. The figure shows, that the nanofiber length increases with temperature and slightly increases with the ridge width, since at wider ridges, the nanofibers lengths are not limited by the ridge width, as on narrow ridges. Lines placed at 2.5 μm, 5 μm and 10 μm clearly show, that the nanofibers lengths are limited to the size of the ridges at 2.5 μm (at 435 K) and almost at 5 μm, whereas at 10 μm, the ridge width exceeds the fibers lengths. It should be noted, that the increase in length with temperature is not monotonic, instead the mean length actually decrease from 435 K to 449 K, independent of the ridge width (fig. 4.12). This decrease is not fully understood, however, it is supposed, that some of the nanofibers tend to break up at this high temperature and therefore lower the mean length. At temperatures around 460 K and above, no further nanofiber growth is observed, presumably due to the lower sticking coefficient of the incoming molecules at this temperature [1].

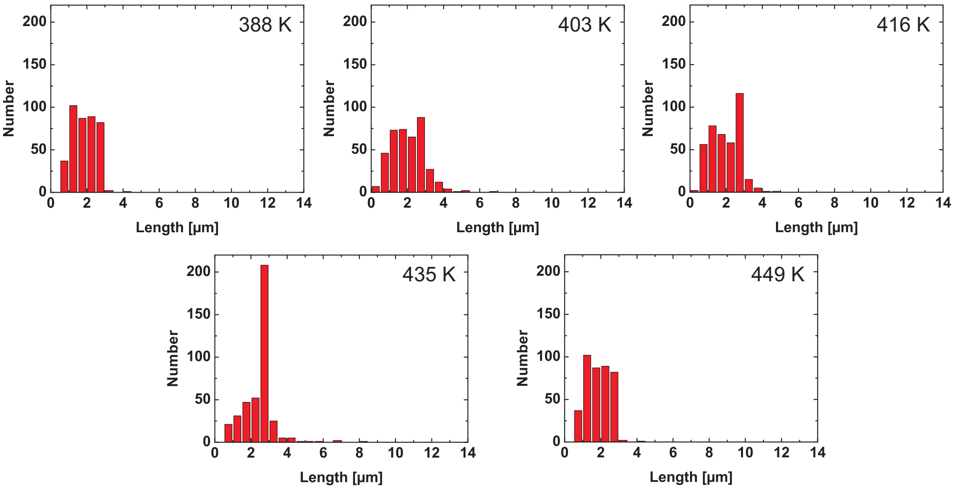

Figure 4.9: Length distribution of p6P nanofibers grown on 2.5 μm wide Au coated ridges at a substrate temperature of 388 K, 403 K, 416 K, 435 K and 449 K, respectively.

The orientational and length distributions dependence on both substrate temperature and ridge width can be explained as follows: At low substrate temperatures, short nanofibers are grown on the ridge, both near the edge and in the center part of the ridge. At these temperatures, the molecules or clusters have a relatively short diffusion length, and they therefore nucleate at the center part of the ridge away from an edge. This results in non-oriented nanofibers as it is the case for nanofibers grown on planar Au surfaces (sec. 3.4.4). At higher substrate temperatures, the diffusing molecules or clusters reach an edge, at which they nucleate, and nanofiber growth then starts. This result in nanofibers, which are oriented almost perpendicular to the ridge. Hence, oriented growth starts from an edge. The fact that the length of the nanofibers grown at high temperatures on 2.5 μm and 5 μm wide ridges peaks at 2.5 μm and 5 μm, respectively, is because the nanofibers are grown perpendicularly oriented to the ridge at these temperatures and therefore are limited in size by the ridge width. This

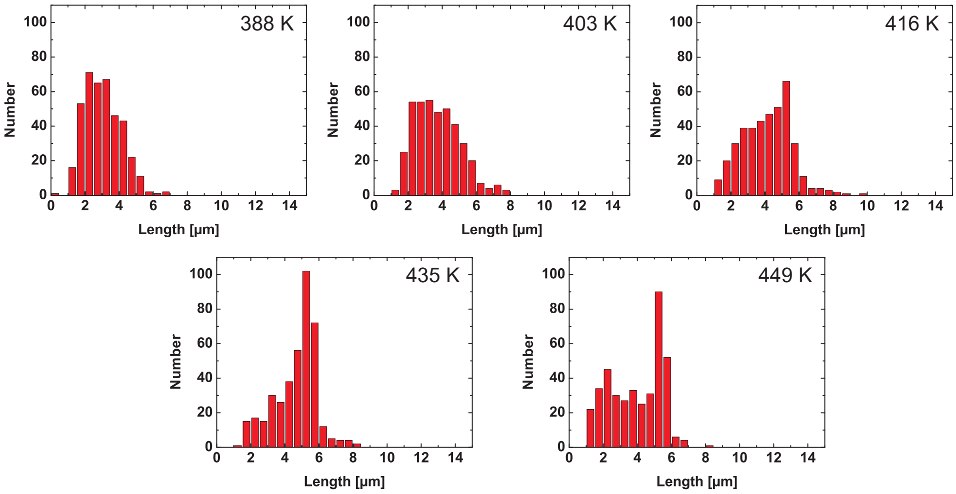

Figure 4.10: Length distribution of p6P nanofibers grown on 5 μm wide Au coated ridges at a substrate temperature of 388 K, 403 K, 416 K, 435 K and 449 K, respectively.

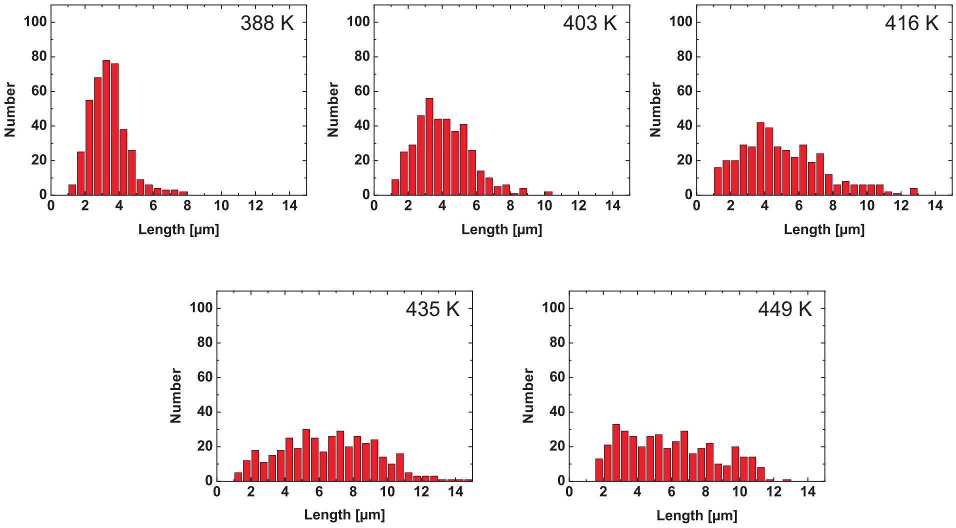

Figure 4.11: Length distribution of p6P nanofibers grown on 10 μm wide Au coated ridges at a substrate temperature of 388 K, 403 K, 416 K, 435 K and 449 K, respectively.

is not the case for nanofibers grown on 10 μm wide Au coated ridges, since the ridge width is bigger than the nanofiber length; therefore the nanofibers are less oriented on 10 μm wide ridges.

The difference in orientational and length distribution for nanofibers

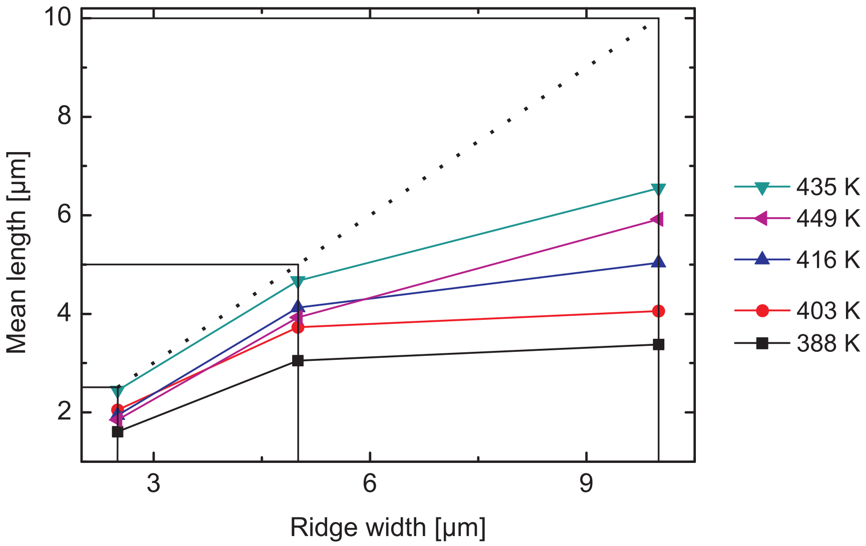

Figure 4.12: Mean length of p6P nanofibers as a function of the ridge width for nanofibers grown at a substrate temperature of 388 K, 403 K, 416 K, 435 K and 449 K, respectively. The dotted line shows the nanofiber length if full coverage of the ridge width is achieved.

grown on Au coated ridges and on a planar Au surface is demonstrated in fig. 4.13. The orientational distribution clearly shows random growth for nanofibers on the planar Au surface, compared to oriented growth on the ridges. The length distributions show that the ridge width clearly limits the length of the nanofibers on the ridges compared to the planar Au surface. A relatively large spread is observed in the length distribution on the planar Au surface. This is due to the fact that nanofibers branches into smaller fibers, i.e. smaller fibers are grown from bigger fibers, this is also seen in figure 3.12c. The mean length of the nanofibers is 18.5 μm on the planar Au surface compared to 3.9 μm on the 5 μm wide Au coated ridge.

The nanofiber morphology has been investigated by AFM. Figure 4.14 shows AFM images of p6P nanofibers grown on a 10 μm wide Au coated ridge at 388 K (fig. 4.14a) and at 449 K (fig. 4.14b). It is seen that the nanofiber density is higher at 388 K than at 449 K. Furthermore, clusters, whose size are temperature dependent, appear in between the nanofibers. Whereas the nanofiber density decreases with increasing temperature, the cluster density is seen to increase with temperature. These observations are qualitatively similar to those seen both for p6P nanofibers grown on muscovite mica (sec. 3.4.2) and for nanofibers grown on planar Au surfaces (sec. 3.4.4). Both the nanofibers and clusters increase in size with temperature, which is also similar to growth on planar Au surfaces (sec. 3.4.4) and

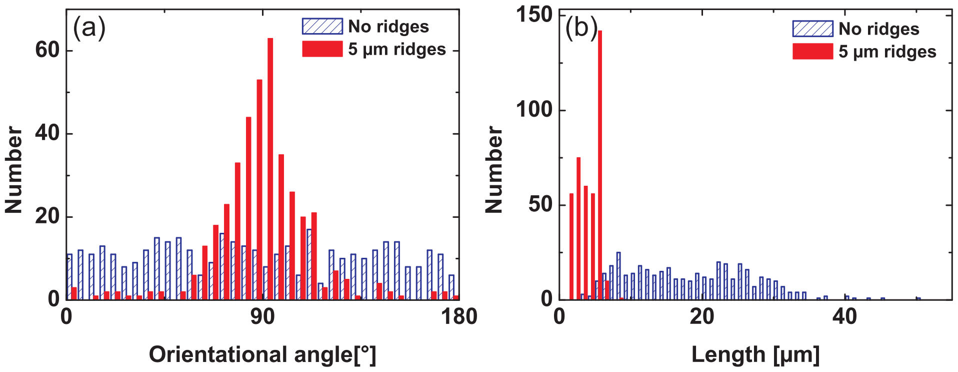

Figure 4.13: (a) Orientational and (b) length distributions of p6P nanofibers grown on 5 μm wide Au coated ridges and a planar Au surface, respectively. The nanofibers were grown at a substrate temperature of 449 K.

consistent with basic nucleation theory (sec. 3.4.1).

A closer look at the morphology of a single nanofiber grown on a 10 μm wide Au coated ridge (fig. 4.14c) and a planar Au surface (fig. 4.14d) shows as expected similar characteristics. Clusters, from which the nanofibers assemble, are visible around the nanofibers. Furthermore, the nanofibers grown on the ridge also exhibit the same kind of faceted morphology as nanofibers grown on planar Au surfaces. This is even more clear in figure 4.15 which shows a 3D representation of a single nanofiber grown on a 10 μm wide Au coated ridge at a substrate temperature of 449 K. The facets along the nanofiber are easily seen together with the clusters.

In this work, the crystalline structure of the nanofibers and their facets has not been determined. However, as described in section 3.3, polarized fluorescence microscopy images reveal, if there is an internal alignment of the molecules, from which the fibers are assembled. Figure 4.16 shows polarized fluorescence microscopy images of p6P nanofibers grown on a 5 μm Au coated ridge at a substrate temperature of 449 K. The polarizer direction is marked with arrows on the images. It is seen that the nanofiber fluorescence is intense, when the polarizer direction is almost perpendicular to the nanofibers, whereas almost no fluorescence is detected, when the polarizer direction is approximately parallel to the long nanofiber axes. This is similar to nanofibers grown on muscovite mica [96], and it indicates, that the nanofibers consist of molecules, that are mutually parallel, and aligned almost perpendicular to the long nanofiber axes.

Although it is argued, that oriented growth starts from an edge, the exact mechanism for this growth perpendicular to the ridges is still unclear. However, since the growth of nanofibers depends critically on the diffusing clusters and hence on surface temperature, it is tempting to assume, that

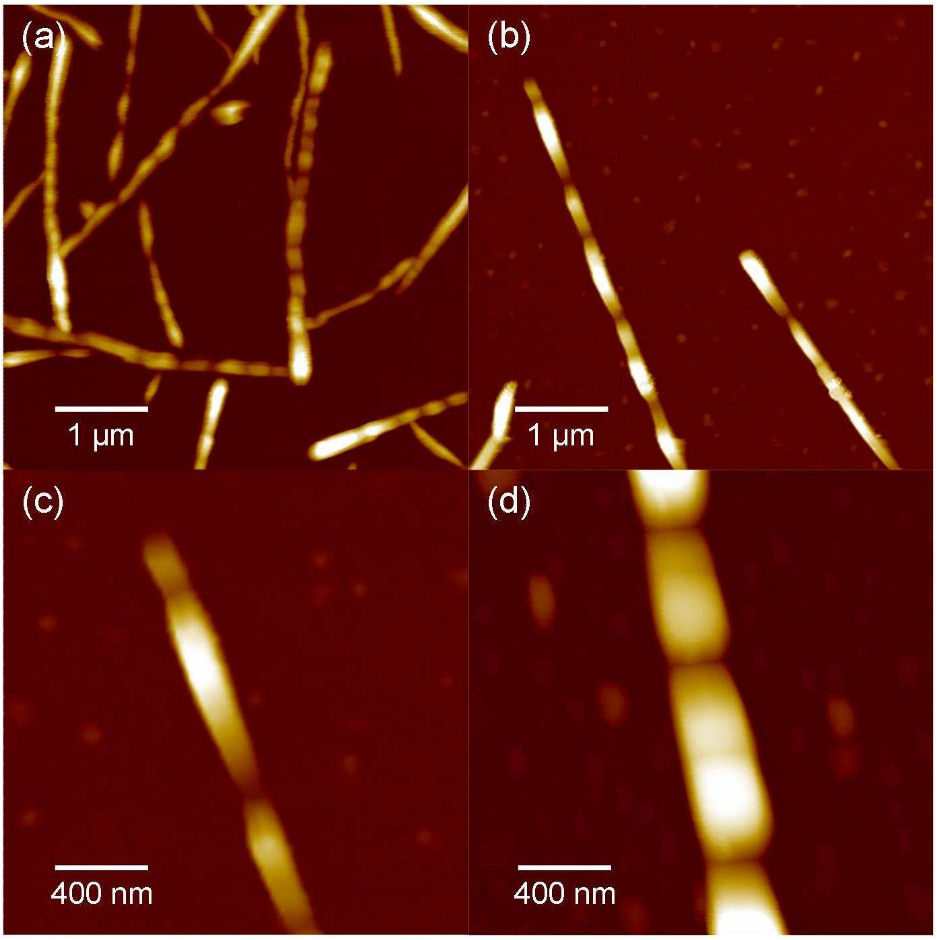

Figure 4.14: AFM images of nanofibers grown on a 10 μm wide Au coated ridge at (a) 388 K and (b) 449 K. AFM images of a single nanofiber grown at 449 K on (c) a 10 μm wide Au coated ridge and (d) a planar Au film. The height range is (a) 225 nm, (b) 269 nm, (c) 230 nm and (d) 174 nm, respectively.

temperature gradients on the structured surfaces affect the growth process. Note that the Au coating is covering only the horizontal parts of the surface. The vertical sidewalls are essentially not coated, i.e. are made of Si. Therefore, due to both the difference in the emissivity of Si and Au, and to the very geometry of the structures, temperature gradients is expected from the ridge edge to their centers. This has been investigated by using COMSOL Multiphysics version 3.4 (see appendix A). Although temperature gradients are found to be present on the structures, the small values of the gradients makes it unlikely, that these gradients alone account for the observed growth

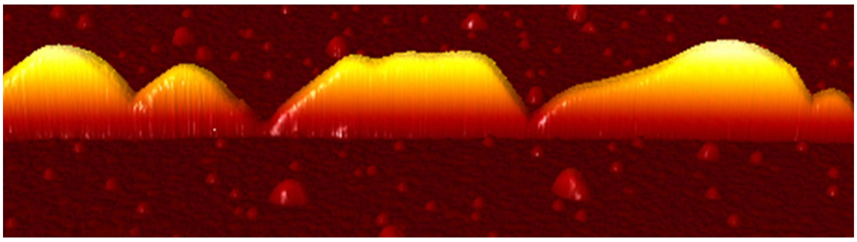

Figure 4.15: 3D AFM image of a single p6P nanofiber grown on 10 μm wide Au coated ridge at a substrate temperature 449 K. The width of the image is 3.3 μm and the height range is 262 nm.

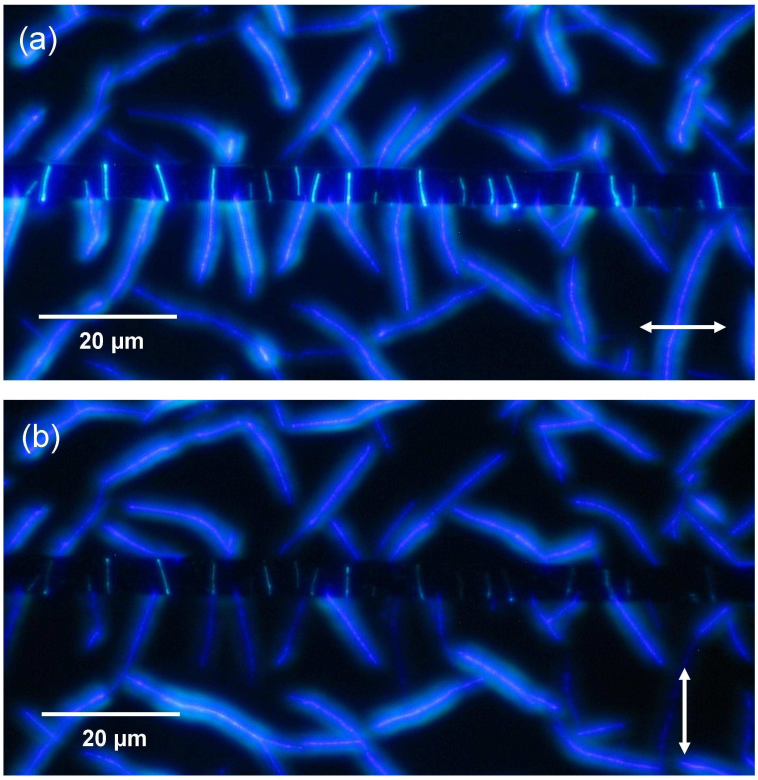

Figure 4.16: Polarized fluorescence microscopy images of p6P nanofibers grown on a 5 μm wide Au coated ridge at 449 K. The polarizer direction is marked with arrows.

perpendicular to the structures.

In previous studies, p4P needle growth perpendicular to small step edges in Au films has been demonstrated, indicating that the individual molecules align parallel to those edges [106]. However, in the case of microstructured ridges, the line edge roughness (sec. 2.4) of the ridges is much bigger than the individual p6P molecules, and it is therefore not expected, that an alignment of individual molecules or small clusters is responsible for the observed oriented growth.

4.1.2 Au coated micro-channels

In the previous section it was demonstrated, how microstructured ridges could guide the growth of p6P nanofibers into a preferred direction perpendicular to the long axes of the ridge. Since an edge is needed for oriented growth to take place, it is easy to be convinced, that a micro-channel could account for the same effect. Although no detailed analysis has been performed, figure 4.17 demonstrates, how a micro-fluidic channel can guide the growth of nanofibers into a preferred direction as well. The figure shows a SEM image of a micro-fluidic platform with a reservoir at the right, and a micro-fluidic channel connected to this reservoir. The channel depth is approx. 3 μm whereas the channel width is approx. 2 μm. The whole sample is covered with both Au and p6P. Inside the reservoir where no structures or edges appear, the nanofibers grow randomly in all directions. However, inside the channel, the nanofibers grow perpendicular to the channel, similar to nanofibers grown on ridges.

The micro-fluidic samples were produced by the S. Tamulevicius group from the Institute of Physical Electronics, Kaunas University of Technology, Lithuania. In short, the structures were fabricated in silicon(111) by optical lithography and reactive ion etching. The Si samples were cleaned in boiling dimethyl formamide and in an oxygen plasma. The structures were processed by RIE etching in the SF_6/N_2 gas mixture (at 0.6 W/cm_2 RF power density).

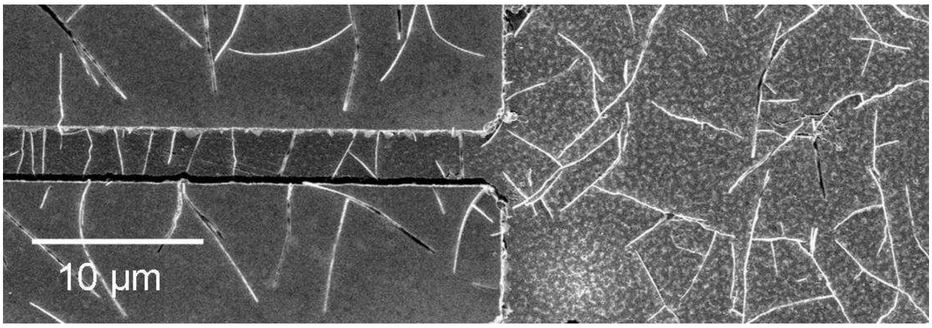

Figure 4.17: SEM image 10 nm p6P deposited on a Au coated micro-fluidic platform fabricated in silicon by optical lithography and reactive ion etching.

These observations demonstrate the flexibility of this *in-situ* growth method, since it is not limited to growth on top of a specific structure alone, but can be combined with other device configurations. However, further measurements are needed in order to demonstrate the alignment effect with respect to both temperature and channel dimensions. Also, since the nanofibers are grown on parts which have been etched in the RIE system, the effect of surface roughness is expected to play a role.

4.2 Au coated alumina templates

As an attempt to increase the growth control of p6P nanofibers on structured Au surfaces, a further downscaling of the structure dimensions has been employed. Typically, nanostructures in silicon are fabricated by electron beam lithography (EBL) and subsequent reactive ion etching. Although EBL allow for fabrication of smaller structures than optical lithography, fabrication of structures below 100 nm is both a difficult and time-consuming task. A much more simple approach for achieving periodic nanostructures in Au films is to use Au coated porous alumina templates. These templates are normally used for growth of both organic and inorganic nanofibers inside the vertically aligned pores [46, 47, 113], which after template removal results in an ensemble of standing nanofibers. However, since these templates can be fabricated with high pore regularity, they also become ideal templates for producing nanostructured Au surfaces, simply by coating the fabricated templates with a thin Au layer.

Although these templates allow for much less flexibility than EBL fabricated nanostructures in terms of structure dimensions and design, they are cheap, easily fabricated and also allow for nanofiber growth when coated with a thin Au layer. This is demonstrated in figure 4.18, which shows a tilted SEM image of 10.5 nm p6P deposited on a Au coated alumina template at a substrate temperature of 418 K. The template was coated with a thin Au layer prior to p6P deposition. Note that there is a crack in the template, which makes it possible to see the vertical pores in the template.

The Au coated alumina templates were produced by the M. Es-Souni group from the Institute for Materials and Surface Technology, University of Applied Sciences, Kiel, Germany. In short, the porous templates were fabricated by double anodization of a high purity (99.999%) aluminum foil under a constant voltage (40V) in an oxalic acid solution [112]. The pores produced from this process had a diameter of approximately 40 nm and a center to center distance of 105 nm. A SEM image of such a template is shown in Fig. 4.19. The pores are hexagonally-ordered in the surface plane, and have a moderate long-range ordering with domain sizes extending typically up to several micrometers. After processing, a thin Au layer is sputter-deposited on the templates (Emitech - K550, 12 V DC - applied to Au target, 2.5 cm target-substrate distance, 1x10^{-1} mbar Ar, I = 15 mA). The sputter deposition time is varied to investigate the influence of different

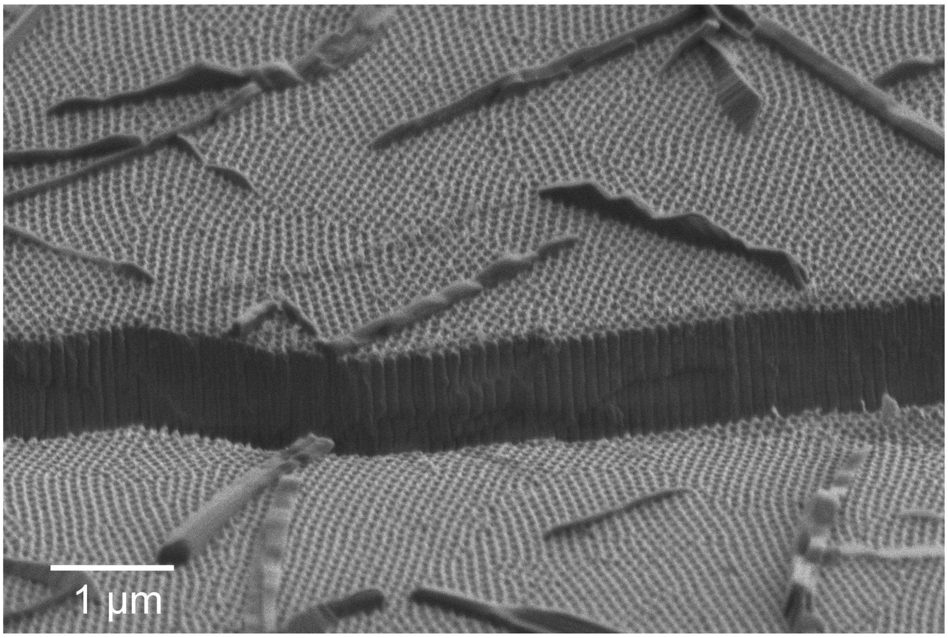

Figure 4.18: Tilted SEM image of 10.5 nm p6P deposited on a Au coated alumina template at a substrate temperature of 418 K.

Au thickness on the subsequent nanofiber growth.

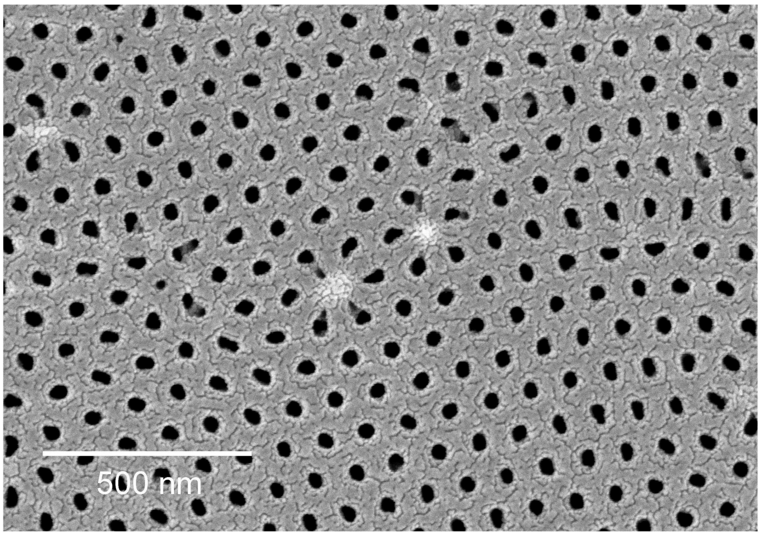

Figure 4.19: SEM image of a porous alumina template. The pore diameter is around 40 nm.

In figure 4.20 SEM images of 6 nm p6P deposited on different Au layers on an alumina template are shown. As it is seen, only elongated clusters are formed on the bare alumina template (fig. 4.20a). However, once a thin Au layer is deposited on the surface, nanofibers start to grow on top of the Au coated template. At thin Au layers, a mixture between nanofibers and islands are formed on the surface (fig. 4.20b-c), whereas only nanofibers are formed on thick Au layers (4.20d). The typical nanofiber length is a few micrometers. The p6P deposition is in all cases at a substrate temperature of 415 K.

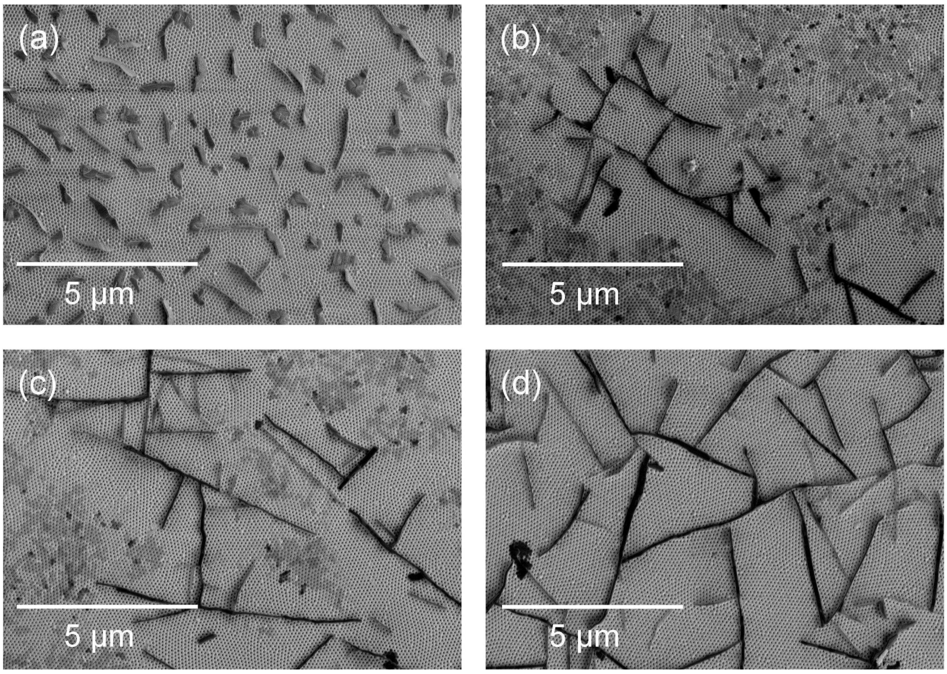

Figure 4.20: SEM images of 6 nm p6P deposited on a (a) bare and (b-d) Au-coated alumina template. The Au deposition time is (b) 3 minutes (c) 5 minutes and (d) 10 minutes, respectively.

In figure 4.21, the difference between growth on a bare (fig. 4.21a) and Au coated (fig. 4.21b) alumina template is more easily seen. Elongated cluster growth on bare templates is modified to fiber growth on the Au coated templates. Note that the pores become smaller when coated with Au, however, they still remain unsealed.

Fluorescence microscopy (fig. 4.22) investigations reveal, that the nanofibers grown on the Au coated templates consist of lying molecules. By rotating a polarization filter during the fluorescence microscopy investigations it is seen, that the nanofibers exhibit some degree of crystallinity, since the emitted fluorescence is polarized. However, since the nanofibers

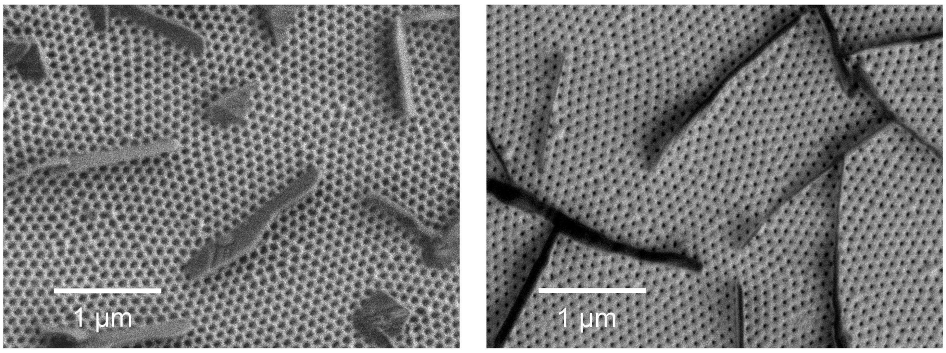

Figure 4.21: SEM images of 6 nm p6P deposited on a (a) bare and (b) Au-coated alumina template. Au deposition time: 10 min.

on a large scale grow randomly in all directions, this has not been imaged for an ensemble of nanofibers.

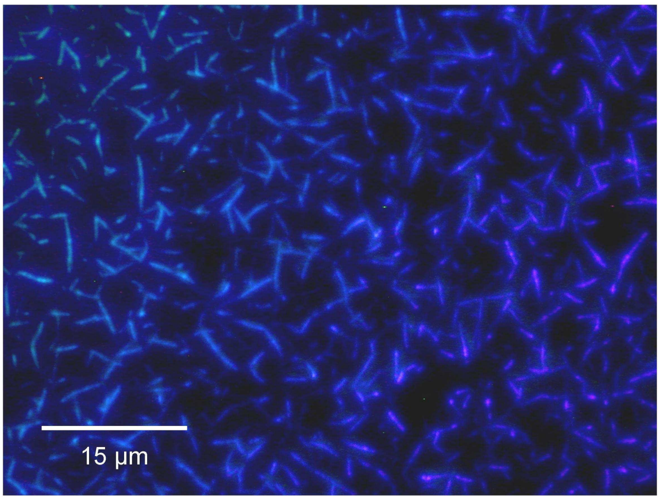

Figure 4.22: Fluorescence microscopy image of 6 nm p6P deposited on a Au-coated alumina template. Au deposition time: 10 min.

The fact that the nanofibers grown on the templates grow randomly in different directions suggests, that the pores have no ordering effect on the nanofibers. However, a closer look at the nanofiber growth reveals, that some of the nanofibers tend to grow along the directions of the ordered pores. This is demonstrated in figure 4.23, which shows a tilted SEM image of 6 nm p6P deposited on the Au coated template at a substrate temperature of 415 K. This indicates that the pores, to some extend, guide the diffusing molecules, so that nanofibers are formed in specific directions defined by the pore ordering on the template. The reason why no order is seen on a large scale is partly due to the fact, that the pores are only ordered within domains of a few tens of micrometers at maximum, i.e. due to the changing domain boundaries, the nanofibers are not ordered on a larger scale. It should be mentioned that although some fibers align along the pore directions, some also grow across a line of pores.

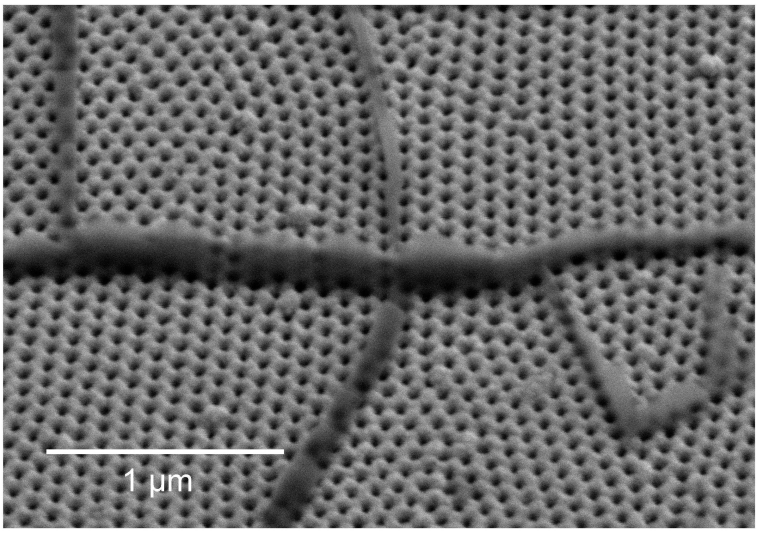

Figure 4.23: SEM images of 6 nm p-6P deposited on an alumina template at a substrate temperature around 415 K.

In order to investigate this in more detail, a thinner p6p layer is deposited on a Au coated alumina template. Figure 4.24 shows SEM (fig. 4.24a) and AFM (fig. 4.24b) images of 2 nm p6P deposited on a Au coated alumina template at a substrate temperature around 415 K. The images are from areas where only very small or no nanofibers are grown.

From the images it is seen, that the porous template consists of clusters that are hexagonally ordered around the pores. As it is seen from the SEM image, some of the small fibers which are formed on the template tend to grow in between these clusters. This effect is seen even more clear on the AFM image, where a small layer of p6P seems to grow from the pores and in between the hexagonally ordered clusters, i.e. the ordered valleys between the clusters seem to act as nucleation centers for the diffusing p6P molecules or clusters. Therefore, the early stage of growth could be similar to that observed for growth on microstructured ridges; the diffusing molecules or clusters nucleate at a surface imperfection or defect where diffusion is hindered, and from here the nanofibers grow. It is therefore assumed, that if the pores are ordered, fiber growth along a symmetry direction is preferred. However, more investigations are needed for making a quantitative analysis

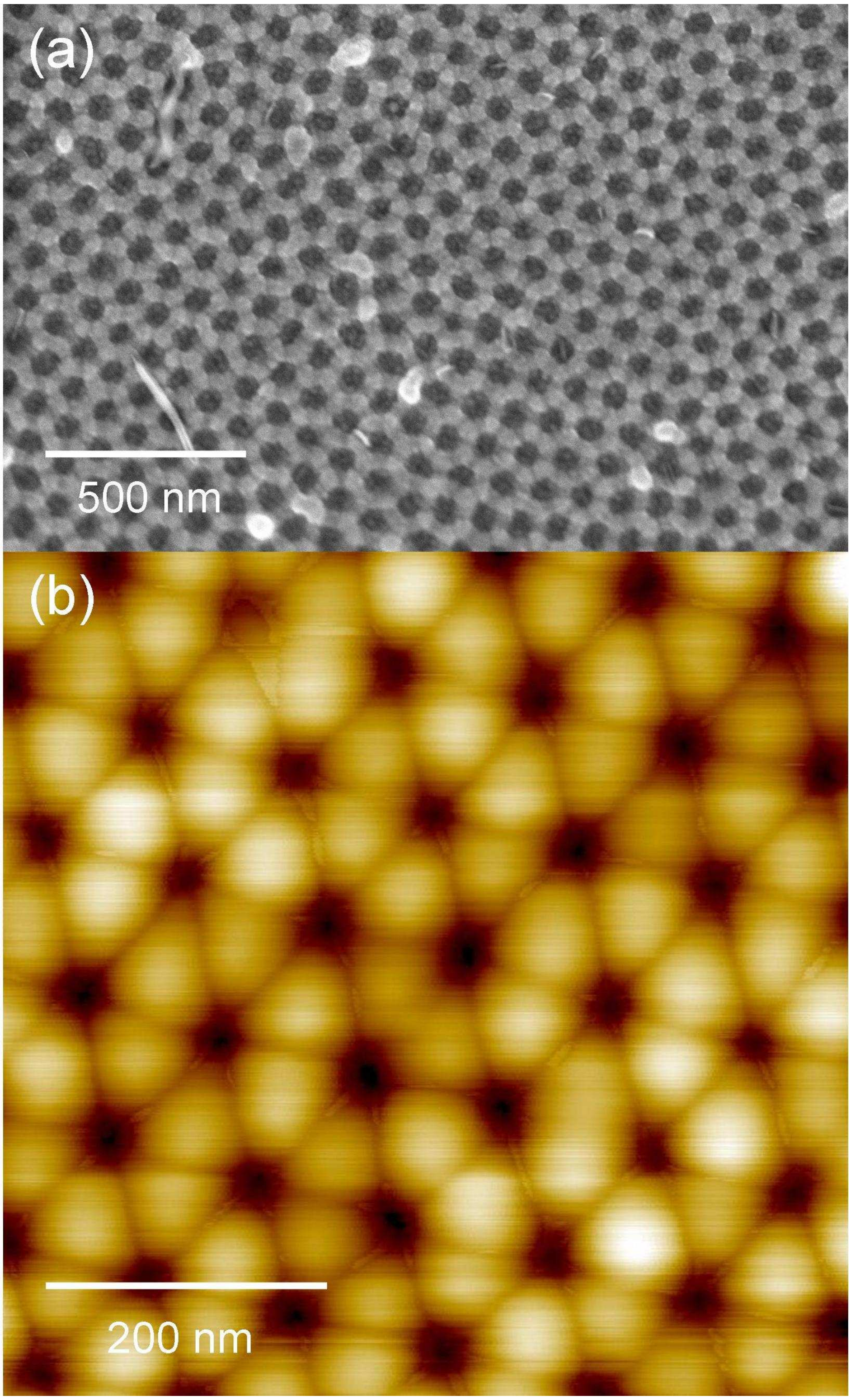

Figure 4.24: (a) SEM and (b) AFM image of 2 nm p-6P deposited on an alumina template at a substrate temperature around 415 K. The height range on the AFM image is 33 nm.

of this effect, which for example include the influence of changing pore sizes. The reason that some of the nanofibers grow across a line of pores could be, that the pores are too small compared to the nanofibers. This could maybe be avoided if the pore sizes are increased. Also parameters such as the substrate temperature and p6P thickness could have an effect on this growth process. Furthermore, the use of electron beam lithography would allow for testing of different nanostructured configurations, which is not possible with the alumina template approach.

4.3 Summary

In this section it has been demonstrated, that it is possible to modify the growth of p6P nanofibers on Au surfaces in a controlled way, by periodically structuring the Au surface. Two main techniques have been employed for fabricating the structured Au surfaces:

- Microstructured Au films are fabricated on silicon by optical lithography with subsequent reactive ion etching and metal deposition.
- Nanostructured Au films are fabricated by metal deposition on porous alumina templates, fabricated with high pore regularity.

The periodic microstructures have an ordering effect on the grown nanofibers, so that growth perpendicular to the structures is mainly observed. In the case of micro-ridges, this orientation effect is shown to be strongly dependent on the substrate temperature during growth; growth perpendicular to the structures is observed at high temperatures, whereas random growth is observed at low temperatures. Furthermore, the width of the ridges also influence the growth; narrow ridges (2.5 μm) lead to a stronger alignment of the fibers than wide ridges (10 μm). This can be explained by the assumption that oriented growth perpendicular to the structures begins at the edge of the structure. Therefore, when the temperature is sufficiently high and the ridge width sufficiently low, the diffusing species, from which the nanofibers are assembled, can reach an edge, which leads to growth perpendicular to the structure. At low temperatures or wide ridges, nucleation takes place away from an edge, leading to random growth as on planar Au surfaces. The ridges also affect the length distribution of the nanofibers. On ridges, the length of the nanofibers is much smaller than on planar Au surfaces, and the distributions are much more narrow. This is due to the ridge limiting the length of the nanofibers. Furthermore, oriented growth in a microstructured channel, perpendicular to the long channel axis, has also been demonstrated, although only qualitatively. The exact mechanism for the growth perpendicular to the microstructures is still unclear.

Growth on nanostructured Au coated alumina templates has shown, that the ordered pores in the Au film have an effect on the nanofiber growth on top of the film. In the initial growth stage, the p6P layer seems to form in between clusters hexagonally ordered around the pores, and hence, the nanofibers tends to favor growth along one of the symmetry directions of the ordered pores. However, when the nanofibers grow too big, they start to grow across a line of pores, probably due to the small dimensions of the pores. Furthermore, the pores are only ordered within micrometer-sized domains, which makes it impossible to achieve an ordering of the p6P nanofibers on a larger scale (several tens of micrometers), for that, further experiments with electron beam lithography fabricated nanostructures are needed.

Chapter 5

Methods for integration of nanofibers

Organic nanofibers can be positioned on device platforms either by *in-situ* growth, as demonstrated in sec. 4, or by transferring of the nanofibers. However, since transferring on specific, micron-sized regions is so far not possible, structuring has to be made after transferring, in order to obtain well defined regions with mutually parallel nanofibers. In this section, results from a simple method for transferring organic nanofibers are reported. The method allows both for transferring onto planar surfaces and into nanofiber suspensions. Furthermore, structuring of transferred nanofibers by laser ablation is demonstrated.

5.1 Transferring of organic nanofibers from muscovite mica

P6P nanofibers can be transferred from muscovite mica by wetting of the nanofiber covered mica surface with water, whereupon the nanofibers detach from the surface [114]. The nanofibers can then either be transferred onto a planar surface, simply by pressing the mica against the planar surface immediately after wetting or, alternatively, the water can be collected a few minutes after wetting of the mica surface, by which process a suspension with nanofibers is obtained. Figure 5.1a shows a fluorescence microscopy image of an ensemble of nanofibers transferred from muscovite mica onto glass, by pressing of the mica surface against the glass after wetting with water. Note that the nanofibers retain their parallelism in this transferred region. Furthermore, fluorescence microscopy images of nanofibers integrated into a capillary tube are shown (fig. 5.1b and fig. 5.1c). In this case, the nanofibers have been transferred to a suspension with water, which subsequently has been sucked through the capillary tube. The inner diameter of the tube is 19 μm. Note that the nanofibers tend to align along the direction of the capillary tube.

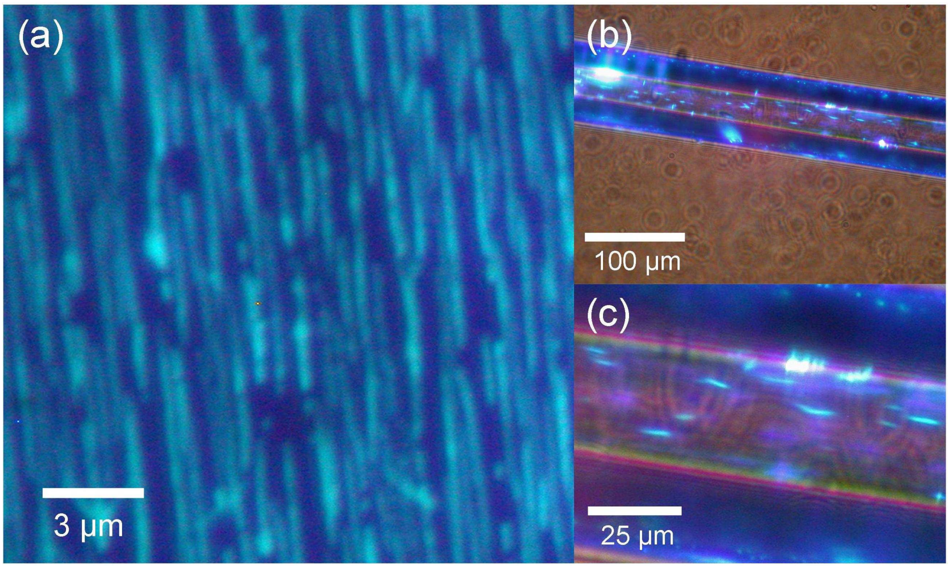

Figure 5.1: Fluorescence microscopy images of (a) p6P nanofibers transferred onto glass [115] and (b-c) into a capillary tube. The inner diameter of the tube is 19 μm. Note that there is a lens effect due to the curved surface of the tube.

Although these methods describe a simple way of placing the nanofibers at specific positions, difficulties in controlling the transfer makes the usefulness of these methods limited. In case of transfer of the nanofibers into capillary tubes, the nanofibers easily stick to each other and to the capillary tube, which makes it difficult to transfer them in a controlled way, as it has been demonstrated for inorganic nanowires [36]. As for the transfer to planar surfaces, controlled transfer onto well defined, micron-sized regions is so far not possible, which limits its use for applications. For manipulation of individual nanofibers after transfer, scanning probes [17, 52], cantilevers [51] or other micromanipulators [29] can be employed. Although these methods offer control of individual 1-D nanostructures, they are rather time-consuming and must be considered barely as methods for building up prototype systems. Besides that, these methods can be rather deteriorating, and in the case of organic nanofibers lead to damage of the individual nanofibers [51, 52]. In the following section, a method for structuring an ensemble of transferred nanofibers by laser ablation is demonstrated. This methods results in mutually parallel nanofibers in specific regions on different substrates.

5.2 Structuring of organic nanofibers by laser ablation

In this section, cutting of p6P nanofibers on glass is demonstrated as a method for structuring an ensemble of nanofibers. In these experiments, an ArF excimer laser emitting at 193 nm was used (for experimental details see [115]). Figure 5.2a shows a fluorescence microscopy image of p6P nanofibers, which have been transferred onto a glass surface, and subsequently ablated in a selected area with the 193 nm laser light. The output energy of the excimer laser was around 50 mJ. The AFM image (fig. 5.2b) reveal, that the glass surface is molten by the UV laser light and shows a rippled structure.

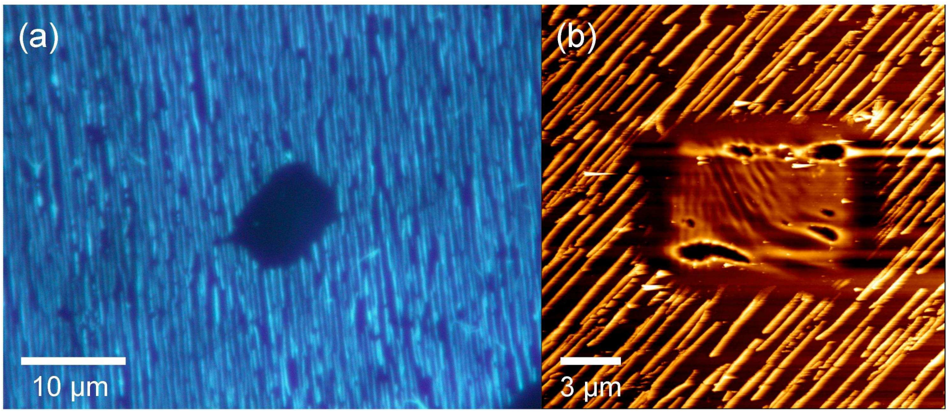

Figure 5.2: (a) Fluorescence microscopy image of laser ablated p6P nanofibers on glass. (b) AFM image of the same ablated area as shown in (a). The laser wavelength was 193 nm. [115]

A close-up of the cut nanofibers reveals, that the steepness of the cut is around 600 nm (fig. 5.3). Note from the line profile in figure 5.3, that a natural occurring break in the nanofiber shows much steeper profile compared to the laser cut.

By lowering the laser output energy, the nanofibers can be cut without melting the underlying glass. This is demonstrated in figure 5.4, which shows AFM images of ablated p6P nanofibers on glass, the output energy was in this case around 10 mJ. The nanofibers have been cut with (a) 1, (b) 3 and (c) 5 laser pulses, respectively. It is seen, that after irradiation with a single pulse (fig. 5.4a), the nanofibers are only slightly modified, whereas after 3 (fig. 5.4b) and especially 5 pulses (fig. 5.4c), both the nanofibers and the small clusters in between the nanofibers are removed. This is easily seen in the close-up image of the area ablated with 5 pulses (fig. 5.4d). It should be noted that debris from the nanofiber cutting is present around the ablated areas.

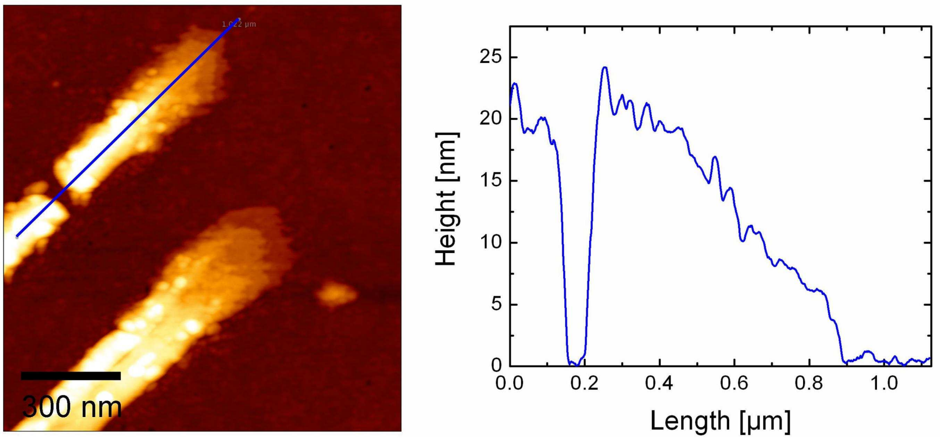

Figure 5.3: AFM image of two laser ablated p6P nanofibers with a measured line profile along one of the fibers. The difference in steepness of a natural occurring break in the nanofiber and the cut end is easily seen. [115]

The steepness of the cut nanofibers has also been investigated at this lower output energy. Figure 5.5 shows AFM images of nanofibers cut with the 193 nm laser light at three different focus positions, namely 0 μm, -15 μm and -30 μm, respectively (arbitrary values). The nanofibers have been cut with three laser pulses at an output energy of around 10 mJ in all cases. At the 0 μm position, the nanofibers are not completely removed by the laser light whereas at -15 μm they are almost fully ablated. At -30 μm, the nanofibers are fully removed, and the underlying glass appears slightly molten. In figure 5.5d, the measured line profiles for each focus position are shown. It is clearly seen that the nanofibers cut with the laser light at a focus position of -30 μm show the steepest profile, with a steepness around 400 nm. From this it is concluded that the sharpest focus is reached around -30 μm.

5.3 Conclusions

In this section, methods for integration of p6P nanofibers by transfer has been demonstrated. The nanofibers are transferred by a simple technique, in which the nanofibers are either transferred as an ensemble onto planar substrates, or by adding them to a nanofiber suspension, in which they can be transferred into micro-channels. Structuring of an ensemble of nanofibers has also been demonstrated. This is done by laser ablation of the transferred nanofibers in selected areas, using a 193 nm ArF excimer laser. A minimum steepness of around 400 nm for the cutting region has been obtained.

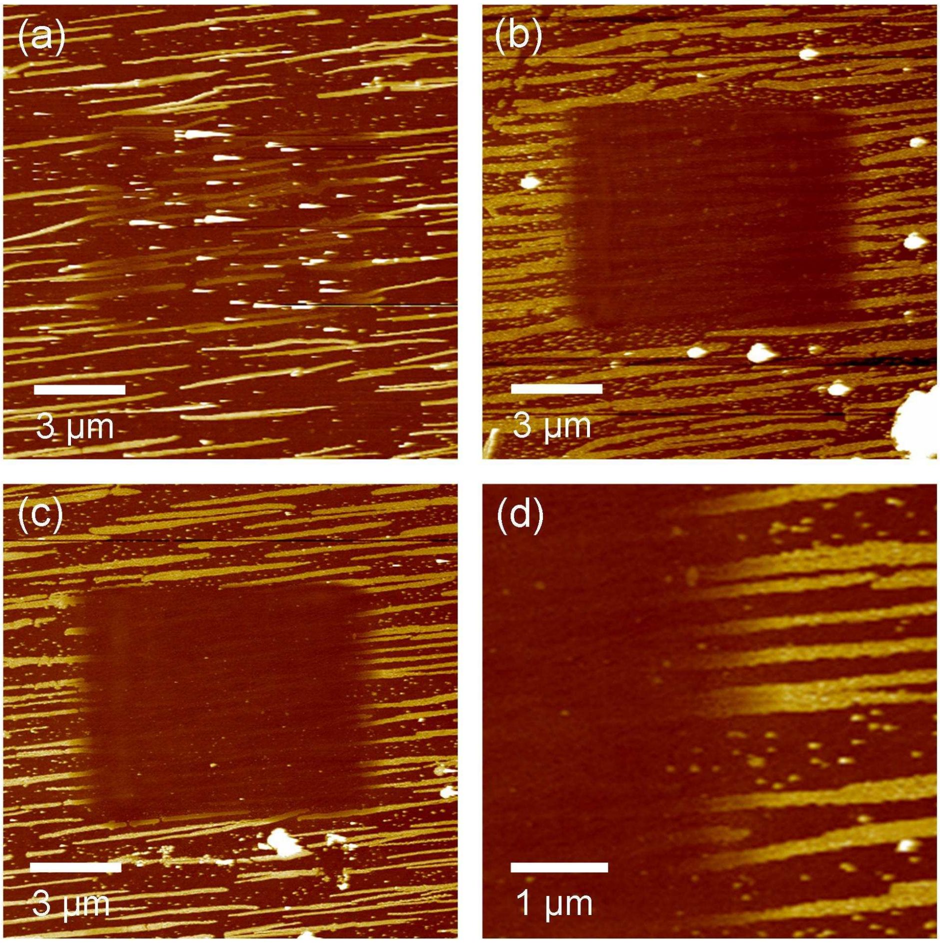

Figure 5.4: AFM images of laser ablated p6P nanofibers on glass. The nanofibers have been ablated with (a) 1, (b) 3 and (c) 5 laser pulses, respectively. In (d), a zoom-in image of the nanofibers ablated with 5 pulses is shown. Note that both the nanofibers and the small clusters in between them are removed.

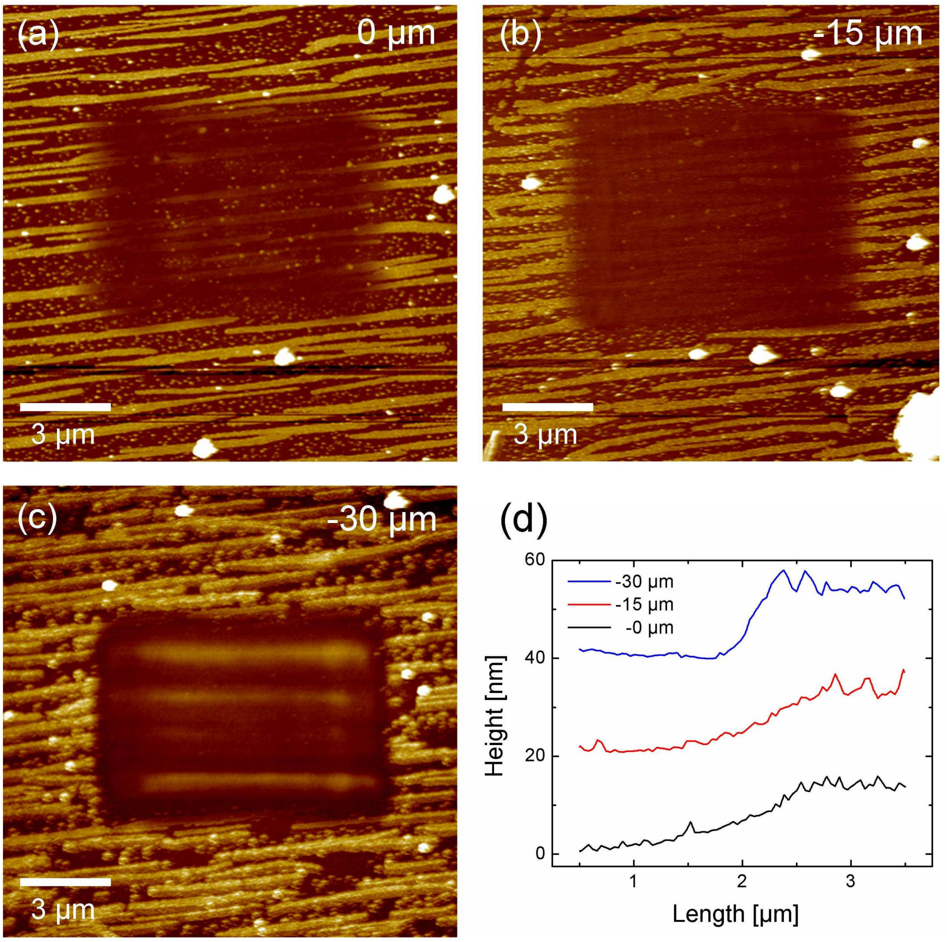

Figure 5.5: AFM images of p6P nanofibers on glass, irradiated with 193 nm laser light with a focus position of (a) 0 μm, (b) -15 μm and (c) -30 μm, respectively. (d) Measured line profiles for cut nanofibers at the different focus positions. At optimum position, a steepness of 400 nm is obtained. [115]

Chapter 6

Conclusions and outlook

In this project, growth and integration of organic nanofibers have been investigated. The main focus areas have been growth of nanofibers on planar surfaces and on micro- and nano-structured surfaces. Furthermore, integration of nanofibers by transferring and subsequent laser structuring have been demonstrated. In the following, the main results in these areas are summarized.

6.1 Growth of nanofibers on planar surfaces

This work is focused on nanofibers based on the molecule *para*-hexaphenylene (p6P), which can self-assemble into nanofibers on specific surfaces, when deposited by physical vapor deposition under high vacuum conditions. The vacuum system used in this work is a two-chamber organic molecular beam epitaxy system, in which the molecules can be deposited on various heated substrates under different conditions. It is demonstrated, how deposition onto muscovite mica leads to growth of long, mutually parallel nanofibers, which are quantitatively similar in terms of density and dimensions to those reported by others in previous studies [96]. This is used as reference measurements for the later experiments.

It is shown, that deposition of p6P molecules on gold surfaces also leads to nanofiber growth. In contrast to crystalline gold surfaces, as examined in previous studies [6, 7], the gold surfaces in this project are prepared by electron beam deposition of a gold film (around 50 nm) on silicon and glass substrates. Although these gold surfaces lead to growth of nanofibers, the fibers are grown randomly in all directions with a broad length distribution. Other metals are also examined for nanofiber growth. These include aluminum, silver, titanium and chromium. Only nanoscaled p6P clusters or islands are observed on these surfaces, except at high surface temperatures, where short nanofibers are observed on silver. The reason for the big difference in the nanostructures formed on the different metal surfaces is unknown, however, it is expected that oxidation of the metal surfaces, which leads to a decreased surface energy, has an influence on the growth.

6.2 Growth of nanofibers on structured surfaces

Two different types of structured gold surfaces have been investigated in this project. This is microstructured gold surfaces, fabricated by conventional microfabrication techniques in silicon with subsequent gold deposition, and nanostructured gold surfaces, fabricated by gold deposition on nano-porous alumina templates.

6.2.1 Microstructured gold surfaces

Within the microstructured configuration, both micron-sized ridges and channels have been examined. Deposition of p6P molecules onto the heated surfaces show in both cases directed growth of nanofibers, namely growth of nanofibers perpendicular to the microstructures. In the case of the ridges, this effect has been analyzed in detail, by measuring orientational and length distributions as a function of both ridge width and surface temperature. It has been demonstrated, that smaller ridges and higher surface temperatures (until a specific maximum in reached) lead to a better alignment of the nanofibers. At these conditions, growth perpendicular to the ridges is observed. Furthermore, the length of the nanofibers are at high temperatures and small ridge widths limited by the width of the ridges. It is argued, that the oriented growth starts from the edges of the ridges, which explains the strong dependence on both ridge width and surface temperature. Therefore, by controlling these two parameters with respect to each other, oriented growth can be observed. However, the reason for the growth perpendicular to the ridges is still unknown. Both temperature gradients, and an effect from alignment of molecules or clusters at the ridge edges, could be of influence. The temperature profiles of the ridges have been simulated, and temperature gradients perpendicular to the long ridge axes observed. However, due to the small values of these gradients, it is assumed to be unlikely, that the gradients alone account for the alignment effect. Furthermore, due to the big line edge roughness of the structures, an alignment effect at the ridge edges is not expected. However, further investigations are needed, in order to determine the exact mechanism for the oriented growth. In the case of microstructured channels, it has been demonstrated, that nanofibers can be grown perpendicular to the channels, although this has not been analyzed in detail, as in the case of microstructured ridges.

6.2.2 Nanostructured gold surfaces

Nanostructured gold surfaces has also been investigated as substrates for oriented growth of p6P nanofibers. These substrates were prepared by gold deposition on porous alumina templates, which displayed a high pore regularity with mono-domain sizes ranging from a few to a few tens of micrometers. Although some nanofibers seem to grow along the high symmetry directions of these pores, the changing domain boundaries inhibit a long range order of the nanofibers, since the domains are not much larger than the length of a single fiber. Furthermore, when the nanofibers are too wide, they do not all follow a specific symmetry direction of the pores, i.e. they tend to grow across a line of pores. When depositing ultra-thin p6P layers, however, indications of p6P nucleation between hexagonally ordered clusters is seen. This leads towards the same conclusions as for the microstructured surfaces: Directed growth starts with nucleation of the p6P molecules or clusters at fabricated surface structures. By controlling the dimensions, quality, periodicity etc. of these structures, one can steer the growth of the nanofibers into preferred directions. Polarized fluorescence microscopy investigations have revealed that the grown nanofibers consist of lying molecules, and that they are to some extend crystalline, since they emit polarized fluorescence. This is the case for nanofiber growth on both the nano- and micro-structured substrates.

6.3 Integration of nanofibers

Integration of nanofibers by transferring has been demonstrated. The nanofibers are either transferred as an ensemble on planar surfaces or into microchannels through a nanofiber suspension. Although these simple methods work, the fluidic integration is so far limited to very small areas, whereas the transfer to planar substrates is difficult to perform in a controlled way in specific areas. Structuring of an ensemble of nanofibers after transferring has been demonstrated. The structuring is done by laser ablation, using an ArF excimer laser with a wavelength of 193 nm. This method therefore describes an alternative way of achieving mutually parallel nanofibers at specific positions on different substrates. However, there are several drawbacks when using this method. First of all, the difficulty in transferring an ensemble of parallel nanofibers at a large scale restrain its use to minor areas. Furthermore, problems related to the ablation method, such as damaging of the substrate and contamination from nanofiber debris, need to be controlled. A minimum steepness of around 400 nm for the cutting region has been obtained.

6.4 Outlook

For growth on planar metal surfaces, further experiments on various other metals could be useful, in order to understand the basic conditions needed for obtaining nanofiber growth. This is for example the influence of surface energy (after possible surface oxidation), surface roughness and metal thickness. In the case of growth on structures surfaces, further experiments on nanostructured gold surfaces should be made, in order to obtain knowledge on the initial growth stage. Electron beam lithography should be employed, in order to fabricate nanostructures with different dimensions, and in different configurations. New experiments using this method are being performed by R. Melina de Oliveira Hansen [116], which so far confirm the results demonstrated in this work, namely that nanofibers grow perpendicular to line structures.

The results presented in this work could be useful for *in-situ* growth of organic nanofibes on device platforms. However, the growth is so far limited to be on gold surfaces, which of course is an important consideration for the device functionality. In many applications, such as solar cells [27], field effect transistors [31] and light emitting diodes [32, 117], electrical contacts are established to each end of the nanofibers, which are placed on an insulator. This is so far not possible with this method. However, SEM investigations has demonstrated, that the nanofibers in certain cases grow out from the ridges, indicating, that they could grow across small gaps in the Au surface (this is also seen on fig 4.4b). This could make it possible to establish electrical contact to the two ends of a nanofiber, and potentially limit contact problems, since the nanofibers are grown directly on the contact electrode. Furthermore, the thin gold film allows for surface plasmon polariton (SPP) excitations [118], which could be useful for SPP waveguiding in organic nanofibers. Therefore it is believed, that this method could be useful within optical and nanophotonic as well as electrical applications.

Appendix A

Temperature gradients on microstructured ridges

The fact, that the density and dimensions of p6P nanofibers are strongly influenced by the surface temperature during growth, makes it relevant to investigate the temperature profile across the substrate surface when it is heated. In the case of planar substrates with homogeneous surface composition, this is less interesting, since a uniform temperature across the substrate surface can be assumed. However, for structured surfaces, which consist of different materials, as it is the case for micron-sized, gold coated silicon ridges (sec. 4.1.1), a more complex temperature profile is expected to be present. In previous studies it has been demonstrated, that both the dimensions and density of p6P nanofibers on muscovite mica can be modified by local heating with an Argon ion laser [119], indicating that not only the absolute temperature but also temperature gradients could have a possible effect on the nanofiber growth. In the case of growth on microstructured ridges, temperature gradients perpendicular to the ridges are expected to be present during heating, due to both the very geometry of the ridges and due to the different materials on top (Au) and on the sides (Si) of the ridges. The temperature profiles of the different ridges have been modeled by using COMSOL Multiphysics version 3.4. In this simple 2D model it is assumed, that the temperature below the ridge is constant, i.e. the ridge is heated uniformly by the whole Si sample and therefore only the ridge, and not the rest of the sample, is taken into account. Furthermore, only heat transfer by conduction in the material and radiation is considered, assuming bulk values for both silicon and gold. The emissivity has been set to $\epsilon_{Au} = 0.02$ for gold and $\epsilon_{Si} = 0.6$ for silicon. The ridges have a height of 3 μm and widths of 2.5 μm, 5 μm and 10 μm, respectively. It should be noted, that in the figures, the scaling in the y-direction (height of the ridges) is twice as big as in the x-direction (width of the ridges) within each profile. Furthermore, each profile has its own temperature scale.

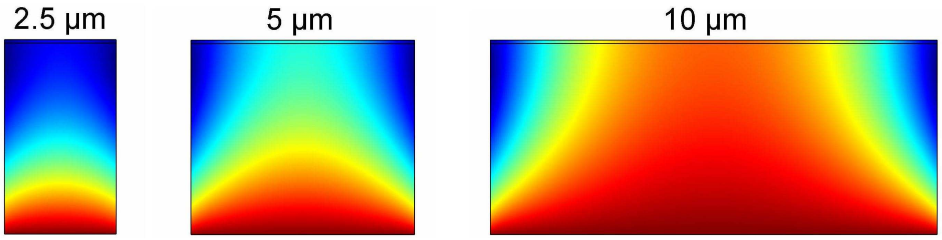

Figure A.1: 2D model of temperature profiles for Au coated Si ridges with widths of 2.5 μm, 5 μm and 10 μm, respectively.

In figure A.1, the temperature profiles for Au coated silicon ridges are shown for ridge widths of 2.5 μm, 5 μm and 10 μm, respectively. The thickness of the Au is 55 nm. It is seen, that a temperature gradient is present on the substrate surface perpendicular to the ridge. This is both due to the geometry of the ridge and the difference in emissivity of Si and Au. As a consequence, the sidewalls are cooled more than the top of the ridge, which gives rise to funnel shaped heat profiles from the heat source (constant temperature at 450 K is assumed just below the ridge). Temperature profiles for pure Au (fig. A.2) and Si (fig. A.3) ridges has also been modeled[1].

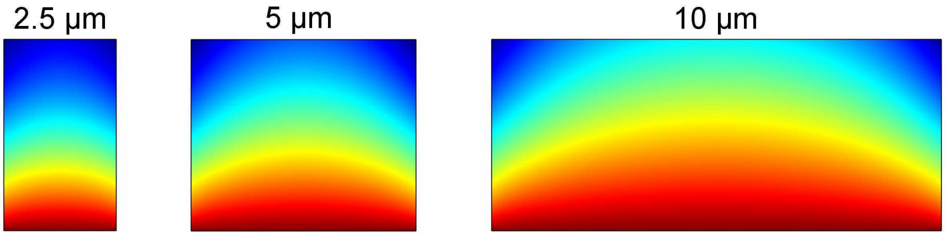

Figure A.2: 2D model of temperature profiles for pure Au ridges with widths of 2.5 μm, 5 μm and 10 μm, respectively.

Indeed temperature gradients perpendicular to the ridges are still present, although the profiles appear as more circular shaped from the heat source, since the ridges are cooled equally on the sides and on the top. This demonstrates, that the temperature gradients on the Au coated Si ridges originate both from the geometry of the ridge, and from the different materials on the side and top of the ridge. In general however, the size of the modeled temperature gradients is small, both on Au coated Si ridges and on pure Au and Si ridges. In figure A.4, the temperature gradients for Au coated Si, pure Au and pure Si ridges, respectively, are plotted for 2.5 μm, 5 μm and

---

[1] It should be noted, that the temperature scales are not shown on the individual profiles, instead values for the temperature gradients are given in figure A.4

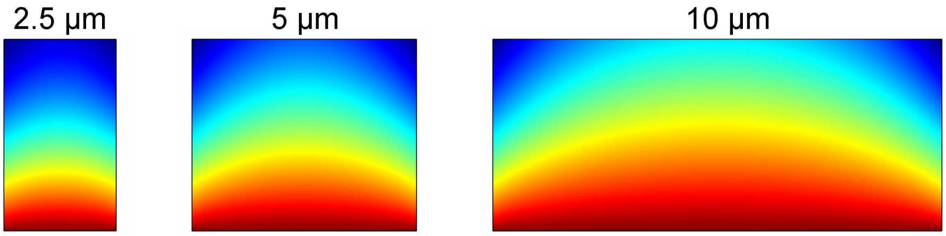

Figure A.3: 2D model of temperature profiles for pure Si ridges with widths of 2.5 μm, 5 μm and 10 μm, respectively.

10 μm wide ridges[2].

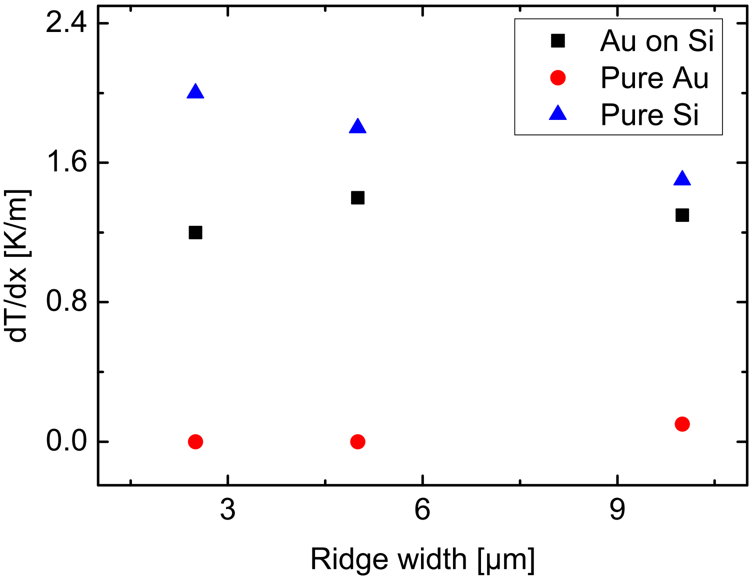

Figure A.4: Modeled temperature gradients for Au coated Si, pure Au and pure Si ridges with widths of 2.5 μm, 5 μm and 10 μm, respectively.

It is seen from the figure, that the largest gradients are present, when the ridge consists of pure Si, whereas for pure Au, the gradients are very small[3].

---

[2] The gradients are given as the ratio between the temperature difference at the center of the ridge and the ridge edge, with respect to the corresponding distance. This therefore gives an average value of the gradient perpendicular to the ridge

[3] From an experimental point of view it should be noted, that a pure Si and Au ridge is only interesting for comparing the temperature profiles with Au coated Si ridges.

For the Au coated Si ridges, the temperature gradients are smaller than for the values of pure silicon ridges, although this difference is decreasing with an increasing ridge width. This demonstrates, that the temperature gradients, that are present on the ridges, arise as a consequence of both the geometry of the ridges and the different materials present on the top and on the sidewalls of the ridges.

In conclusion, the temperature profiles modeled for the microstructured ridges show, that temperature gradients are present on the substrate surface, perpendicular to the gold coated silicon ridges. However, the modeled gradients are very small, with typical values around 1.3 K/m.

Appendix B

Publication list

The list is ordered chronologically by date of publication.

- F. Balzer, R. Frese, M. Madsen, K. Thilsing-Hansen and H.-G. Rubahn. *UV-Laser Treatment in the Nanodomain: Forming of Organic Nanofibers* J. Laser Micro/Nanoeng. 1, pp. 275-280 (2006).
- M. Madsen, M. Schiek, P. Thomsen, N. L. Andersen, A. Lützen and H.-G. Rubahn. *Organic nanofiber nanosensors* Proc. SPIE. 6769, pp. 676908 (2007).
- F. Balzer, J. Brewer, J. Kjelstrup-Hansen, M. Madsen, M. Schiek, K. Al-Shamery, A. Lützen and H.-G. Rubahn. *Printed second harmonic active organic nanofiber arrays* Proc. SPIE. 6779, pp. 67790I (2007).
- F. Balzer, M. Madsen, R. Frese, M. Schiek, T. Tamulevicius, S. Tamulevicius and H.-G. Rubahn. *Bottom-up tailoring of photonic nanofibers* Proc. SPIE. 6883, pp. 68830T (2008).
- J. Fiutowski, V. G. Bordo, L. Jozefowski, M. Madsen and H.-G. Rubahn. *Light scattering from an ordered area of needle-shaped organic nanoaggregates: Evidence for optical mode launching* Appl. Phys. Lett. 92, pp. 073302 (2008).
- A. Sileikaite, T. Tamulevicius, S. Tamulevicius, M. Andrulevicius, J. Puiso, A. Guobience, I. Prosycevas, M. Madsen, C. Maibohm and H.-G. Rubahn. *Periodic structures modified with silver nanoparticles for novel plasmonic application* Proc. SPIE. 6988, pp. 69881Q (2008).
- M. Madsen, J. Kjelstrup-Hansen and H.-G. Rubahn. *The surface microstructure controlled growth of organic nanofibres* Nanotechnology. 20, pp. 115601 (2009). Highlighted paper at Nanotechweb.org.

- T. Tamulevicius, A. Sileikaite, S. Tamulevicius, M. Madsen and H.-G. Rubahn. *Scanning electron microscopy of semiconducting nanowires at low voltages* Mater. Sci. (Medziagotyra). 15, pp. 86-90 (2009).

- M. Madsen, G. Kartopu, N. L. Andersen, M. Es-Souni and H.-G. Rubahn. *Para-hexaphenyl nanofiber growth on Au-coated porous alumina templates* Appl. Phys. A. 96, pp. 591-594 (2009).

- M. Madsen, R. M. de Oliveira, J. Kjelstrup-Hansen and H.-G. Rubahn. *Controlled growth of organic nanofibers on nano-and micro-structured gold surfaces* Proc. SPIE. *In preparation* (2009).

- F. Balzer, M. Madsen, J. Kjelstrup-Hansen, M. Schiek and H.-G. Rubahn. *Organic Nanowires* Handbook of Nanophysics: Taylor and Francis. *Accepted* (2010).

Bibliography

[1] F. Balzer and H.-G. Rubahn. *Adv. Funct. Mater.*, 15:17, 2005.

[2] A. Andreev, G. Matt, C. J. Brabec, H. Sitter, D. Badt, H. Seyringer, and N. S. Sariciftci. *Adv. Mater.*, 12:629, 2000.

[3] F. Balzer, V. G. Bordo, A. C. Simonsen, and H.-G. Rubahn. *Phys. Rev. B*, 67:115408, 2003.

[4] F. Quochi, F. Cordella, A. Mura, G. Bongiovanni, F. Balzer, and H.-G. Rubahn. *J. Phys. Chem. B*, 109:21690, 2005.

[5] J. Brewer, H. H. Henrichsen, F. Balzer, L. Bagatolli, A. C. Simonsen, and H.-G. Rubahn. *Proc. SPIE*, 5931:59310Y, 2005.

[6] F. Balzer, L. Kankate, H. Niehus, R. Frese, C. Maibohm, and H.-G. Rubahn. *Nanotechnology*, 17:984, 2006.

[7] S. Müllegger, G. Hlawacek, T. Haber, P. Frank, C. Teichert, R. Resel, and A. Winkler. *Appl. Phys. A*, 87:103, 2007.

[8] G. Koller, S. Berkebile, J. R. Krenn, G. Tzvetkov, G. Hlawacek, O. Lengyel, F. P. Netzer, C. Teichert, R. Resel, and M. G. Ramsey. *Adv. Mater.*, 16:2159, 2004.

[9] H. Yanagi and T. Morikawa. *Appl. Phys. Lett.*, 75:187, 1999.

[10] J. S. Kilby. *IEEE Trans. Electron Devices*, ED-23:648, 1976.

[11] G. E. Moore. *Electronics*, 38:114, 1965.

[12] *ITRS 2007 Edition.* International Technology Roadmap for Semiconductors, 2007.

[13] A. Ashkin, J. M. Dziedzic, J. E. Bjorkholm, and S. Chu. *Opt. Lett.*, 11:288, 1986.

[14] S. Iijima. *Nature*, 354:56, 1991.

[15] K. Hiruma, T. Katsuyama, K. Ogawa, M. Koguchi, H. Kakibayashi, and G. P. Morgan. *Appl. Phys. Lett.*, 59:431, 1991.

[16] A. P. Alivisatos. *Science*, 271:933, 1996.

[17] H. W. Ch. Postma, T. Teepen, Z. Yao, M. Grifoni, and C. Dekker. *Science*, 293:76, 2001.

[18] D. L. Klein, R. Roth, A. K. L. Lim, A. P. Alivisatos, and P. L. McEuen. *Nature*, 389:699, 1997.

[19] R. P. Feynman. *Engineering and Science*, 23:22, 1960.

[20] D. J. Sirbuly, A. Tao, M. Law, R. Fan, and P. Yang. *Adv. Mater.*, 19:61, 2007.

[21] F. Patolsky, G. Zheng, and C. M. Lieber. *Nat. Protoc.*, 1:1711, 2006.

[22] Z. Fan, J. C. Ho, Z. A. Jacobson, H. Razavi, and A. Javey. *Proc. Natl. Acad. Sci. U. S. A.*, 105:11066, 2008.

[23] J. Hahm and C. M. Lieber. *Nano Lett.*, 4:51, 2004.

[24] Z. Chen, J. Appenzeller, Y.-M. Lin, J. Sippel-Oakley, A. G. Rinzler, J. Tang, S. J. Wind, P. M. Solomon, and P. Avouris. *Science*, 311:1735, 2006.

[25] A. Javey, S. Nam, R. S. Friedman, H. Yan, and C. M. Lieber. *Nano Lett.*, 7:773, 2007.

[26] M. Law, L. E. Greene, J. C. Johnson, R. Saykally, and P. Yang. *Nat. Mater.*, 4:455, 2005.

[27] B. Tian, T. J. Kempa, and C. M. Lieber. *Chem Soc. Rev.*, 38:16, 2009.

[28] Y. Huang, X. Duan, and C. M. Lieber. *Small*, 1:142, 2005.

[29] M. Law, D. J. Sirbuly, J. C. Johnson, J. Goldberger, R. J. Saykally, and P. Yang. *Science*, 305:1269, 2004.

[30] A. Javey. *ACS Nano*, 2:1329, 2008.

[31] Y. Cui, Z. Zhong, D. Wang, W. U. Wang, and C. M. Lieber. *Nano lett.*, 3:149, 2003.

[32] F. Qian, Y. Li, S. Gradecak, D. Wang, C. J. Barrelet, and C. M. Lieber. *Nano Lett.*, 4:1975, 2004.

[33] S. Gradecak, F. Qian, H.-G. Park, and C. M. Lieber. *Appl. Phys. Lett.*, 87:173111, 2005.

[34] L. Samuelson. *Materials Today*, 6:22, 2003.

[35] R. Yerushalmi, Z. A. Jacobson, J. C. Ho, Z. Fan, and A. Javey. *Appl. Phys. Lett.*, 91:203104, 2007.

[36] Y. Huang, X. Duan, Q. Wei, and C. M. Lieber. *Science*, 291:630, 2001.

[37] B. Tian, X. Zheng, T. J. Kempa, Y. Fang, N. Yu, G. Yu, J. Huang, and C. M. Lieber. *nature*, 449:885, 2007.

[38] Z. Fan, J. C. Ho, Z. A. Jacobson, R. Yerushalmi, R. L. Alley, H. Razavi, and A. Javey. *Nano Lett.*, 8:20, 2008.

[39] H. Namatsu, K. Kurihara, M. Nagase, and T. Makino. *Appl. Phys. Lett.*, 70:619, 1997.

[40] A. M. Morales and C. M. Lieber. *Science*, 279:208, 1998.

[41] T. Mårtensson, M. Borgström, W. Seifert, B. J. Ohlsson, and L. Samuelson. *Nanotechnology*, 14:1255, 2003.

[42] Z. W. Pan, Z. R. Dai, and Z. L. Wang. *Science*, 291:1947, 2001.

[43] T. I. Kamins, R. S. Williams, D. P. Basile, T. Hesjedal, and J. S. Harris. *J. Appl. Phys.*, 89:1008, 2001.

[44] R. S. Wagner and W. C. Ellis. *Appl. Phys. Lett.*, 4:89, 1964.

[45] J. Hu, T. W. Odom, and C. M. Lieber. *Acc. Chem. Res.*, 32:435, 1999.

[46] R. O. Al-Kaysi and C. J. Bardeen. *Chem. Commun.*, page 1224, 2006.

[47] C. R. Martin. *Science*, 266:1961, 1994.

[48] B. Mandl, J. Stangl, T. Mårtensson, A. Mikkelsen, J. Eriksson, L. S. Karlsson, G. Bauer, L. Samuelson, and W. Seifert. *Nano lett.*, 6:1817, 2006.

[49] F. Balzer and H.-G. Rubahn. *Appl. Phys. Lett.*, 79:3860, 2001.

[50] T. Takahashi, K. Takei, J. C. Ho, Y.-L. Chueh, Z. Fan, and A. Javey. *J. Am. Chem. Soc.*, 131:2102, 2009.

[51] J. Kjelstrup-Hansen. *Integration of nanocomponents in microsystems.* PhD thesis, Technical University of Denmark, 2006.

[52] J. Kjelstrup-Hansen, O. Hansen, H.-G. Rubahn, and P. Bøggild. *Small*, 2:660, 2006.

[53] A. Ural, Y. Li, and H. Dai. *Appl. Phys. Lett.*, 81:3464, 2002.

[54] H. Dai, J. H. Hafner, A. G. Rinzler, D. T. Colbert, and R. E. Smalley. *Nature*, 384:147, 1996.

[55] E. Yenilmez, Q. Wang, R. J. Chen, D. Wang, and H. Dai. *Appl. Phys. Lett.*, 80:2225, 2002.

[56] M. T. Lloyd, J. E. Anthony, and G. G. Malliaras. *Materials Today*, 10:34, 2007.

[57] M. Schiek, F. Balzer, K. Al-Shamery, A. Lützen, and H.-G. Rubahn. *Soft matter*, 4:277, 2008.

[58] M. Bendikov, F. Wudl, and D. F. Perepichka. *Chem. Rev.*, 104:4891, 2004.

[59] C. Ziegler and H. S. Nalwa (Ed.). *Handbook of organic conductive molecules and polymers*, volume 3. Chapter 13. Wiley, Chichester, 1997.

[60] R. Resel. *Thin Solid Films*, 433:1, 2003.

[61] C. D. Dimitrakopoulos and P. R. L. Malenfant. *Adv. Mater.*, 14:99, 2002.

[62] N. Koch, A. Pogantsch, E. J. W. List, G. Leising, R. I. R. Blyth, M. G. Ramsey, and F. P. Netzer. *Appl. Phys. Lett.*, 74:2909, 1999.

[63] R. H. Friend, R. W. Gymer, A. B. Holmes, J. H. Burroughes, R. N. Marks, C. Taliani, D. D. C. Bradley, D. A. Dos Santos, J. L. Brédas, M. Lögdlund, and W. R. Salaneck. *Nature*, 397:121, 1999.

[64] J. J. M. Halls, C. A. Walsh, N. C. Greenham, E. A. Marseglia, R. H. Friend, S. C. Moratti, and A. B. Holmes. *Nature*, 376:498, 1995.

[65] G. Yu, J. Gao, J. C. Hummelen, F. Wudl, and A. J. Heeger. *Science*, 270:1789, 1995.

[66] C. J. Brabec, N. S. Sariciftci, and J. C. Hummelen. *Adv. Funct. Mater*, 11:15, 2001.

[67] F. J. M. Hoeben, P. Jonkheijm, E. W. Meijer, and A. P. H. J. Schenning. *Chem. Rev.*, 105:1491, 2005.

[68] C. Maibohm, J. R. Brewer, H. Sturm, F. Balzer, and H.-G. Rubahn. *J. Appl. Phys.*, 100:054304, 2006.

[69] T. Tamulevicius, A. Sileikaite, S. Tamulevicius, M. Madsen, and H.-G. Rubahn. *Mater. Sci. (Medziagotyra)*, 15:86, 2009.

[70] K. Hänel, A. Birkner, S. Müllegger, A. Winkler, and Ch. Wöll. *Surf. Sci.*, 600:2411, 2006.

[71] A. M. Hynes, H. Ashraf, J. K. Bhardwaj, J. Hopkins, I. Johnston, and J. N. Shepard. *Sens. Actuators, A*, 74:13, 1999.

[72] A. A. Ayón, R. Braff, C. C. Lin, H. H. Sawin, and M. A. Schmidt. *J. Electrochem. Soc.*, 146:339, 1999.

[73] A. A. Ayón, R. A. Braff, R. Bayt, H. H. Sawin, and M. A. Schmidt. *J. Electrochem. Soc.*, 146:2730, 1999.

[74] L. A. Donohue, J. Hopkins, R. Barnett, A. Newton, and A. Barker. *Proc. SPIE*, 5347:44, 2004.

[75] M. A. Blauw, G. Craciun, W. G. Sloof, P. J. French, and E. van der Drift. *J. Vac. Sci. Technol. B*, 20:3106, 2002.

[76] J.-H. Min, G.-R. Lee, J. k. Lee, S. H. Moon, and C.-K. Kim. *J. Vac. Sci. Technol. B*, 22:893, 2004.

[77] M. Schiek, F. Balzer, K. Al-Shamery, J. R. Brewer, A. Lützen, and H.-G. Rubahn. *Small*, 4:176, 2008.

[78] H. Yanagi and S. Okamoto. *Appl. Phys. Lett.*, 71:2563, 1997.

[79] S. Tasch, C. Brandstatter, F. Meghdadi, G. Leising, G. Froyer, and L. Athouel. *Adv. Mater.*, 9:33, 1997.

[80] H. Yanagi, S. Okamoto, and T. Mikami. *Synth. Met.*, 91:91, 1997.

[81] F. Meghdadi, S.Tasch, B. Winkler, W.Fischer, F.Stelzer, and G.Leising. *Synth. Met.*, 85:1441, 1997.

[82] D. J. Gundlach, Y.-Y. Lin, T. N. Jackson, and D. G. Schlom. *Appl. Phys. Lett.*, 71:3853, 1997.

[83] P. Puschnig and C. Ambrosch-Draxl. *Phys. Rev. B.*, 60:7891, 1999.

[84] F. Balzer, V. G. Bordo, R. Neuendorf, K. Al-Shamery, A. C. Simonsen, and H.-G. Rubahn. *IEEE Trans. Nanotechn.*, 3:67, 2004.

[85] A. Niko, F. Meghdadi, C. Ambrosch-Draxl, P. Vogl, and G. Leising. *Synth. Met.*, 76:177, 1996.

[86] K. N. Baker, A. V. Fratini, T. Resch, H. C. Knachel, W. W. Adams, E. P. Socci, and B. L. Farmer. *Polymer*, 34:1571, 1993.

[87] S. Guha, W. Graupner, R. Resel, M. Chandrasekhar, H. R. Chandrasekhar, R. Glaser, and G. Leising. *Phys. Rev. Lett.*, 82:3625, 1999.

[88] D. E. Williams and T. L. Starr. *Computers and Chemistry.*, 1:173, 1977.

[89] F. Balzer and H.-G. Rubahn. *Surf. Sci.*, 548:170, 2004.

[90] F. Balzer, K. Al-Shamery (Ed.), H.-G. Rubahn (Ed.), and H. Sitter (Ed.). *Organic nanostructures for next generation devices.* Chapter 3. Springer-Verlag, Berlin Heidelberg, 2008.

[91] Y. Yoshida, H. Takiguchi, T. Hanada, N. Tanigaki, E.-M. Han, and K. Yase. *J. Cryst. Growth*, 198/199:923, 1999.

[92] E. Zojer, N. Koch, P. Puschnig, F. Meghdadi, A. Niko, R. Resel, C. Ambrosch-Draxl, M. Knupfer, J. Fink, J. L. Brédas, and G. Leising. *Phys. Rev. B*, 61:16538, 2000.

[93] M. Ohring. *Materials science of thin films.* Academic Press, 2002.

[94] H. Sitter, R. Resel, G. Koller, M. G. Ramsey, A. Andreev, C. Teichert, K. Al-Shamery (Ed.), H.-G. Rubahn (Ed.), and H. Sitter (Ed.). *Organic nanostructures for next generation devices.* Chapter 1. Springer-Verlag, Berlin Heidelberg, 2008.

[95] B. Krause, A. C. Dürr, K. Ritley, F. Schreiber, H. Dosch, and D. Smilgies. *Phys. Rev. B.*, 66:235404, 2002.

[96] L. Kankate, F. Balzer, H. Niehus, and H.-G. Rubahn. *J. Chem. Phys.*, 128:084709, 2008.

[97] C. Teichert, G. Hlawacek, A. Andreev, H. Sitter, P. Frank, A. Winkler, and N. S. Sariciftci. *Appl. Phys. A.*, 82:665, 2006.

[98] K. Müller and C. C. Chang. *Surf. Sci.*, 14:39, 1969.

[99] G. Koller, S. Berkebile, M. Oehzelt, P. Puschnig, C. Ambrosch-Draxl, F. P. Netzer, and M. G. Ramsey. *Science*, 317:351, 2007.

[100] A. J. Fleming, S. Surnev, F. P. Netzer, M. G. Ramsey, H.-G. Rubahn (Ed.), H. Sitter (Ed.), G. Horowitz (Ed.), and K. Al-Shamery (Ed.). *Interface Controlled Organic Thin Films.* Chapter 27. Springer-verlag, Berlin Heidelberg, 2009.

[101] M. Oehzelt, L. Grill, S. Berkebile, G. Koller, F. P. Netzer, and M. G. Ramsey. *ChemPhysChem*, 8:1707, 2007.

[102] S. Müllegger and A. Winkler. *Surf. Sci.*, 600:1290, 2006.

[103] T. Haber, S. Müllegger, A. Winkler, and R. Resel. *Phys. Rev. B.*, 74:045419, 2006.

[104] R. Resel, M. Oehzelt, T. Haber, G. Hlawacek, C. Teichert S. Müllegger, and A. Winkler. *J. Cryst. Growth*, 283:397, 2005.

[105] G. Hlawacek, C. Teichert, S. Müllegger, R. Resel, and A. Winkler. *Synt. Met.*, 146:383, 2004.

[106] S. Müllegger, S. Mitsche, P. Pölt, K. Hänel, A. Birkner, C. Wöll, and A. Winkler. *Thin Solid Films*, 484:408, 2005.

[107] S. Müllegger, I. Salzmann, R. Resel, G. Hlawacek, C. Teichert, and A. Winkler. *J. Chem Phys.*, 121:2272, 2006.

[108] W. R. Tyson and W. A. Miller. *Surf. Sci.*, 62:267, 1977.

[109] L. Vitos, A. V. Ruban, H. L. Skriver, and J. Kollár. *Surf. Sci.*, 411:186, 1998.

[110] J. Kjelstrup-Hansen, H. H. Henrichsen, P. Bøggild, and H.-G. Rubahn. *Thin Solid Films*, 515:827, 2006.

[111] M. Cranney, Y. Chalopin, A. J. Mayne, and G. Dujardin. *Appl. Phys. A.*, 94:767, 2009.

[112] G. Kartopu, S. Habouti, and M. Es-Souni. *Mater. Chem. Phys.*, 107:226, 2008.

[113] A Vlad, M. Mátéfi-Tempfli, S Faniel, V Bayot, S Melinte, L Piraux, and S Mátéfi-Tempfli. *Nanotechnology*, 17:4873, 2006.

[114] F. Balzer and H.-G. Rubahn. *Patent PA 2004 01676.*

[115] F. Balzer, R. Frese, M. Madsen, K. Thilsing-Hansen, and H.-G. Rubahn. *J. Laser Micro/Nanoeng.*, 1:275, 2006.

[116] M. Madsen, R. Melina de Oliveira Hansen, J. Kjelstrup-Hansen, and H.-G. Rubahn. *Proc. SPIE*, Submitted, 2009.

[117] X. Liu, J. Kjelstrup-Hansen, K. Thilsing-Hansen, H. H. Henrichsen, and H.-G. Rubahn. *Proc. TNT09 conference.*, In preparation, 2009.

[118] B. Steinberger, A. Hohenau, H. Ditlbacher, A. L. Stepanov, A. Drezet, F. R. Aussenegg, A. Leitner, and J. R. Krenn. *Appl. Phys. Lett.*, 88:094104, 2006.

[119] F. Balzer and H.-G. Rubahn. *Nano lett.*, 2:747, 2002.